Diogo Duarte Pacheco Botelho Moniz

Licenciado em Engenharia de Materiais

Piezoelectric ceramics for bone regeneration

Dissertação para obtenção do Grau de Mestre em
Engenharia de Materiais

Advisor: M. Carmo Lança, (Assistant Professor), DCM FCT-UNL and CENIMAT

Co-advisor: M. Margarida Lima, (Assistant Professor), DCM FCT-UNL and CENIMAT

Jury:

President: João Paulo Borges, (Associate Professor w/ Habilitation), DCM FCT-UNL and CENIMAT

Examiner: Rui Alberto Garção Barreira do Nascimento Igreja, (Assistant Professor) DCM FCT-UNL and CENIMAT

Advisor: M. Carmo Lança, (Assistant Professor), DCM FCT-UNL and CENIMAT

October 2019

FACULDADE DE CIÊNCIAS E TECNOLOGIA
UNIVERSIDADE NOVA DE LISBOA

Piezoelectric ceramics for bone regeneration

À minha avó Maria Helena e aos meus pais Francisca e Carlos.

Acknowledgments

Gostaria de agradecer muito à minha orientadora Prof. Maria do Carmo Lança e aos co-orientadores Prof. Maria Margarida Lima e Prof. João Paulo Borges por me terem aceitado como seu aluno de dissertação e por todo o apoio profissional e pessoal dado ao longo deste projeto.

Ao DCM e CENIMAT por todas as ferramentas e meios disponibilizados, à FCT-UNL por ter sido a instituição que me formou e me deu as memoráveis recordações do percurso académico que fiz.

À Universidade de Aveiro, em particular ao Pedro Prezas e ao Professor Manuel Graça, pela disponibilidade e ajuda prestada na polarização por corona das amostras.

Agradeço também à Andreia Lopes por toda a ajuda incansável no dia-a-dia durante este projecto, tal como ao Edgar Camacho e à Fernanda Bruno de Carvalho por toda a disponibilidade e boa disposição em todas as horas de almoço e não só.

Aos que "deambulam eternamente", agradeço terem-me mostrado um exemplo extraordinário de amizade que, por isso mesmo, espero guardar para o resto da vida.

A minha família que, apesar das suas atarefadas vidas e dispersas pelo mundo, nunca se esqueceram de se preocupar e mostrar apoio.

A quem me criou com tudo o que tinha sem me pedir nada em troca, obrigado "Cácá".

O mais humilde agradecimento para os meus pais e avó, por terem sido quem me conduziu enquanto cresci e por me terem educado a partir do exemplo, embutindo valores e princípios que espero conseguir, sempre que possível, aplicar na minha vida.

Resumo

O titanato de bário (BT) é um cerâmico piezoelétrico bastante estudado e neste trabalho será alvo de dopagem com cálcio até ao limite em que a substituição não comprometa a sua fase tetragonal, que lhe confere as aptidões piezoelétricas. Partindo dos reagente analíticos $CaCO_3$, $BaCO_3$ e TiO_2, prepararam-se, por reação no estado sólido, misturas de $Ba_{(1-x)}Ca_xTiO_3$ $0 \leq x \leq 0{,}3$ (BCT). O material foi sinterizado a temperaturas entre 1150 °C e 1450 °C em atmosferas de ar e N_2. Compósitos foram produzidos a partir de $Ba_{(1-x)}Ca_xTiO_3$ $0 \leq x \leq 0{,}15$ e hidroxiapatite (HP) em proporções de 90/10 e 80/20 (BCT/HP %) em peso. A caracterização do material foi feita utilizado análises como DTA-TG, granulometria, difração de raios-X, FTIR, Raman e SEM/EDS. As amostras foram polarizadas pelo método de corona a 110 °C durante 1 hora com potencial de ponta de -15kV e -2kV potencial de rede para subsequente análise de bioactividade. A polarização foi analisada por correntes termo estimuladas de depolarização (TSDC).

A substituição de cálcio até 15% molar deformou a estrutura cristalina do BT sem comprometer a sua tetragonalidade, mantendo a temperatura de Curie entre 123 °C e 125 °C. Os materiais produzidos comprovaram ser não-citotóxicos. Polarização por corona foi bem sucedida.

Hidroxiapatite reagiu com BCT quando a sinterização foi feita a 1350 °C formando novas fases como fosfato de bário, mas mantendo parcialmente as estruturas originais.

Um estudo embrionário de bioactividade foi feito emergindo as amostras em SBF (*simulated body fluid*) durante 7 dias e analisando, por ICP-AES, amostras de meio retiradas em diferentes intervalos de tempo. No mesmo âmbito, fez-se análise da superfície da amostra no final da experiência através de SEM/EDS. Os resultados indicam que as amostras polarizadas não contendo hidroxiapatite têm maior tendência para depositarem iões de fósforo e cálcio na sua superfície.

Abstract

Piezoelectric materials have shown large potential on hard tissue applications due to their ability to stimulate osteogeneses and osseointegration. Barium titanate (BT) is a well-known piezoelectric ceramic. This work reports the consequences of calcium acceptance in BT lattice without compromising the formation of piezoelectric tetragonal phase under physiological conditions. Analytical reagents $CaCO_3$, $BaCO_3$ and TiO_2 were used to prepare, via solid state reaction, $Ba_{(1-x)}Ca_xTiO_3$ (BCT), $0 \leq x \leq 0.3$ mixtures. Materials were sintered from 1150°C to 1450°C under air and N_2 atmospheres. Composites were prepared from $Ba_{(1-x)}Ca_xTiO_3$ ($0 \leq x \leq 0.15$) and hydroxyapatite (HP) at 10/90 and 20/80 (HP/BCT wt%) proportions. Reagents and produced ceramics were characterized by DTA-TG, granulometry, X-ray diffraction, FTIR, Raman and SEM/EDS. Samples were polarized by corona poling at 110°C, 1 hour, tip potential -15kV and -2kV grid potential for subsequent bioactivity essays. The polarization was analysed by thermally stimulated depolarization currents.

Calcium substitution up to 15 mol% deformed the known $BaTiO_3$ lattice without compromising the tetragonal phase stability, maintaining Curie point between 123 °C and 125 °C. All materials tested were non cytotoxic. Corona poling was successfully done to BCT samples.

Hydroxyapatite reacts with BCT while sintered at 1350 °C forming different phases, but materials original structures are partially maintained.

Early stage bioactivity studies made after both polarized and unpolarized samples were immersed in SBF (simulated body fluid) for 7 days. Results from ICP-AES supported by SEM/EDS point to the materials enhanced ability while polarized to deposit calcium and phosphor ions on its surface.

Table of Contents

Acknowledgments vii
Resumo ix
Abstract xi
Table of Contents xiii
List of Tables xv
List of Figures xvii
Abbreviations and Symbols xxi
1. Motivation and Objectives 1
2. Introduction 3
2.1. Piezoelectric Barium Titanate 3
2.2. Piezoelectricity and biocompatibility compromise 4
2.3. Hydroxyapatite 5
2.4. Sample preparation and characterization 6
2.5. Applications and challenges 7
3. Materials and methods 9
3.1. Analytical reagents characterization 9
3.2. Barium titanate and calcium doped BT synthesis 9
3.3. Sample characterization 10
3.4. Cytotoxicity tests 10
3.5. Polarization and TSDC 10
3.6. Bioactivity tests 10
4. Results and Discussion 11
4.1. Analytical reagents $CaCO_3$, $BaCO_3$ and TiO_2 11
4.1.1. Differential thermal analysis-Thermogravimetry 11
4.1.2. Granulometry and X-Ray diffraction 11
4.1.3. FTIR 13
4.2. Calcium doped BT mixtures 13
4.2.1. DTA-TG and Granulometry 13
4.2.2. X-Ray Diffraction 16
4.2.3. FTIR 17
4.2.4. RAMAN 18
4.2.5. DSC 19
4.2.6. SEM and EDS 21
4.2.7. Cytotoxicity 21

4.2.8. Thermally stimulated depolarization currents 23
4.3. Hydroxyapatite and calcium doped BT composite 25
4.3.1. X-Ray Diffraction 25
4.3.2. SEM and EDS 27
4.4. ICP-AES and SEM/EDS accounting for bioactivity essays 28
5. Conclusions 31
5.1. Future perspectives 32
References 34
Annexes 40
A. Introduction 40
B. Sample production method 41
C. DTA-TG mixtures analysis 42
D. Granulometry 44
E. XRD 45
E.1. Calcium doped barium titanate 45
E.2. Hydroxyapatite composites 46
F. FTIR 48
G. Raman analysis of every mixture 49
H. DSC 52
I. SEM and EDS 53
I.1. Calcium doped barium titanate 53
I.2. Hydroxyapatite composites 55
J. Cytotoxicity 57
K. Thermal stimulated depolarization currents 58
L. Bioactivity essays 60

List of Tables

Table 3.1 Summary of prepared samples and their sintering conditions..... 9

Table 4.1 Granulometry analysis results for milling time and correspondent average particle size of BT mixture. 15

Table 4.2 Average particle size (μm) for every mixture prepared. Results were obtained by granulometry analysis made in water. 15

Table 4.3 Depolarization parameters from TSDC analysis. 25

List of Figures

Figure 2.1.1 (a) Perovskite cubic unit cell structure barium titanate presents above Curie temperature. Below Curie temperature it presents tetragonal structure where Ti^{4+} ion displacement will shift upward (b) and downward (c) [8]. 3

Figure 4.1.1 DTA analysis of the three analytical reagents $BaCO_3$, $CaCO_3$ and TiO_2. 11

Figure 4.1.2 Granulometry analysis of the three analytical reagents $BaCO_3$, $CaCO_3$ and TiO_2. 12

Figure 4.1.3 XRD of $BaCO_3$, $CaCO_3$ and TiO_2 powder. ★ tetragonal anatase, ✳ rhombohedral calcite and l orthorhombic witherite. 12

Figure 4.1.4 FTIR analysis of each $BaCO_3$, $CaCO_3$ and TiO_2 analytical reagents in powder state. 13

Figure 4.2.1 BT and BCT30 differential thermic analysis in order to compare the behaviour of the highest calcium substituted material and no calcium substituted material. 14

Figure 4.2.2 Mass loss (%) in function of calcium presence along the calcination process with a 5 °C min^{-1} heating rate from room temperature up to 1000 °C remaining at the highest temperature for 4 hours. 15

Figure 4.2.3 X-Ray diffraction of BT and BCT30 mixtures sintered at 1350 °C in both air and N_2 atmospheres. ★ tetragonal $Ba_{(1-x)}Ca_xTiO_3$, l orthorhombic $CaTiO_3$ and ✳ tetragonal $BaTiO_3$. 16

Figure 4.2.4 FTIR analysis of every $Ba_{1-x}Ca_xTiO_2$ compounds mixed with KBr. 17

Figure 4.2.5 Relation between FTIR absorption peaks and calcium substitution. 18

Figure 4.2.6 Raman analysis of BCT30, BCT15 and BT samples. 19

Figure 4.2.7 Differential scanning calorimetry analysis to all the $Ba_{1-x}Ca_xTiO_2$ mixtures in order to obtain the Curie point for each one. 20

Figure 4.2.8 Evolution of Curie point in function of calcium molar percentage. 20

Figure 4.2.9 SEM showing different grain sizes in $Ba_{(1-x)}Ca_xTiO_3$ $0 \leq x \leq 0.3$ 21

Figure 4.2.10 Cytotoxicity results for all $Ba_{1-x}Ca_xTiO_3$ mixtures and the control with correspondent error bars. 22

Figure 4.2.11 Thermally stimulated depolarization currents of $Ba_{(1-x)}Ca_xTiO_3$ $0 \leq x \leq 0.15$ polarized samples and polarization temperature marked as Tp. 23

Figure 4.2.12 Linear fit done from equation 4.13 and 1/T combination to calculate the activation energy and τ_0 of polarized samples. Dashed lines represent the linear fit done from the original curves. 24

Figure 4.3.1 X-ray diffraction of 1350 °C sintered and non-sintered commercial hydroxyapatite. ▲ Hydroxyapatite, ■ β-TCP and ✳ α-TCP. 25

Figure 4.3.2 X-ray diffraction comparison between BCT10 samples containing 10 wt% and 20 wt% hydroxyapatite, BCT10 sample and HP sample all sintered at 1350 °C. ▲ Hydroxyapatite, ◆ barium phosphate, ✚ calcium doped barium titanate and ✳ α-TCP. 26

Figure 4.3.3 BCT10/HP (90/10) composite under SEM microscopy and EDS quantification on three different points of the sample. 27

Figure 4.4.1 SEM microscopy showing BCT05 surface: (a) unpolarized after sintering, (b) unpolarized after immersed in SBF for 7 days (c) polarized after 7 day immersion in SBF. 28

Figure 4.4.2 ICP-AES results for both calcium and phosphor concentration in SBF samples, collected during 7 days, out of a recipient containing one polarized $Ba_{(1-x)}Ca_xTiO_3$ $0 \leq x \leq 0.15$ ceramic sample and 250 mL SBF. 30

Figure A.1 Electric field application effect on the spontaneous oriented domains formed from cooling in piezoelectric materials [77] 40

Figure A.2 $BaTiO_3$-TiO_2 equilibrium phase diagram [45] 40

Figure A.3 Phase diagram of $BaTiO_3$ and CaTiO3 [46] 41

Figure B.1 Schematic of BT and BCT sample production 41

Figure B.2 Apparatus of the corona system used to polarize samples close to the Curie point (left) and corona tip and grid schematic (right) 42

Figure C.1 $BaCO_3$ analytical reagent DTA-TG analysis 42

Figure C.2 TiO_2 analytical reagent DTA-TG analysis. 43

Figure C.3 $CaCO_3$ analytical reagent DTA-TG analysis 43

Figure C.4 Differential thermic analysis of all $Ba_{(1-x)}Ca_xTiO_3$ mixtures on the range 400 °C to 1100 °C. 44

Figure D.1 Granulometry analysis for commercial hydroxyapatite used in composite making. 44

Figure E.1 XRD analysis for BT samples sintered at different temperatures from 1150 °C to 1350 °C. 45

Figure E.2 XRD analysis for BCT30 samples sintered at different temperatures from 1150 °C to 1350 °C (on top) and zoom on diffractograms in areas with peaks of $CaTiO_3$ (bellow). 45

Figure E.3 XRD for $Ba_{(1-x)}Ca_xTiO_3$ $0 \leq x \leq 0.15$ mixture sintered at 1350 °C. Sample BCT15 is the only sample to present a double peak below $2\theta = 40°$ and it might be due to a different conformation of titanium during sintering. 46

Figure E.4 X-ray diffraction of all BT and hydroxyapatite sintered at 1350 °C. 46

Figure E.5 X-ray diffraction in order to compare BCT05 composites with HP and solo BCT05, all 1350 °C sintered. 47

Figure E.6 X-ray diffraction for all BCT15 composites to be compared with BCT15 solo and HP, all 1350 °C sintered. 47

Figure F.1 Barium titanate sintered at 1350 °C FTIR spectrum 48

Figure F.2 Ti-O vibration modes: Bending vibration (left), stretching vibration (right) [61]. 48

Figure G.1 Raman analysis of all the mixtures $Ba_{1-x}Ca_xTiO_3$ sintered at 1350 °C. Note along the increase of calcium presence the disappearance of the 309 cm^{-1} peak visible in BT inside the dashed rectangular. It is also noticeable the progression of a second peak signed with the dot-dash line to higher Raman shift values in function of calcium presence. 49

Figure G.2 Raman analysis of the 1350 °C sintered mixtures that qualify to composite making. Up to BCT15 is possible to spot the 309 cm^{-1} peak that assures tetragonality of the material. The perturbation spotted in 470 cm^{-1} is also related with tetragonality. 49

Figure G.3 Raman analysis of $Ba_{(1-x)}Ca_xTiO_3$ $0 \leq x$ 0.3 mixtures sintered at 1450 °C. 50

Figure G.4 Raman microscopy for all $Ba_{(1-x)}Ca_xTiO_3$ mixtures. 51

Figure G.5 Raman vibration modes [61] 51

Figure H.1 Lattice distortion caused by Ca^{2+} substitution on B-site of ABO_3 perovskite structure [28]. 52

Figure H.2 DSC analysis of BT samples sintered at different temperatures 1150 °C, 1250 °C, 1350 °C and 1450 °C. 52

Figure H.3 DSC analysis of BCT30 samples sintered at 1150 °C, 1250 °C , 1350 °C and 1450 °C. 53

Figure I.1 SEM analysis for diamond paste polished samples of BT, BCT15 and BCT30. 53

Figure I.2 SEM and EDS analysis for BCT30 polished sample. 54

Figure I.3 BT/HP (90/10) composite under SEM microscopy with EDS quantification on four different points of the sample. 55

Figure I.4 EDS quantification of BCT10/HP (90/10) composite. SEM imaging of this same sample is present in section 4.3.2, figure 4.21. 56

Figure J.1 Labelled plate used in cytotoxicity assays with the positions of each intervenient in order to account for every mixture cell viability. 57

Figure K.1 Results for polarized and depolarized $Ba_{(1-x)}Ca_xTiO_3$ $0 \leq x \leq 0.15$ samples submitted to thermally stimulated depolarization currents. 58

Figure K.2 Never polarized samples TSDC analysis. 59

Figure K.3 TSDC spectrum showing a pyroelectric anomalous current on BT sample. 59

Figure L.1 SEM/EDS results for polarized BCT05 sample after 7 days SBF immersion. 60

Figure L.2 EDS quantification for polarized BCT05 samples immersed in SBF for 7 days. 61

Figure L.3 ICP-AES results for $Ba_{(1-x)}Ca_xTiO_3$ $0 \leq x \leq 0.15$ unpolarized samples 7 days immersion in SBF. Samples were put inside a recipient containing 250 mL when the test starts. Each graph shows the SBF calcium and phosphor concentration varying during the 7 days period. 62

Figure L.4 ICP-AES results for polarized composites. 63

Figure L.5 ICP-AES results for unpolarized composites. 64

Figure L.6 SEM/EDS mapping and quantification of polarized BT sample after 7 days immersion in SBF. 65

Figure L.7 SEM/EDS mapping and quantification for polarized BCT10 sample after 7 days immersion in SBF. 66

Figure L.8 SEM/EDS mapping and quantification for polarized BCT15 sample after 7 day immersion in SBF. 67

Abbreviations and Symbols

PFM – Piezoelectric Force Microscopy

HP – Hydroxyapatite

BT – Barium Titanate

d_{33} – Piezoelectric coefficient

XRD – X-Ray Diffraction

SEM/EDS – Scanning Electron Microscope/ Energy Dispersive Spectroscopy

TSDC – Thermally Stimulated Depolarization Currents

DTA-TG – Differential Thermal Analysis-Thermogravimetry

FTIR – Fourier Transform Infrared

ICP-AES – Inductively coupled plasma atomic emission spectroscopy

BCT – Calcium doped barium titanate

BCT/HP – Calcium doped barium titanate and hydroxyapatite composite

BPH – Barium phosphate hydroxide

α-TCP – alpha tricalcium phosphate

β-TCP – beta tricalcium phosphate

T_c – Curie temperature

χ – Electric susceptibility

C – Curie constant

T_θ – Curie temperature in stressed state

Q_{11} and Q_{12} – Electrostrictive coefficients

α – Temperature coefficient

p – Hydrostatic stress

ε_0 – Permittivity

Q_p – Polarization charge

β – Heating rate

J – Current density

τ – Relaxation time

E_a – Activation energy

k – Boltzmann constant

1. Motivation and Objectives

Bone implants have been used worldwide for many years, in the last decades the developments in tissue engineering generated various new applications. Increased accessibility to these means by a rising population gave way to a $46/€41 million market in 2017 expected to reach $67/€60 million by 2025 [1]. The demand for bone implants can only grow bigger by reaching more patients in a wider socioeconomical spectrum.

Surgeries involving orthopaedic implants are, in many cases, obviously very invasive and may cause infections or disease transmission. In this sense, medics avoid doing it until it is absolute necessary. These procedures often require bone grafts, in other words the harvesting of healthy bone from a part of the body to replace the affected one. The most successful practice is to use the patient own bone, called an autograft. However, the bone quality may be poor and scarce specially in older patients, making it necessary to find a bone supplement donor performing an allograft. Xenogeneic bone (i.e. animal donor) or allografts might generate other problems related with immune rejection leading to total implant failure [2].

Another very important parameter used to evaluate implant failure is clinically marked mobility. Implant mobility is a consequence of deficient osseointegration and, at the 1st European Workshop in Periodontology, its absence was consider to be a key criteria to implant success [3]. The case of a "falling" implant is defined by the continuous bone anchorage loss whereas a "failed" implant is one that is mobile. This problem can also be present with no distinctly radiographic signs of bone change making it more difficult to do an early diagnose. Considering that the body is a biological system, implant complications have multiple overlapping causes but can be summarized in infections, impaired healing and overload [4]. The first two, being strictly biological related are off the scope of the work here reported.

"Overload" is the name given for bone deformation due to excessive imposed mechanical stress. This term is more accurately related with the loss of bone supporting capacity in the implant surrounding area that eventually will lead to mobility and consequent implant failure. The ideal goal to address this problem would be to stimulate bone formation in order to regain implant support in the nearby affected areas. This is precisely why piezoelectric materials have been gaining such big interest in tissue engineering applications. It is known that electric phenomena exist in living tissues, but it is yet to be fully understood how it affects cell migration. Regardless, many studies indicate that electrical stimulation may cause enhanced bone density [5]. By taking advantage of body movement and a known complication with bone implants like overload, piezoelectric biomaterials might be able to transform the problem into a solution.

In order to approach the high standards imposed by the human body, bone in particular, this work examines the application of a composite material made of calcium doped barium titanate, synthesized by solid reaction route, and hydroxyapatite in order to mimic or excel the piezoelectric properties of bone and promote osseointegration. To achieve this purpose, it is necessary to:

- Guarantee the tetragonality of the final material and enhance its piezoelectric properties.
- Understand and limit the Curie point evolution with regards to calcium doping as well as the amount of hydroxyapatite used in the composite.
- Ensure sample polarization.
- Test the materials for cytotoxicity and bioactivity.

2. Introduction

2.1. Piezoelectric Barium Titanate

Piezoelectricity was first discovered by Pierre and Jacques Curie in 1880 [6]. This property of materials generates an electric signal induced by a deformation (direct piezoelectric effect). The mechanical strain causes the asymmetric shift of ions or charges which induces a change in the electric polarization. Since it is known that an electrical stimulation, provided by mechanical stress, helps tissue regeneration there has been much interest in scaffolds made from piezoelectric materials for tissue engineering applications [2], [5], [7], [8].

Barium titanate ($BaTiO_3$) was the first piezoelectric ceramic developed and as such it has been widely studied [9]. Mechanically and chemically very stable, it can be easily prepared and used as a polycrystalline ceramic. Structure wise belongs to the perovskite family (ABO_3) that takes its name from $CaTiO_3$, the mineral perovskite. The cubic crystal structure has an A-large cation in the corner with the coordination number 12, a B-smaller cation in the middle with the coordination number 6 and a anion, usually oxygen, located in the centre of the face edges [10]. $BaTiO_3$ may have different crystallographic conformations [11]. At room temperature presents a ferroelectric tetragonal phase and at the Curie point, approximately 120 °C, undergoes a phase transformation to cubic that remains stable up to 1460 °C. Above this temperature changes to a hexagonal structure [12]. At the Curie point all the titanium ions are in equilibrium positions in the centre of their octahedra. As the temperature decreases and the tetragonal phase is stable, these ions jump between energetically favourable positions in the octahedron centre [10], like Figure 2.1.1 suggests.

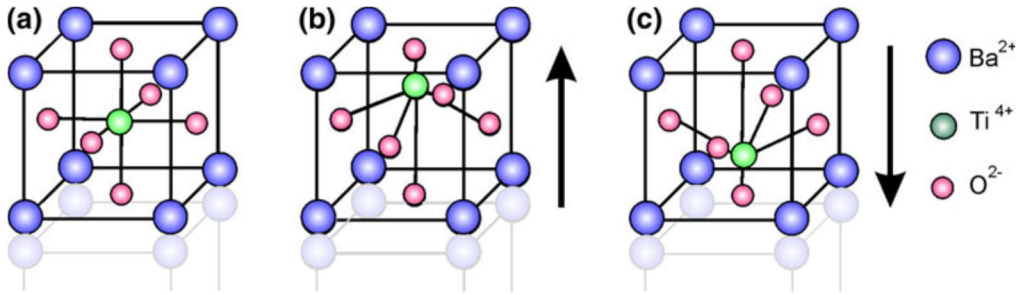

Figure 2.1.1 (a) Perovskite cubic unit cell structure barium titanate presents above Curie temperature. Below Curie temperature it presents tetragonal structure where Ti^{4+} ion displacement will shift upward (b) and downward (c) [8].

A ceramic like barium titanate is an agglomeration of small crystals fitted in a random way. As it is cooled from high temperatures to the tetragonal phase, the unit cell deforms. In order to minimize intergranular stress, domains are formed. These are regions within each grain with a spontaneously oriented dipole. It is necessary a poling treatment to make barium titanate develop a piezoelectric response. This means, an electrical field must be applied to switch the polar axes of the crystallites to the directions which are nearest to the electrical field, giving it a net dipole moment as represented in annexe A, Figure A.1. As such, the material will respond linearly to applied electrical field or mechanical pressure like a single crystal. Although, considering the random orientated crystallographic directions in a ceramic, the orientation of polar axes cannot be as perfectly aligned as it is in a single crystal. Polarization measurements indicate the fraction of single crystal polarization that can be ideally done, in other words, the dipole alignment. Regarding the effect of field poling, the remanent alignment it causes is temperature and time dependent [13]. One of the reasons many ceramics do not reach full dipole orientation is intergranular stress because it prevents the domains from switching their initial polarity orientation to more favourable directions. Well poled barium

titanate has the ability of switching the domains up to 180° into the field direction without external shape change. This way it almost remains intergranular stress free thus presenting excellent polarization. The common symmetry these materials have when poled fixes the number of independent elastic, piezoelectric and dielectric constants needed to describe it completely [9]. The constants mentioned are strongly temperature dependent [14].

The first piezoelectric documented response of barium titanate was made in 1947 by Shepard Roberts [15]. Roberts was studying $BaTiO_3$ dielectric response to biasing field strengths from 0 to 5 MV/m at different temperatures from -50 °C up to 135 °C and different frequencies. Samples above the Curie point of 120 °C followed the Curie-Weiss law for the electric susceptibility. However, for temperatures below the Curie point the same measurements indicated spontaneously polarized domains gave rise to hysteresis and remanence. By polarizing with a momentary strong electrical field at low magnetic field strength, a resonance spectrum appeared in the ceramics. The author concluded the resonance is attributed to the piezoelectric effect in polarized samples and measured the piezoelectric voltage developed upon squeezing a polarized sample of barium titanate with a vacuum tube electrometer. Despite no actual piezoelectric coefficient was measured, Roberts reports the piezoelectric voltage was found to be several volts for a force of several kilograms (not measured). Both electric field parallel to mechanical stress and electric field perpendicular to stress were observed. Some years later in 1971, the value commonly used for piezoelectric coefficient d_{33} of barium titanate was set to 190 pC N^{-1} at room temperature [9]. Since then various investigations aimed to increase this value and Shao et al. [16] reported d_{33} up to 419 pC N^{-1} of barium titanate prepared via solid state reaction method.

The conventional way to prepare barium titanate is by a solid state reaction method. It involves ball milling the analytical reagents such as $BaCO_3$ and TiO_2. The reaction starts in air by the initial formation of $BaTiO_3$ at the $BaCO_3$-TiO_2 grain boundaries, after this the process is diffusion controlled. The reaction continues as $BaTiO_3$ react to form Ba_2TiO_4 until $BaCO_3$ is used up. The remaining TiO_2 reacts with Ba_2TiO_4 to form $BaTiO_3$. The formation of Ba_2TiO_4 can be restricted below 1100 °C by CO_2 atmosphere [17]. This method may produce large $BaTiO_3$ particles with irregular morphologies due to high reaction temperature and heterogenous solid phase reaction [18]. Therefore, solid state reaction despite being simple and low waste production method, the electrical properties of the final ceramic will not be optimized.

2.2. Piezoelectricity and biocompatibility compromise

The bone itself is a piezoelectric material as Yasuda an Fukada reported in 1957 [19] with a piezoelectric coefficient of 0,7 pC N^{-1} [20]. Its capacity of generating an electrical response from a mechanical stress is how bone tissue regeneration cells are biologically stimulated. Bone is a composite of densely packed aligned collagen fibrils containing hydroxyapatite particles [21]. Collagen is the most abundant mammalian protein and has a spiral structure consisting of a triple helice [22]. The piezoelectricity in tissues such as bone is attributed to the compact alignment of these highly ordered α-helice and their inherent polarization [23]. The study by Fukada and Yasuda concluded that bone piezoelectricity appears when the shearing force acts on the oriented collagen fibres that slip past one another. Even the micromechanical stress resulting from body movement is enough to generate an electrical dipole with an opposite electric charge that can attract calcium (Ca^{2+}) and phosphate (PO_4^{3-}) ions present in body fluid [24], thus stimulating growth and enhance the implant integration with the host bone according to Wolf's law [5]. In addition the osteogenic activities which benefit bone healing are promoted by electrical signals [25].

Calcium titanate is another piezoelectric ceramic which has been used for biomedical applications and studies have confirmed that calcium titanate coatings on titanium implants promoted osteoblast adhesion compared to uncoated ones. Despite this, the same work reports results showing calcium titanate has poorer piezoelectric response than barium titanate [26]. In this sense doping barium titanate with calcium in a $(Ba_{1-x}Ca_x)TiO_3$ mixture may become a good compromise between piezoelectricity and biocompatibility. Therefore, tailored piezoelectric materials such as barium titanate doped with calcium are very promising for improving the implant performance.

The work made by Han et al. [27] reports that Ca^{2+} prefers to occupy A-sites in $BaTiO_3$ and will do so as long as Ba + Ca < Ti, but if Ba + Ca > Ti the Ca^{2+} ion could occupy B-sites. The site in which calcium ions can be integrated in barium titanate is hard to control. Zhuang et al. [28] studied the effect of Ca-acceptors on dielectric and conductivity properties of $BaTiO_3$ and observed a decrease of tetragonal distortion of the perovskite unit cell, a lowering Curie point at the incorporation of Ca^{2+} ions on B-sites. Hennings et al. [29] confirmed that Ca^{2+} ions are shifted from A-sites to B-sites by influence of BaO-excess (A/B>1). Considering the mixture $(Ba_{1-x}Ca_x)TiO_3$ Wang et al. [30] prepared a large range of different composites ($0.2 \leq x \leq 1$) and reported high piezoelectric properties in this composite for x = 0,23 being near to the solubility limit. Zhu et al. [31] also studied this mixtures and made composites from $(Ba_{1-x}Ca_x)TiO_3$ ($0 \leq x \leq 0.3$) and reported the higher dielectric strength were obtained in the x = 0.75 composition.

2.3. Hydroxyapatite

The bone major component forming 60%-70% of its mass is called natural hydroxyapatite $Ca_{10}(PO_4)_6(OH)_2$ and is used under artificial form in many biomedical applications [32]. For many years the scientific community believed that hydroxyapatite could not be piezoelectric due to its crystallization in a centrosymmetric space group in the hexagonal system [33]. Although, in 2011 Lang et al. [34] made hydroxyapatite thin films spin-coated on silicon wafers and reported the first measurements of its piezoelectric coefficient (16 pC N^{-1}), later in 2013 the same author demonstrated the piezoelectricity of sintered hydroxyapatite using PFM [35]. This can only suggest that hydroxyapatite, alongside collagen, contributes to the piezoelectricity of bone. Studies made in the beginning of the century like the one by Kobayashi et al. [36] found enhanced bone osteobonding and bone growth on polarized hydroxyapatite due to the generation of a permanent surface charge. The study reports bone growth is accelerated on negatively charged surfaces of polarized hydroxyapatite and decelerated on the positive surfaces. This may happen due to the absorption of Ca^{2+} ions that act as nuclei for calcium phosphate formation, but the mechanism is not clear. Plus electromagnetic fields accelerate bone growth as reported in studies about dielectric properties of hydroxyapatite [37]. Some work has been made in pursuit of establishing the best compound percentual relation in HP/BT composites. For instance, Zhang et al. [24] fabricated aligned porous scaffolds of HP/BT and reports that the composites made of 30%HP/70%BT and 10%HP/90%BT exhibited piezoelectric coefficient d_{33} of 1.2 and 2.8 pC N^{-1} respectively. In addition to these values being higher than the piezoelectric coefficient of bone, also both composites had no cytotoxic effects. The porosity is an important parameter knowing that a functional bone implant should be in a porous form to provide a favourable environment for bone ingrowth and osseointegration [38]. In agreement to the study previously referred Bowen et al. [39] concludes the increase of HP leads to the rapidly decrease of d_{33}, but differs concluding that composites with BT percentage below 80% do not report significant piezoelectric response. In this sense, producing a composite by mixing hydroxyapatite and calcium doped barium titanate would improve the biocompatibility and increase osteobonding. All of these are characteristics of highly importance for the work we are proposing.

2.4. Sample preparation and characterization

This work prime goal is to study the best possible calcium doped barium titanate composition with regards to its piezoelectric properties and biocompatibility. Despite this, we will start by preparing barium titanate samples by the same solid state reaction method in order to have a reference sample for all the characterization ahead and to get acquainted with the compound behaviour. After, the calcium doped barium titanate samples are prepared, hydroxyapatite will finally be mixed. There is extensive information regarding the solid state reaction method [31], [40], [41], [42], [43], [44], [45]. Authors get better milling efficiency when using planetary ball with zirconium balls and ethanol. The time in planetary mill is between 2 to 12 hours. Calcination temperatures occur between 1000 °C and 1280 °C during 2 to 5 hours. The samples are pressed into disks with 10 mm to 15 mm diameter and 0.5 mm to 2 mm thickness by pressuring at 98 MPa to 200 MPa. Sintering temperatures may go from 1280 °C to 1500 °C during 2 to 10 hours. The addition of hydroxyapatite is made before sintering. Some authors do a two-step milling, before calcination and another one after calcination and prior to sintering. Most authors prepare samples with 1:1 molar ratio but not all, most of the times not mentioning the exact parameters for different molar ratios. Hence the different values in the parameters above. Special attention must be taken regarding the heating treatments samples undergo in both calcination and sintering. Milling time is another crucial parameter that appears in the literature with some value fluctuation. High energy ball milling will considerably reduce milling time [41].

To better understand the mixtures behaviour regarding the thermal treatments in calcination and specially sintering, one can analyse the phase diagrams of both $BaTiO_3$ and $BaTiO_3$-$CaTiO_3$ as shown in annexe A, Figure A.2 and Figure A.3 respectively.

In order to characterize the mixtures regarding its properties, a series of analyses must be made as it was done in the literature mentioned above. Some of these are granulometry of the powders and mixtures to study average particle size, DSC to evaluate at which temperatures phase transformations occur. Mixtures behaviour throughout calcium substitution regarding Curie point determination can be described according to Curie-Weiss law. In equation (2.1), C is the Curie constant and T the absolute temperature. In equation (2.2), T_ϑ is the Curie temperature in the stressed state, T_0 and C_0 are the unstressed Curie temperature and constant respectively, $(Q_{11}+2Q_{12})_0$ is the value of the electrostrictive coefficient at zero temperature, α is the temperature coefficient and finally p is hydrostatic stress [28]:

$$\chi = \frac{C}{T - T_\theta} \tag{2.1}$$

$$T_\theta = \frac{T_0 - 2\varepsilon_0 p(Q_{12} + 2Q_{21})_0 C_0}{1 + 2\varepsilon_0 \alpha p(Q_{11} + 2Q_{21})_0 C_0} \tag{2.2}$$

Further structural analysis is required using XRD to identify the substitutional sites and crystal phase presence, SEM and RAMAN. Tests in vitro must be done in order to account for cytotoxicity so the samples can be labelled as qualified to polarization.

Thermally stimulated depolarization currents (TSDC) tests are a useful tool to describe the materials physical properties regarding polarization.

$$Q_p = \frac{1}{\beta}\int_{T_{initial}}^{T_{final}} J(T)d(T) \tag{2.3}$$

$$J(T) = \frac{dP(t)}{dt} = \frac{dP(T)}{dT} \times \frac{dT}{dt} = \frac{P(t)}{\tau(T)} \tag{2.4}$$

$$P(T) = \frac{1}{\beta}\int_{T}^{\infty} J(T)d(T) \tag{2.5}$$

$$\tau(T) = \frac{1}{\beta J(T)}\int_{T}^{\infty} J(T)dT = \tau_0 \exp\left(\frac{E_a}{kT}\right) \tag{2.6}$$

From equation (2.3) the polarization charge Q_p is calculated, heating rate is β and $J(T)$ is the current density as a function of temperature.

During TSDC analysis no electrical field is applied, which means current density is given by equation (2.4) where dT/dt is the heating rate β, $dP(T)/dT$ is the change in polarization with temperature [46]. Spontaneous polarization is given by equation (2.5). By equations (2.4) and (2.5) is possible to obtain the relaxation time $\tau(T)$ as described by equation (2.6).

2.5. Applications and challenges

Development of lead-free piezoelectric ceramics have been increasingly gaining interest for environment and biocompatibility reasons. Barium titanate comes as an obvious choice to be in the vanguard of such investigations due to its ability to form a strong interfacial bonding with bone and exhibits excellent biocompatibility [47]. Extended studies about in vitro biocompatibility made in 2013 by Ball et al. [7] clearly indicate barium titanate has good potential for orthopaedic tissue engineering applications. And studies by Ergun et al. [48] show that osteoblast (bone-forming cells) adhesion increased with greater $CaTiO_3$ substitutions in either hydroxyapatite or tricalcium phosphate. Considering all the studies mentioned in this work, the applications in bone tissue engineering of calcium doped barium titanate mixed with hydroxyapatite are indeed very promising.

Some of the preliminary applications could be as dental implant coatings. Dental implants procedures have increased worldwide in the last 20 years, reaching about one million dental implants per year [49]. The early osseointegrations is closely related with the clinical success of the oral implants [50], in this sense our material has a clear helpful character. But the attractiveness of this material is not reduced to dental implants, many types of implants on different bone areas struggle with osteointegration and long term clinical success. A mixture of calcium doped barium titanate and hydroxyapatite might just be a solution.

3. Materials and methods

3.1. Analytical reagents characterization

Before beginning sample synthesis all the precursor reagents were analysed in order to understand their behaviour during preparation, in particular for milling and thermal treatments. DTA-TG (Linseis STA PT1600) under flowing air was done with powder samples weighing between 15 and 20 mg and heated up to 1200 °C with 10 °C min^{-1} heating rate. Granulometry analysis in water was done using Malvern Mastersizer Hydro 2000MU after sonicating each powder for 5 minutes. And X-ray diffraction via Rigaku-DMAX III-C 3KW and PANalytical X'Pert Pro-X-ray diffractometer was done in the interval $10° \leq \theta \leq 60°$ with a 0.08° step. FTIR-Thermo Nicolet 6700 analysis was made to the analytical reagents in powder state.

3.2. Barium titanate and calcium doped BT synthesis

The analytical reagents, $BaCO_3$ (99%), TiO_2 (99%) and $CaCO_3$ (99%) provided by Honeywell Fluka, Merch and Panreac respectively were used to prepare six mixtures of $Ba_{(1-x)}Ca_xTiO_3$ with x=0, 0.1, 0.15, 0.2, 0.3 named BT, BCT05, BCT10, BCT15, BCT20 and BCT30 respectively. After being carefully weight, accounting for molar ratio after calcination, the reagents were mixed using a turbula WAB System Schatz for 20 minutes. Milling in ethanol with zirconia balls followed for 3 to 12 hours using a planetary ball mill Pulverisette 6. The mixtures were dried for 24 hours at 60 °C and filtered through a 33 µm mesh in their powder state preventing aggregation in order to optimize CO_2 release. Calcination was made at 1000°C during 4 hours in a Naber HT04116 oven. For scaffold preparation 0.5 mg of material was weighted and mixed with 40 µL of 5% PVA binder. Then pressed into 13 mm scaffolds under 150 MPa for 1 minute. Sintering in a tubular oven (TERMOLAB TH) was done between 1150 °C and 1450 °C with 5 °C min^{-1} heating rate in both air and N_2 atmospheres for 2 hours. A schematic regarding sample production methods and chronology is in annexe B, Figure B.1.

Table 3.1 Summary of prepared samples and their sintering conditions

Sample name	Theoretical composition	Sintering temperature	Sintering atmosphere
BT	$BaTiO_3$	1150 °C to 1450 °C	Air and N_2
BCT05	$Ba_{0.95}Ca_{0.05}TiO_3$		
BCT10	$Ba_{0.90}Ca_{0.10}TiO_3$		
BCT15	$Ba_{0.85}Ca_{0.15}TiO_3$		
BCT20	$Ba_{0.80}Ca_{0.20}TiO_3$		
BCT30	$Ba_{0.70}Ca_{0.30}TiO_3$		
BT/HP (90/10)	(0.9) $BaTiO_3$+ (0.1) $Ca_{10}(PO_4)_6(OH)_2$	1300 °C and 1350 °C	Air
BCT05/HP (90/10)	(0.9) $Ba_{0.95}Ca_{0.05}TiO_3$+ (0.1) $Ca_{10}(PO_4)_6(OH)_2$		
BCT10/HP (90/10)	(0.9) $Ba_{0.90}Ca_{0.10}TiO_3$+ (0.1) $Ca_{10}(PO_4)_6(OH)_2$		
BCT15/HP (90/10)	(0.9) $Ba_{0.85}Ca_{0.15}TiO_3$+ (0.1) $Ca_{10}(PO_4)_6(OH)_2$		
BT/HP (80/20)	(0.8) $BaTiO_3$+ (0.2) $Ca_{10}(PO_4)_6(OH)_2$		
BCT05/HP (80/20)	(0.8) $Ba_{0.95}Ca_{0.05}TiO_3$+ (0.2) $Ca_{10}(PO_4)_6(OH)_2$		
BCT10/HP (80/20)	(0.8) $Ba_{0.90}Ca_{0.10}TiO_3$+ (0.2) $Ca_{10}(PO_4)_6(OH)_2$		
BCT15/HP (80/20)	(0.8) $Ba_{0.85}Ca_{0.15}TiO_3$+ (0.2) $Ca_{10}(PO_4)_6(OH)_2$		

The hydroxyapatite composites were done by carefully weigh $HCa_5O_{13}P_3$ (99%) from Sigma-Aldrich in order to obtain 10% and 20% weight percentage of HP in the BT, BCT05, BCT10 and BCT15 mixtures. The materials were mixed in a planetary shaker mixer turbula for 45 minutes and pressed following the procedure mentioned in the paragraph above. Sintering in the tubular oven was made at 1300 °C and 1350 °C for 2 hours in air. Sample description is made in Table 3.1.

3.3. Sample characterization

During milling, granulometry analysis was done using the same equipment in the same conditions as the analytical reagents in order to understand the evolution of the average particle size along 3 hours milling process. Before calcination samples of all mixtures prepared in powder state were tested by the same DTA-TG used for the analytical reagents under the same conditions. After sintering the samples were submitted to different characterization techniques in order to study their atomic structures and crystallographic organization using the same X-ray diffraction equipment used for the analytical reagents in the $0° < \theta < 60°$ range using 0.08° step. FTIR-Thermo Nicolet 6700 analysis was made from 500 cm^{-1} to 5000 cm^{-1} for the analytical reagents and to the mixtures from 400 cm^{-1} to 4000 cm^{-1} after being mixed with KBr. RAMAN microscopy-Reninshaw Qontor was carried out with 1 second exposition and 0.5% of the 633 nm laser in the frequency range 0 to 1000 cm^{-1}. Samples were cracked and gold coated for SEM/EDS using Carl Zeiss Auriga SEM and Oxford Instruments EDS respectively. To better understand the implications calcium doping would have in the Curie point DSC analysis were carried out, using DSC 204 F1 Phoenix from NETZSCH, on sintered samples heating from 25 °C to 200 °C at 5 °C min^{-1} rate.

3.4. Cytotoxicity tests

To evaluate samples cytotoxicity, the assays were performed according to standard ISO-10993 “Biological evaluation of medical devices, Part 5: Tests for in vitro cytotoxicity”. Using the extract method, Vero cells (monkey renal epithelial cells) and powder state samples sintered at 1350 °C. Readings were made by Biotek ELX 800 UV instrument. Detailed explanation is made in annexe J.

3.5. Polarization and TSDC

Polarization was made in University of Aveiro, using a corona system. Samples were heated up to 110 °C and a discharge potential of -15 kV was applied in order to measure -2 kV grid potential for 1 hour. Cooling occurred for 1 hour with the same potentials applied. The equipment used during polarization is showed in annexe B, Figure B.2. The TSDC tests were made placing the sample between two electrodes connected to an electrometer Keitlhey 617 in order to record current values meanwhile heating was done from room temperature to 250 °C at 5 °C min^{-1} rate.

3.6. Bioactivity tests

Materials ability to deposit on its surface phosphate ions PO^{3-}_4 and calcium ions Ca^{2+} was studied by ICP-AES and SEM/EDS analysis. Samples were immersed for 7 days in SBF (simulated body fluid), produced as explained in annexe L. Each recipient, kept at 37 °C and under agitation, was filled with ~250 ml of SBF in direct contact with the material. Two samples of 1 ml were collected in five different time intervals. The first interval was immediately before material immersion, followed by 24 hours, 48 hours, 96 hours and 168 hours. Upon SBF trial completion, ion concentration was analysed by ICP-AES and sample surface by SEM and EDS.

4. Results and Discussion

4.1. Analytical reagents $CaCO_3$, $BaCO_3$ and TiO_2

4.1.1. Differential thermal analysis-Thermogravimetry

All three analytical reagents DTA curves are summarized in Figure 4.1.1. The DTA-TG analysis shows that $BaCO_3$ mass loss starts at 600 °C and shortly after is possible to identify two endothermic peaks as annexe C, Figure C.1 confirms. The first one located at 810 °C is attributed to the transformation of orthorhombic witherite to rhombohedral phase. The second peak spotted at 964°C marks the transformation to cubic phase [51]. Up to 1200 °C $BaCO_3$ has a 13% mass loss. Regarding TiO_2, TG results indicate no mass loss during heating as manifested in annexe C, Figure C.2. Which means there is no chemical progression of any kind in contrast with what happens in both carbonate cases. The very large endothermic progression from 320 °C to 727 °C peaks at 751°C and subsequent exothermic directed progression to 922 °C is related with surface area decrease by crystallite growth, sintering and annealing of strains. The exotherm directed peaks at 956 °C are due to the anatase-rutile transformation. The following endothermic progression peaking at 1030 °C also presents an exothermic direction as follow-up revealing more crystalline growth and annealing of strains [52]. About $CaCO_3$ mass loss is 22.6% beginning at 576 °C up to 850 °C as can be seen in annexe C, Figure C.3. This mass loss is accompanied by an endothermic large peak initiated at 694 °C, with 823 °C as maximum and ending at 858 °C. The peak in the thermogram described is related with the formation of lime (CaO) from calcite and decomposition of CO_2 [53].

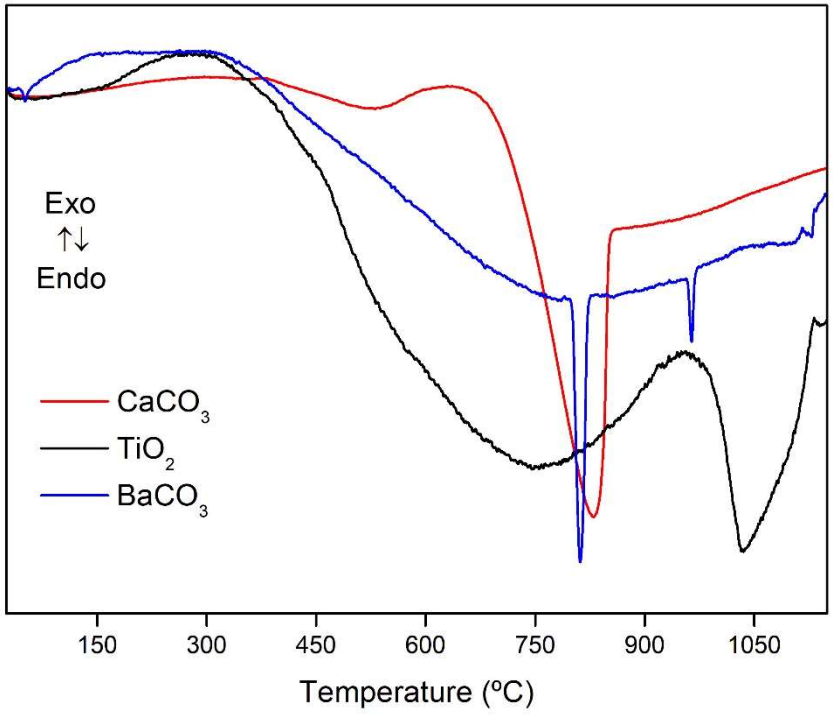

Figure 4.1.1 DTA analysis of the three analytical reagents $BaCO_3$, $CaCO_3$ and TiO_2.

4.1.2. Granulometry and X-Ray diffraction

In order to better understand the milling process, it is necessary to analyse the starting point regarding average grain size of the analytical reagents. In this sense, by sonicating each reagent in

water, it was possible to identify three different average grain sizes. As shown in Figure 4.1.2, $BaCO_3$ presented 6.6 µm particle size. The $CaCO_3$ had 7.6 µm, and the smallest TiO_2 indicated 0.6 µm.

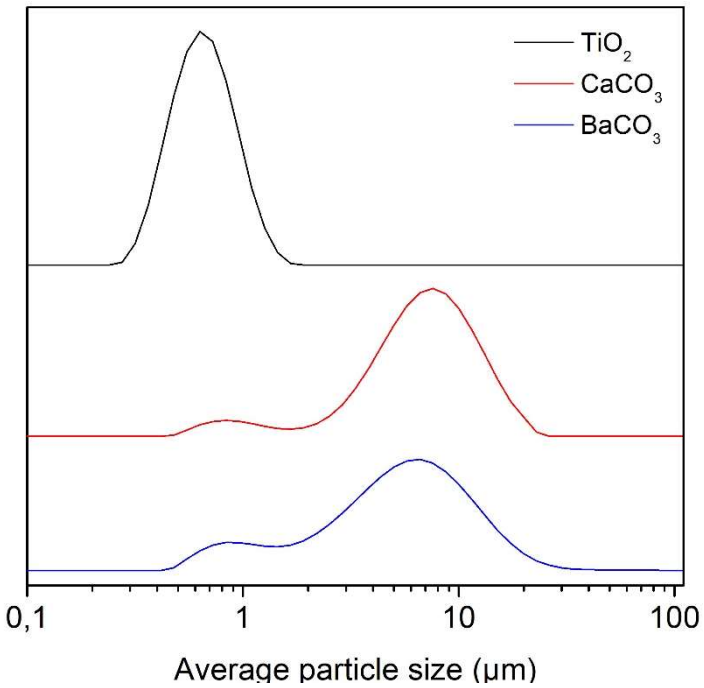

Figure 4.1.2 Granulometry analysis of the three analytical reagents $BaCO_3$, $CaCO_3$ and TiO_2.

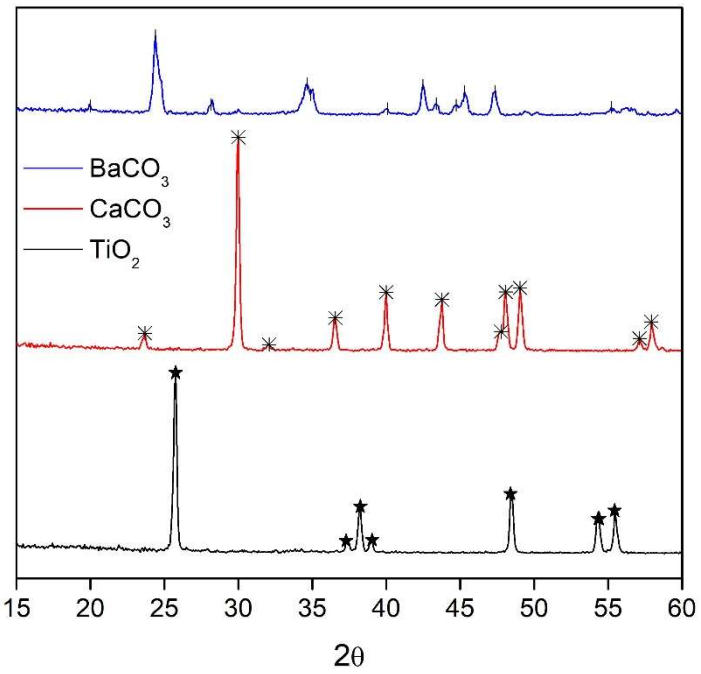

Figure 4.1.3 XRD of $BaCO_3$, $CaCO_3$ and TiO_2 powder. ★ tetragonal anatase, ✳ rhombohedral calcite and l orthorhombic witherite.

X-Ray diffraction of the analytical reagents in Figure 4.1.3 shows the three crystalline phases expected from non-sintered powder samples. Tetragonal anatase is correspondent to TiO_2 diffractogram identified by ICDD 00-021-1272. Rhombohedral calcite is present in $CaCO_3$ as ICDD 00-005-0586 suggests and orthorhombic witherite $BaCO_3$ is finally identified by ICDD 00-045-1471.

4.1.3. FTIR

Given the fact that TiO_2 is not a carbonate, its FTIR spectrum does not present clear peaks since carbon linked bands do not exist in this molecule thus there is no vibrations to be taken under consideration. On the other hand, $CaCO_3$ and $BaCO_3$ being carbonates, the vibrations these molecular links produced are present in their FTIR spectrum in Figure 4.1.4.

On $CaCO_3$ analysis the peaks present in 879 cm^{-1} and 1424 cm^{-1} to 1492 cm^{-1} are related with the normal modes of vibration of planar XY_3 molecules [54]. The peak spotted at 3639 cm^{-1} is probably due to a combination band where two fundamental bands absorb at two different energy simultaneously or an overtone of the band indicated by the first peak. Regarding $BaCO_3$ the peaks shown at 692 cm^{-1}, 857 cm^{-1}, 1059 cm^{-1} and 1749 cm^{-1} are attributed to the stretching and deformation vibration modes of carbonate ions [55]. Once again, the low frequency peak at 2452 cm^{-1} is likely related to overtone or combination band.

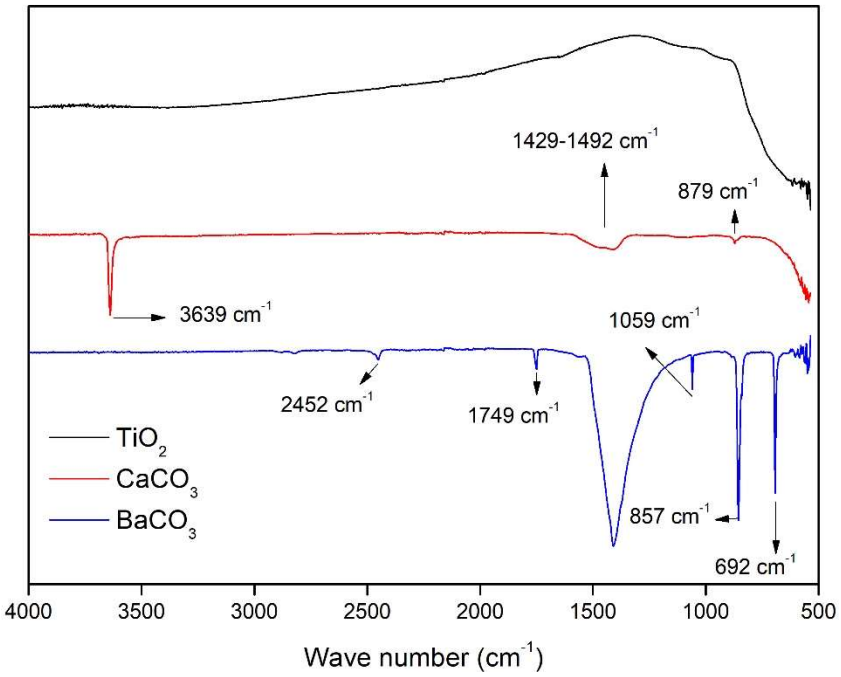

Figure 4.1.4 FTIR analysis of each $BaCO_3$, $CaCO_3$ and TiO_2 analytical reagents in powder state.

4.2. Calcium doped BT mixtures

4.2.1. DTA-TG and Granulometry

The thermal behaviour of BT endothermic progression associated with weight loss from 813 °C to 940 °C is attributed to the continuous transformation of orthorhombic $BaCO_3$ to rhombohedral phase and subsequent formation of $BaTiO_3$ according to equation (4.7), hence such a large endothermic domain. Weight loss of 11% starts at 714 °C and endures up until 943 °C related with CO_2 release [56]. The formation of Ba_2TiO_4 according to equation (4.8) is also likely to happen knowingly that the powder was not calcinated before DTA-TG analysis. These reactions overlap and that is probably the reason why in Figure 4.2.1 is noticeable a very large endothermic region [57]. This proves the importance of an efficient calcination process if no reductive atmosphere is to be used during sintering.

$$BaCO_3 + TiO_2 \rightarrow BaTiO_3 + CO_2 \quad (4.7)$$

$$BaTiO_3 + BaCO_3 \rightarrow Ba_2TiO_4 + CO_2 \quad (4.8)$$

Regarding BCT30 sample, the TG curve shows a continuous weight loss of 20% from 580 °C to 932 °C. There is an exothermic peak at 611 °C that is present in the thermograms of all mixtures containing calcium as annexe C, Figure C.4 proves. The exothermic peak mentioned is related with crystallization of the calcite phase after completing thermal dehydration [58]. From BT to BCT20 sample thermograms show a very similar endothermic behaviour presenting a very large region stretching from 820 °C to 940 °C implying there are multiple overlapping reactions taking place at those temperatures, not only equation (4.7) and equation (4.8), but also the formation of $Ba_{1-x}Ca_xTiO_3$ according to equation (4.9). BCT30 is the only sample to present a narrower endothermic region peaking at 890 °C. According to XRD results present in section 4.2.2, this might be due to the formation of orthorhombic $CaTiO_3$ according to equation (4.10), indicating there is a limit to which calcium can dope barium titanate without compromising its structure by forming different phases. Weight loss of all samples are listed in Table 4.2. There is a clear increasement of mass loss from no calcium substitution to 5% molar substitution. In section 4.1.1, DTA-TG analysis of the carbonate analytical reagents show there is more mass loss in $CaCO_2$ than in $BaCO_2$. Suggesting the presence of calcium in the mixture should translate in larger mass loss. These values maintain throughout the remaining samples except for BCT15.

$$(1-x)\ BaCO_3 + (x)\ CaCO_3 + TiO_2 \rightarrow Ba_{1-x}Ca_xTiO_3 + CO_2 \quad (4.9)$$

$$CaCO_3 + TiO_2 \rightarrow CaTiO_3 + CO_2 \quad (4.10)$$

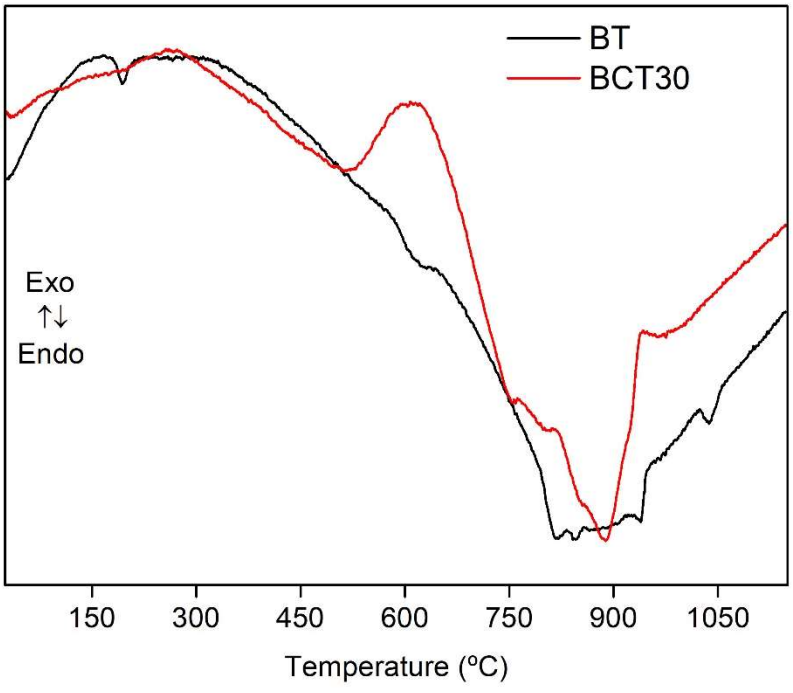

Figure 4.2.1 BT and BCT30 differential thermic analysis in order to compare the behaviour of the highest calcium substituted material and no calcium substituted material.

A study regarding the weight loss during calcination at 1000 °C for 4 hours was also made. The results present in Figure 4.2.2 show that as the molar percentage of calcium increases so does the weight loss. These results, as mentioned before, indicate that $CaCO_3$ is more reactive to high temperature than $BaCO_3$ in the sense that more CO_2 is released. This goes in agreement with the results given by TG analysis of BT and BCT30. But there is an important factor to be taken under consideration regarding weight loss, that is average particle size. From Table 4.2 the average particle size in BT and BCT30 are both 3.8 µm after 3 hours milling but this is not true for BCT15, that presents 5.0 µm size and loses 10% weight during DTA analysis. Smaller particle size implicates larger surface area in contact with hot air, for that reason it increases temperature reactivity. Since the samples submitted to DTA-TG analysis did not went under calcination process before being heated up to 1200 °C, samples containing calcium lose more weight during heating.

Table 4.1 Granulometry analysis results for milling time and correspondent average particle size of BT mixture.

Mixture	**BT**			
Milling time (hours)	3	6	9	12
Average particle size (µm)	3.8	3.3	2.9	1.5

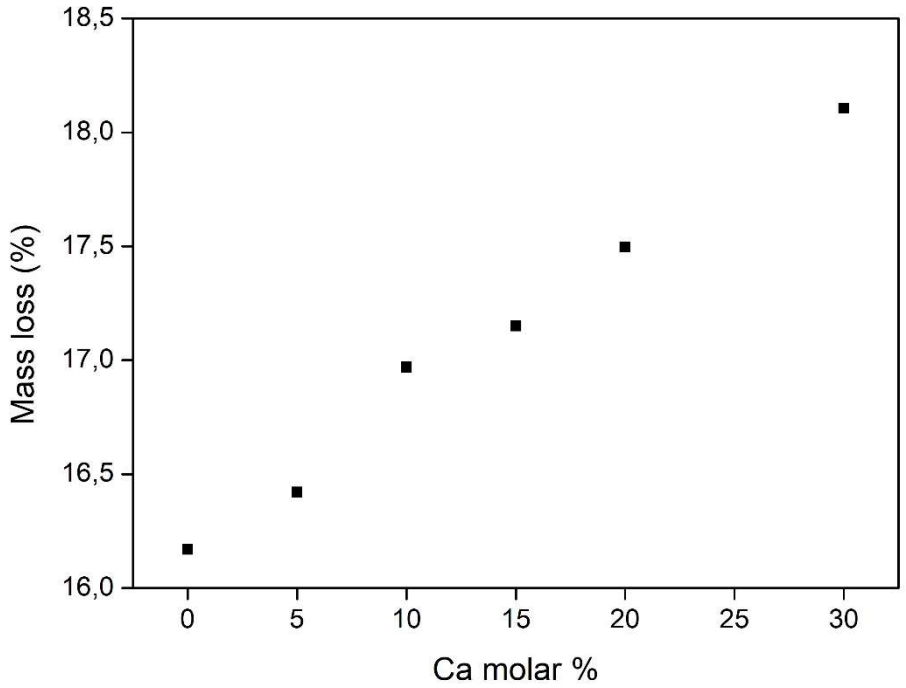

Figure 4.2.2 Mass loss (%) in function of calcium presence along the calcination process with a 5 °C min^{-1} heating rate from room temperature up to 1000 °C remaining at the highest temperature for 4 hours.

The BT mixture was first ball milled up to 12 hours with samples being taken every 3 hours for particle size analysis. Results showed an evolution from 3.8 µm to 1.5 µm between the interval. The following results reported in this work are made from mixtures ball milled for 3 hours. Table 4.1 shows the relation between average particle size and milling time for BT mixture.

Table 4.2 Average particle size (µm) for every mixture prepared. Results were obtained by granulometry analysis made in water.

Mixture	**BT**	**BCT05**	**BCT10**	**BCT15**	**BCT20**	**BCT30**
Average particle size (µm)	3.8	3.8	3.6	5.0	2.9	3.8
Weight loss up to 1200 °C (%)	11	19	20	10	23	20

4.2.2. X-Ray Diffraction

Analysing Figure 4.2.3 is noticeable that tetragonality in BT is assured (ICDD – International Centre for Diffraction Data 05-0626) and there is no evidence that using N_2 atmosphere during sintering might significantly change crystal structure since the peaks found in both samples are the same. Although, for BCT30 samples, there is clear presence of a tetragonal $Ba_{1-x}Ca_xTiO_3$ specimen, it is also spottable orthorhombic $CaTiO_3$ (ICDD 22-0153) indicating that $CaCO_3$ did not react to full extend forming $Ba_{0.7}Ca_{0.3}TiO_3$ and instead $CaTiO_3$ residue was left. Just like BT samples, BCT30 diffractogram does not indicate any variability between air and N_2 atmosphere during sintering regarding tetragonality assurance or supressing $CaTiO_3$ formation [59]. Another important remark is the existing shift to higher angles on BCT30 samples. This means the cell unit volume is shrinking and it can be explained by Ca^{2+} ions presenting smaller ionic radius and replacing Ba^{2+} with bigger ionic radius at CN = 12 site in $BaTiO_3$ lattice maintaining a tetragonal phase [31].

Sintering temperature plays an important role in crystal conformation and as such, tetragonal phase is better achieved and maintained when samples are submitted to high temperatures during sintering [45]. This importance becomes clear in X-ray diffraction, since the evolution of sintering temperatures from 1150 °C to 1350 °C is accompanied by the formation of two double peaks on the diffractograms near 2θ values of 45° and 57° as annexes E, Figure E.1 and Figure E.2 show. In the first figure (E.1) there are different diffractograms of BT mixture are present, temperatures from 1150 °C to 1250 °C show peaks correspondent to cubic $BaTiO_3$ identified by ICDD 031-0174. Diffractograms of samples with sintering temperatures above 1300 °C have both distinguished double peaks that identify tetragonal $BaTiO_3$ by ICDD 01-083-1878. The second figure (E.2) shows a similar evolution as mention above, but in this case the second double peak located around 2θ = 57° is not so evident. Moreover, there is some small peaks indicating the presence of orthorhombic $CaTiO_3$ unrelated with sintering temperature evolution as expected.

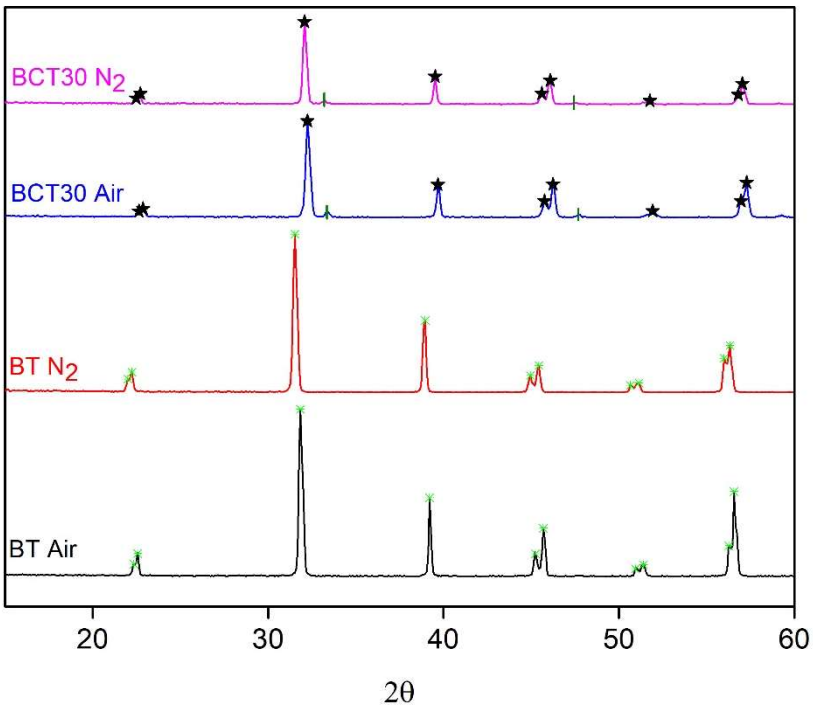

Figure 4.2.3 X-Ray diffraction of BT and BCT30 mixtures sintered at 1350 °C in both air and N_2 atmospheres. ★ tetragonal $Ba_{(1-x)}Ca_xTiO_3$, l orthorhombic $CaTiO_3$ and ✳ tetragonal $BaTiO_3$.

The remaining 1350 °C sintered mixtures diffractograms do not show signs of either $CaTiO_3$ or tetragonality loss. Despite this, there is a double peak formation from a single peak only on sample BCT15 located close to 2θ = 38° presented in annexe E, Figure E.3. It might indicate the presence of TiO by ICDD 98-0020-3331. These results show there is an incomplete solid solubility of Ca^{2+} in $BaTiO_3$ lattice on, at least, BCT30 samples.

4.2.3. FTIR

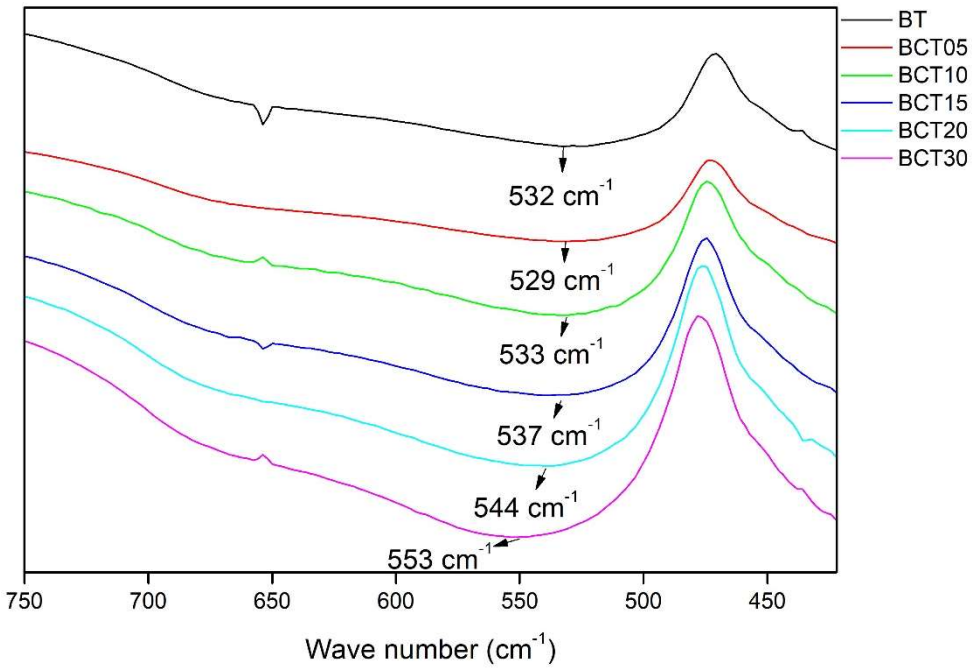

Figure 4.2.4 FTIR analysis of every $Ba_{1-x}Ca_xTiO_2$ compounds mixed with KBr.

In Figure 4.2.4 FTIR analysis of samples sintered at 1350 °C are shown. In BT spectrum there is a strong absorption peak at 532 cm^{-1} attributed to the stretching vibration of Ti-O bond, these modes of vibration and the spectrum are represented in annexes F, Figure F.2 and Figure F.1 respectively. There is great importance in this stretching normal vibration mode since its direction is the same as spontaneous polarization of tetragonal $BaTiO_3$ phase [60]. The FTIR spectrums of $Ba_{1-x}Ca_xTiO_3$ ($0 \leq x \leq 0.3$) mixtures are similar but BCT05 absorption peak wave number is smaller than BT, the first is 529 cm^{-1} and the last 532 cm^{-1}. XRD analysis in section 4.2.2 show a tetragonal perovskite structure (ABO_3). As such, when Ca^{2+} ions are doped most occupy A-site substituting Ba^{2+} but some occupy B-sites where Ti^{4+} was present before. This last substitution implies a weaker coulomb interaction with O^{2-} ions since the old electrical charge of Ti^{4+} is greater than the new Ca^{2+}, resulting in an energy decrease of O-B (B is the ion at B-site) bond [61].

Figure 4.2.4 also shows that from BCT05 to BCT30, the increase of Ca percentage reflects in a wave number increment from 529 cm^{-1} to 553 cm^{-1}. The unit cell volume decreases due to preferable substitution of Ca in A-site, as confirmed by XRD results. The increasing Ca substitution is associated with angle value increments proving there is crystal planes approximation by ion radius shortage since Ca^{2+} has a smaller ionic radius than Ba^{2+}. As a result, Ti-O bonds also shorten shifting the aborting peaks in FTIR spectrum to higher frequencies. Figure 4.2.5 shows absorption peaks in function of Ca percentage in the mixture [61].

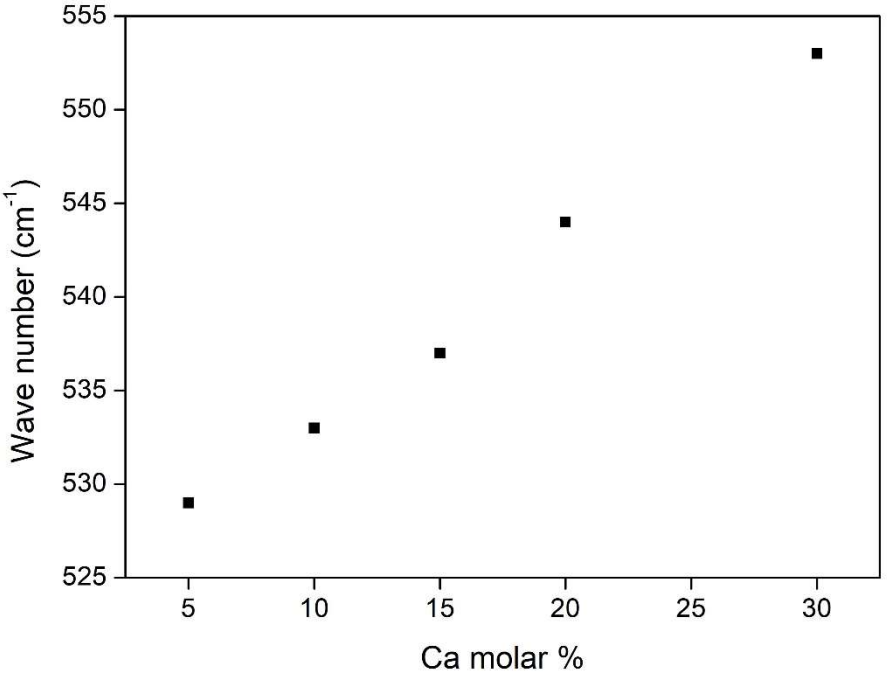

Figure 4.2.5 Relation between FTIR absorption peaks and calcium substitution.

4.2.4. RAMAN

For samples sintered at 1350 °C, Figure 4.2.6 presents barium titanate RAMAN spectrum at room temperature and it shows optical phonon frequencies and their mode symmetry assignments (some presented in annexe G, Figure G.5) in $BaTiO_3$ that indicate tetragonality characteristic such as 168 cm^{-1} A_1[TO2], 266 cm^{-1} A_1[TO1], 309 cm^{-1} B_1 and E[TO+LO], 470 cm^{-1} A_1[LO], 520 cm^{-1} A_1[TO4] and 720 cm^{-1} A_1[LO] [62], [63]. The introduction of calcium in the mixture reflects on the spectrum in different senses like, the vibration mode A_1[TO1] (168 cm^{-1} for BT sample) peak shifts to lower frequencies and both B_1 and E[TO+LO] peak (309 cm^{-1} for BT sample) become larger to the point of being unnoticeable, as annexe G, Figure G.1 suggests. These evolutions go in agreement with previous studies [64] that point to changes on phonon vibrations of Ti-O bonds due to Ca^{2+} presence. Another important alteration, as calcium fraction increases, is the sift to higher frequencies of A_1[TO4] and A_1[LO] correspondent to 720 cm^{-1} peak in BT. In this case local disorder regarding Ti^{4+} position due to the substitution of ions with different radius and subsequent force constant increase are responsible for peak shifting to higher frequencies and broadening [64].

If there was significant substitution of Ca^{2+} ions in Ti^{4+} site it should be noticeable a peak close to 800 cm^{-1} A_{1g} octahedral breathing mode since it is RAMAN inactive for single B-site species [65]. There is no evidence on what was mentioned before and alongside with XRD and FTIR, Raman analysis indicates the large majority of Ca^{2+} ions are substituting Ba^{2+} ions and not Ti^{4+} on $Ba_{1-x}Ca_xTiO_3$. Despite this, it is important to notice BCT20 and BCT30 show almost no evidence of some tetragonal optical phonon vibrations like B_1 and E[TO+LO], also these samples show large shift and broadening of key peaks like the ones corresponding to A1[TO1] modes of vibration. Indicating their tetragonality is somewhat doubtful. Annexe G, Figure G.2 has the mixture spectra that maintain all the peaks.

Raman microscopy of every unpolished sample reveals very heterogenous grain size throughout the same sample confirmed by annexe G, Figure G.4. It is also noticeable the average grain size in BT is greater than BCT05 and BCT10. BCT15 has similar size to BT but decreases for BCT20 and BCT30. It is possible to clarify there is no significant difference in the Raman spectrum of samples sintered at 1350 °C and 1450 °C, comparing annexe G, Figure G.1 and Figure G.3 confirms.

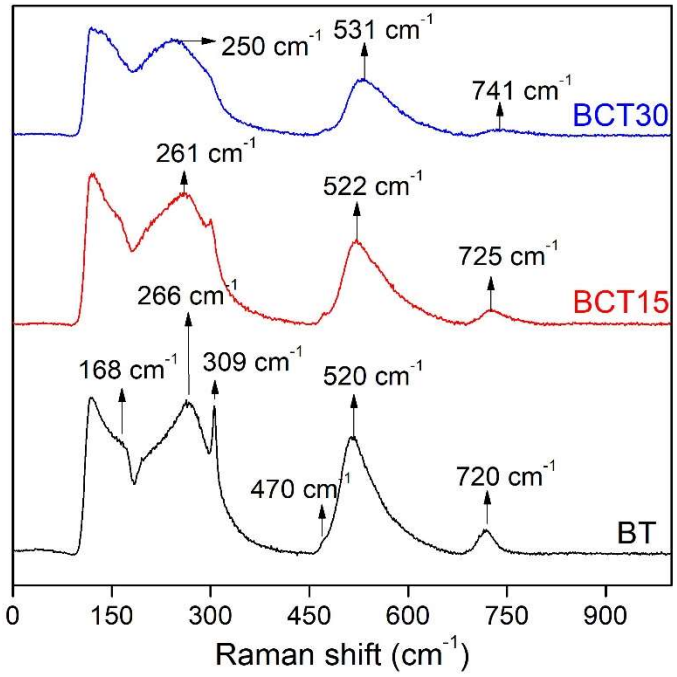

Figure 4.2.6 Raman analysis of BCT30, BCT15 and BT samples.

4.2.5. DSC

The following measurements were made after the structural studies mentioned before in order to understand the temperature evolution at which structural transformation takes place from tetragonal phase to cubic (i.e.) Curie point along calcium substitution. The following samples were previously sintered at 1350 °C. Taking into consideration T_c values were obtained while heating the samples and not cooling, the results are represented in Figure 4.2.7. BT sample show T_c of 125 °C as literature suggests [9]. As expected, small amounts of calcium substitution up to 15 molar percentage, show little to no difference regarding the evolution of T_c. Nonetheless, BCT20 and BCT30 peaks present broadening and a shift toward lower temperatures like 118 °C and 111 °C respectively. Figure 4.2.8 represents the direct relationship between T_c and calcium substitution. The notorious effect in BCT20 and BCT30 is caused by lattice distortion confirmed by XRD, FTIR and Raman analysis. It was discussed above that despite the majority of Ca^{2+} ions are replacing Ba^{2+} ions, there is some residual quantity of the first ions replacing Ti^{4+} in the unit cell. This residual percentage of B-site occupation logically increases with the increasing calcium substitution. It is possible to understand the unit cell deformation caused by a compressive stress *p* on the adjacent unit cell due to substitution as shown in annexe H, Figure H.1.

Looking at equation (2.2) in section 2.4, it becomes obvious the Curie temperature under stress T_ϑ will decrease linearly while the hydrostatical stress *p* increases, just like what the DSC results here reported suggest.

It seems to be clear there is a calcium substitutional limit in $Ba_{(1-x)}Ca_xTiO_3$ if the objective is to ensure the material tetragonal characteristics. Taking into consideration the studies made so far in this report, that limit must be under 20% molar substitution of calcium. Which leaves BT, BCT05, BCT10 and BCT15 the samples where is possible to assure tetragonal phase characteristics are not compromised making it possible to polarize and be piezoelectric efficient. In addition, the effect of

sintering temperature on tetragonal to cubic phase transitions in both BCT20 and BCT30 is clarified by the absence of clear peaks on DSC spectrums indicating the difficulty in achieving tetragonal phase at room temperature if samples are not submitted to sintering temperatures above 1300 °C as demonstrated in annexe H, Figure H.2 and Figure H.3

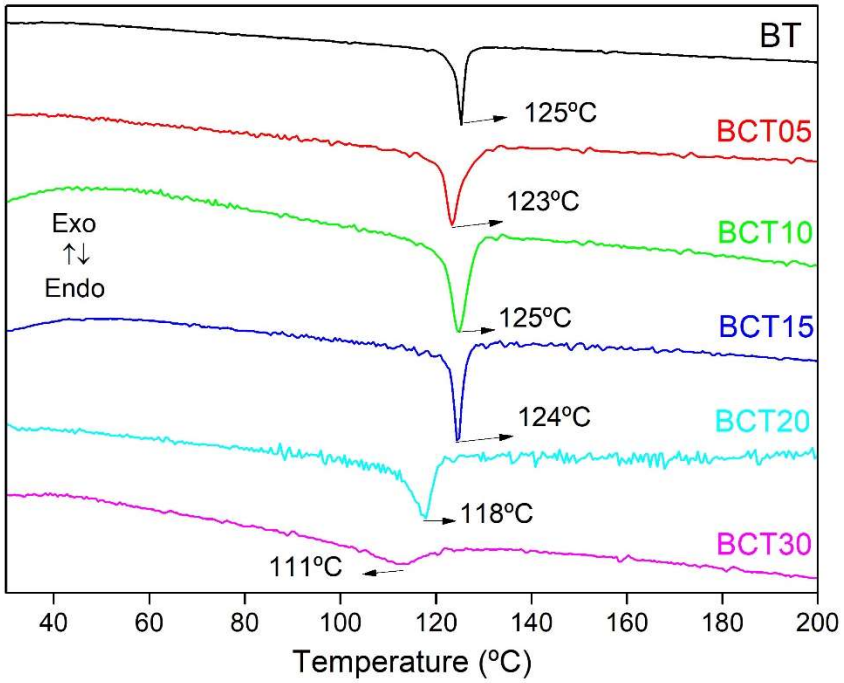

Figure 4.2.7 Differential scanning calorimetry analysis to all the $Ba_{1-x}Ca_xTiO_2$ mixtures in order to obtain the Curie point for each one.

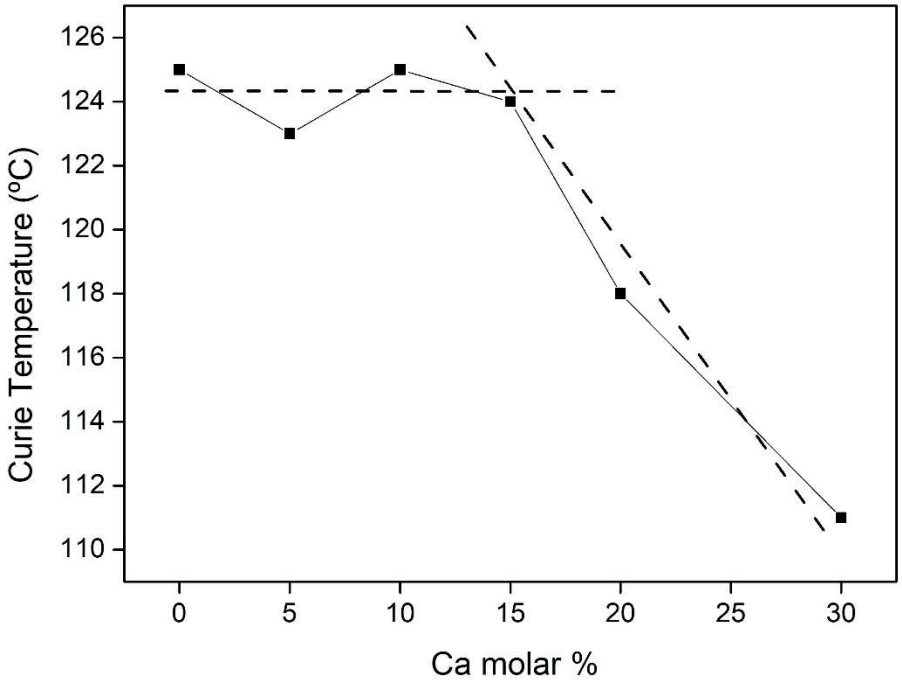

Figure 4.2.8 Evolution of Curie point in function of calcium molar percentage.

It might be possible to achieve a stable tetragonal phase with relative elevated Curie point for $Ba_{(x-1)}Ca_xTiO_3$ with x > 15% but it requires much higher sintering temperatures. This way, atoms may have enough time and energy to arrange themselves in the unit cell without increasing hydrostatic

pressure too much and consequently decreasing Curie point to the point of almost inexistence as BCT30 in Figure 4.2.7 demonstrates. However, there are other obstacles regarding high temperature sintering in order to optimize piezoelectric properties like over-sized grain domains that promote back switching [66], jeopardizing polling treatments efficiency and thus the material main purpose.

4.2.6. SEM and EDS

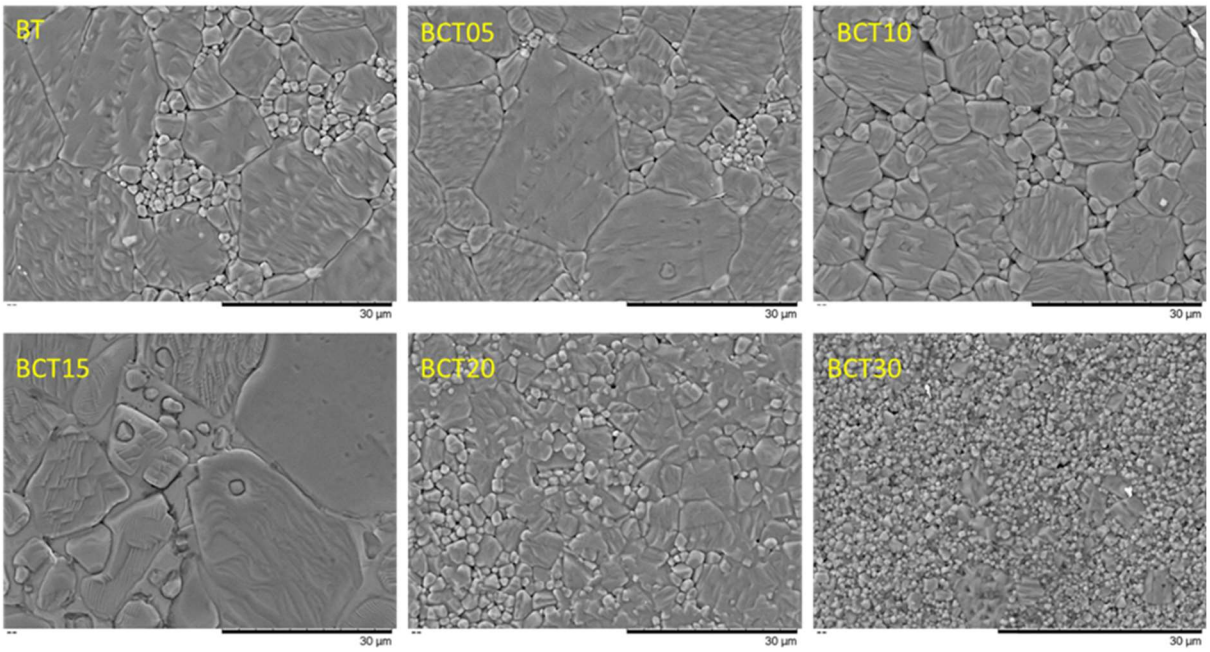

Figure 4.2.9 SEM showing different grain sizes in $Ba_{(1-x)}Ca_xTiO_3$ $0 \leq x \leq 0.3$.

Calcium doped barium titanate mixtures under SEM in Figure 4.2.9 show a decrease of grain size as calcium presence increases, which agrees with the information present in the literature [31], [67]. A similar effect using barium titanate produced by two-step sintering is reported by Zhao *et al* [68]. This author states that smaller and specially more uniform grain size will result in higher breakdown strength and internal resistance, since there is a more homogenous electrical field concentration along the sample if grain size is more uniform. In this work, however, the cause for grain uniformization is the presence of calcium as an impurity and not improvement of sintering efficiency on the same material. More calcium appears to inhibit grain growth, thus resulting in a more uniform grain size distribution as calcium percentage increases. Sample BCT15 SEM image on Figure 4.2.9 shows larger grain size probably to higher particle size after milling as mentioned in section 4.2.1 and seems to have a different phase formation between grains. This may be due to TiO presence confirmed by XRD, as shown in annexe E, Figure E.3.

Some samples like BT, BCT15 and BCT30 surface after being polished using down to ¼ µm diamond paste are shown in annexe I, Figure I.1. It is clear there is some porous with heterogenous sizes and shapes, but overall samples do not reveal a high porosity. Sample BCT30 SEM image has noticeable small darker shapes that indicate, via EDS mapping and quantification, the presence of high calcium formations in annexe I, Figure I.2. These results combined with what can be found in XRD analysis in section 4.2.2 confirm the possibility of $CaTiO_3$ phase formation.

4.2.7. Cytotoxicity

These assays were done using extraction method where Vero cells are put in contact with medium where the different samples were incubated in. After 48 hours in the incubator, a viable cell

count is made using a colorimetric method based on resazurin. Due to the impossibility of using disk like samples in cytotoxic assays, 100 mg of powder samples were sintered at 1350 °C and pre-sterilized with UV radiation for 1 hour. Powders were then placed in 2.5 ml of medium at 37 °C for 48 hours. Positive, negative and medium controls were also made in order to calculate cell viability. Resazurin is blue collared and is reduced by metabolic active cells into pink collared resorufin. As such the conversion from resazurin to resorufin is proportional to metabolic active cells under certain limits like incubation time or cell density. It is possible to evaluate cell activity through fluorescence since resazurin has absorbance maximum at 570 nm and resorufin at 600 nm.

$$Cell\ viability = \frac{number\ of\ cells\ under\ inderect\ contact\ with\ samples}{number\ of\ cell\ in\ the\ negative\ control} \times 100 \qquad (4.11)$$

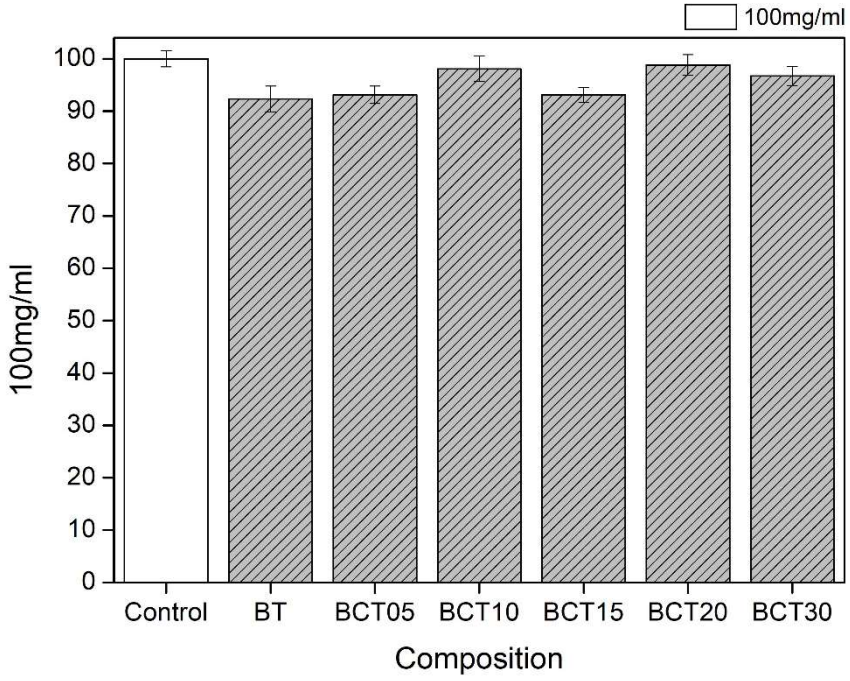

Figure 4.2.10 Cytotoxicity results for all $Ba_{1-x}Ca_xTiO_3$ mixtures and the control with correspondent error bars.

The potential cytotoxic effect of all mixtures in powder state sintered at 1350 °C was studied and results present in Figure 4.2.10 were calculated from equation 4.11 and are expressed under cell viability in percentage (%). From an extract concentration of 100 mg/ml, with 2% uncertainty, 5 replicas from every samples were made. In annexe J, Figure J.1 it is shown the sample distribution along the plate. Control medium revealed 100% cell viability, as such, it was used as reference throughout the rest of the tests. The sample that revealed the lowest cell viability was BT with 92±2%. BCT05 and BCT20 samples followed revealing 93±2% cell viability, BCT30 was second highest with 97±2% and BCT10 presents 98±2% Vero cells viability. Since all samples show cell viability above 90%, it is secure to assume these materials are non-cytotoxic. Literature information is scarce about this topic, but Ahmadi *et al* [69] have very recently reported calcium doped barium titanate to be non-cytotoxic and to improve MG63 osteoblast-like cell viability as calcium substitution increases up to 20% atomic ratio.

4.2.8. Thermally stimulated depolarization currents

The most commonly used technique to polarize ferroelectric ceramics is by contact polarization. Electrodes are deposited on the sample surface and after it is immersed in oil bath while applying a large electrical field at constant temperature. This method has some disadvantages. Local break down at weak spots, such as pinholes, may short-circuit the electrodes disabling further poling, plus samples cease to be fit to use under biomaterials applications standards once electrodes are contaminating it and oil washing off is an inconvenient process. On the other hand, corona polarization method does not require electrode deposition nor oil bath immersion. Charges from the corona tip (point) flow through the sample creating an electrical field between both surfaces. Surface potential can be measured using an electrostatic voltmeter [70].

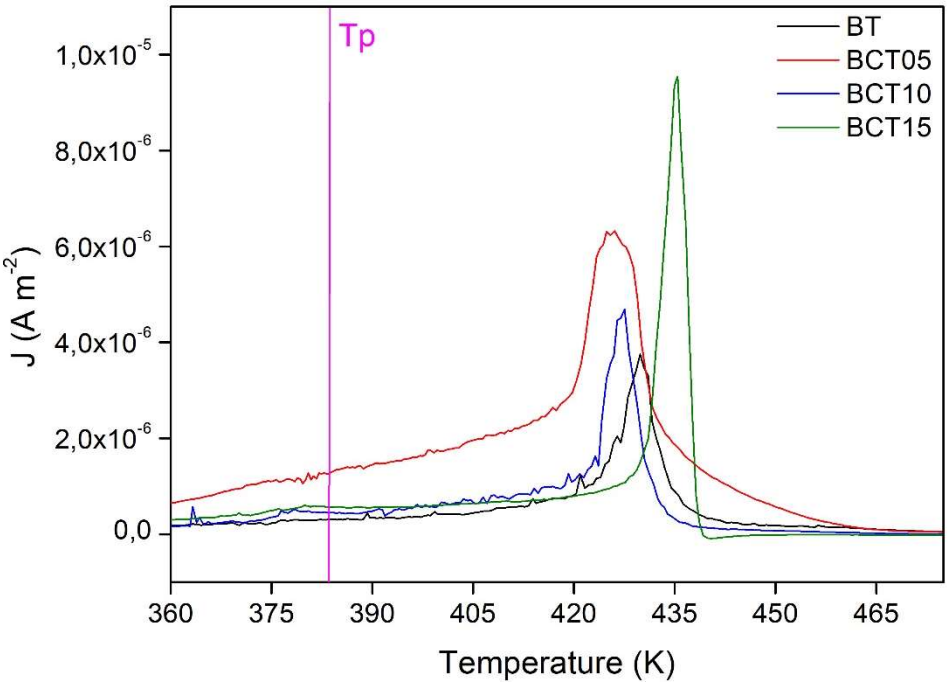

Figure 4.2.11 Thermally stimulated depolarization currents of $Ba_{(1-x)}Ca_xTiO_3$ $0 \leq x \leq 0.15$ polarized samples and polarization temperature marked as Tp.

Despite cytotoxicity results revealed all mixtures to be non-cytotoxic and thus all materials qualify to polarization, results given by XRD, FTIR, Raman and DSC show it would be inefficient to polarize mixtures such as BCT20 and BCT30 since their crystal tetragonal conformation is compromised. Under this assumption, polarization was only done to $Ba_{(1-x)}Ca_xTiO_3$ $0 \leq x \leq 0.15$ mixtures. TSDC spectrums of these samples are in Figure 4.2.11 and polarization temperature is represented by a pink line at 110 °C.

Each mixture spectrum is individually represented by a polarized and depolarized sample as annexe K, Figure K.1 shows. This figure clearly indicates sample depolarization was achieved since the depolarized samples are represented by a flat line in the spectrum and polarized samples have a well-defined peak. In TDSC spectrum of non-polarized samples, there are two very sharp and low current density double peak above Curie point, between 160 °C and 180 °C for calcium substituted samples and between 150 °C and 160 °C for BT as can be seen in annexe K, Figure K.2. These peaks exist in both positive and negative directions (current reversal), hence double peak, are probably related to a pyroelectric current due to the late ferroelectric-paraelectric phase transition [71]. For BT. the anomalous pyroelectric current can be easily identified near 156 °C in a polarized sample at much higher current density, about 2×10^{-5} A cm^{-2}, than compared with a non-polarized sample at about

4×10^{-9} A cm^{-2} as annexe K, figure K.3 suggests. Moreover, on polarized samples there is no double peak, like the ones present in non-polarized samples thermograms, where the current is 3 orders of magnitude lower, precisely because most electrical dipoles are oriented in the same direction. This direction being the electrical field direction when it was applied to samples during corona polarization. On non-polarized samples, dipoles are spontaneously oriented in different directions as the ferroelectric state dissolves into the paraelectric state.

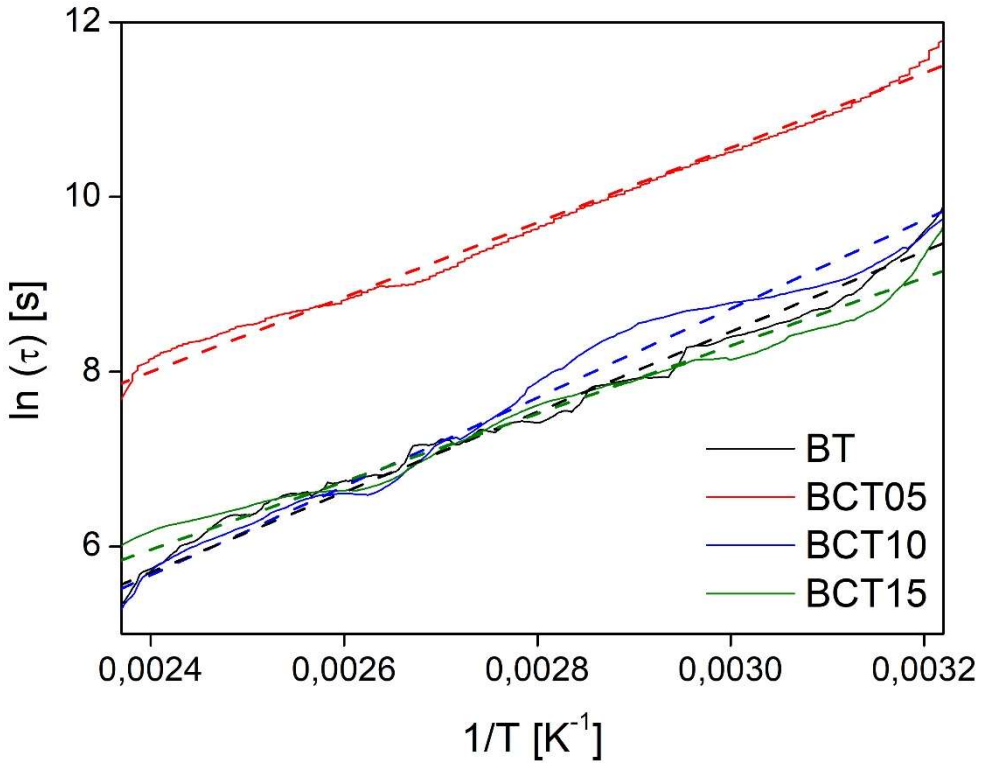

Figure 4.2.12 Linear fit done from equation 4.13 and 1/T combination to calculate the activation energy and τ_0 of polarized samples. Dashed lines represent the linear fit done from the original curves.

From the spectra above is possible to calculate a series of parameters in order to describe the materials behaviour mathematically and understand their physical meaning. Assuming the relaxation time τ can be described by an Arrhenius law, τ_0 is the pre-exponential factor, E_a is the activation energy and k the Boltzmann constant, by combining equation (2.6) present in section 2.4 and equation (4.12), results equation (4.13). From the last equation is possible to calculate the activation energy and τ_0 by the linear fit slope and intercept, respectively, of the curve given by the right side of equation (4.13) in function of the temperature inverse. On Figure 4.2.12 the lines describing polarized sample behaviour are shown and results are in Table 4.3. The highest polarization charge value belongs to BCT05 by some margin compared with the remaining mixtures, this could be expected by analysing the peak areas in Figure 4.2.11.

$$\tau(T) = \tau_0 \exp\left(\frac{E_a}{kT}\right) \tag{4.12}$$

$$\frac{E_a}{kT} + \ln \tau_0 = \ln\left[\frac{1}{\beta}\int_T^{\infty} J(T)d(T)\right] - \ln J(T) \tag{4.13}$$

Another important consideration on BT polarization are oxygen vacancies cause by charge migration that are closely related with polarization fatigue in ferroelectrics and normally are revealed by large and high intensity peaks around temperatures of 200 °C and 300 °C [68]. Meaning that oxygen vacancies and their possible clusters tend to increment the activation energy calculated from TSDC analysis by opposing dipole reorientation [72]. Most works in the literature about BT polarization report activation energies close to 1 eV [46] precisely due to the presence of oxygen vacancy. Although during TSDC analysis here reported samples were not heated to temperatures above 250 °C, there are no peaks after 162 °C until the end of the spectrum. Thus, not indicating high oxygen vacancies or clusters concentration, resulting in lower activation energy values as Table 4.3 states.

Table 4.3 Depolarization parameters from TSDC analysis.

	T_{peak} (K)	J_{max} (A m^{-2} × 10^{-6})	Q_p (C cm^{-2} × 10^{-4})	E_a (eV)	τ_0 (s × 10^{-3})
BT	430	3.74	7.81	0.40±0.01	4.89±0.01
BCT05	425	6.33	23.3	0.37±0.01	104±0.08
BCT10	427	4.71	8.50	0.44±0.01	1.47±0.01
BCT15	435	9.64	1.15	0.34±0.01	24.97±0.04

4.3. Hydroxyapatite and calcium doped BT composite

4.3.1. X-Ray Diffraction

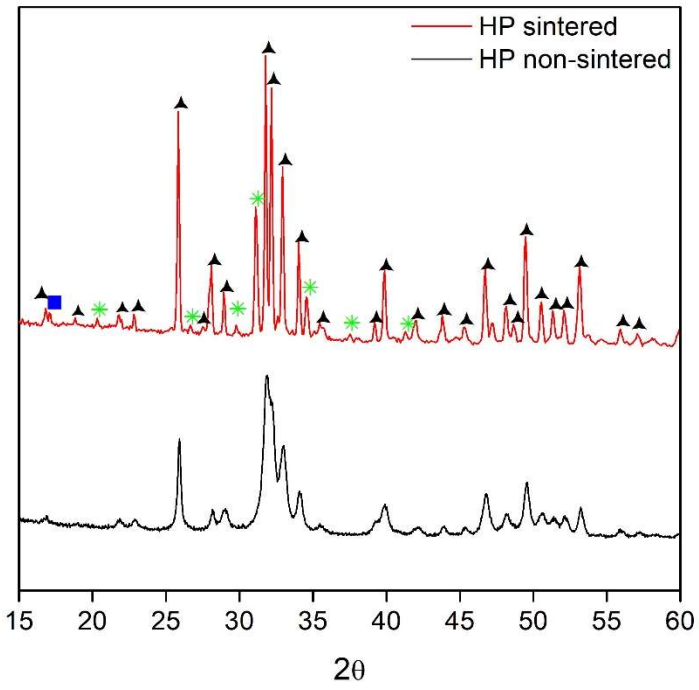

Figure 4.3.1 X-ray diffraction of 1350 °C sintered and non-sintered commercial hydroxyapatite. ▲ Hydroxyapatite, ■ β-TCP and ✳ α-TCP.

In Figure 4.3.1, XRD analysis of both 1350 °C sintered and non-sintered commercial HP used in composite making are shown. Non sintered HP powder, with 3.3 µm average particle size, indicated by annexe D, Figure D.1, has a diffractogram with broad peaks that may indicate submicron crystallite presence in the sample [73]. All powder peaks were identified as hexagonal calcium phosphate hydroxide by ICDD 00-034-0010, indicating the presence of pure hydroxyapatite. Despite what can be found in the literature about HP not decomposing at 1350 °C, given the Ca/P ratio is similar to the

stoichiometric value [74], results have shown some decomposition has indeed happen at 1350 °C on this HP commercial powder. Resulting in peaks that suggest the presence of α-TCP and β-TCP by ICDD 98-007-6561 and ICDD 01-070-2065 respectively.

The presence of HP has a clear effect on BCT samples as the X-ray diffractogram on Figure 4.3.2 show. Even the slight 10% weight presence is enough to react, to some extent, with calcium doped barium titanate forming different phases like barium phosphor hydroxide identified by ICDD 00-024-00028. Regardless the new phase formation, XRD still shows a dominant presence of tetragonal BCT by ICDD 01-082-2234 and HP from the record mentioned before. It is important to notice the peaks identified as BCT are slightly shifted to higher angles in comparison with the peaks that appear in BCT10 diffractogram on the same figure. This is most likely due to the increase presence of calcium prevenient from HP. As mentioned in section 4.2.2, Ca^{2+} has a smaller ionic radius than Ba^{2+} and by replacing it in BCT lattice, the unit cell volume decreases provoking the shift. The remaining Ba^{2+} may react with HP, now low on Ca^{2+}, to form hexagonal barium phosphate hydroxide identified by ICCD 00-024-0028.

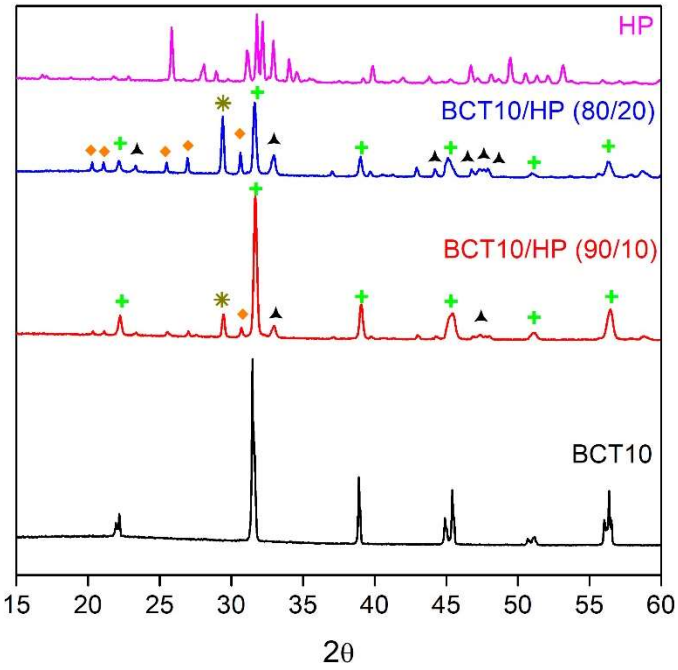

Figure 4.3.2 X-ray diffraction comparison between BCT10 samples containing 10 wt% and 20 wt% hydroxyapatite, BCT10 sample and HP sample all sintered at 1350 °C. ▲ Hydroxyapatite, ◆ barium phosphate, ✚ calcium doped barium titanate and ✳ α-TCP.

If the presence of HP is concern for angle shifting to higher values, the same cannot be said regarding the increase of HP percentage in the same material. Analysing BCT10/HP (80/20) diffractogram is possible to understand there is no remarkable shift of the peaks already visible on BCT10/HP (90/10) diffractogram. However, peaks indicating the presence of HP and barium phosphate hydroxide gain considerable intensity indicating stronger presence of these phases. In both BCT10/HP (90/10) and BCT10/HP (80/20) diffractograms there seems to be evidence of HP decomposition into α-TCP as it happens in pure HP when sintered at 1350 °C. Suggesting that calcium doped barium titanate reacts with hydroxyapatite, as some works support [75]. Information in the literature states the different phases, here reported to be part of the composites produced, like barium phosphate, are non-cytotoxic [76], [77].

The rest of the composites containing BT, BCT05 and BCT15 diffractograms are in annexe E.1 and all follow the same comparative logic between the mixture starting material, both 10% and 20% HP content and finally, sintered HP. BT and BCT05 X-ray diffraction analysis respectively, show the same line of evolution between diffractograms as BCT10 does, this can be seen in annexe E.1, Figure E.4 and Figure E.5. In the sense that is notorious a peak shift to higher angle values between the free HP mixture and the composites. Also, comparing the composites between themselves, although there is no transformation regarding peak position, there is regarding peak intensity increase when HP content increases as well. Samples based on BCT15 are presented on Figure E.6. An interesting transformation of the double peak discussed in section 4.2.2 near $2\theta = 38°$ happens due to its complete disappearance when HP is added. On both composites BCT15 based containing 10% and 20% HP the peaks shown in the diffractograms are very similar to the ones seen on rest of the samples. Which leads to the belief that HP addition restored the crystal order in BCT15 lattice to one like the ones shown by the remaining mixtures.

4.3.2. SEM and EDS

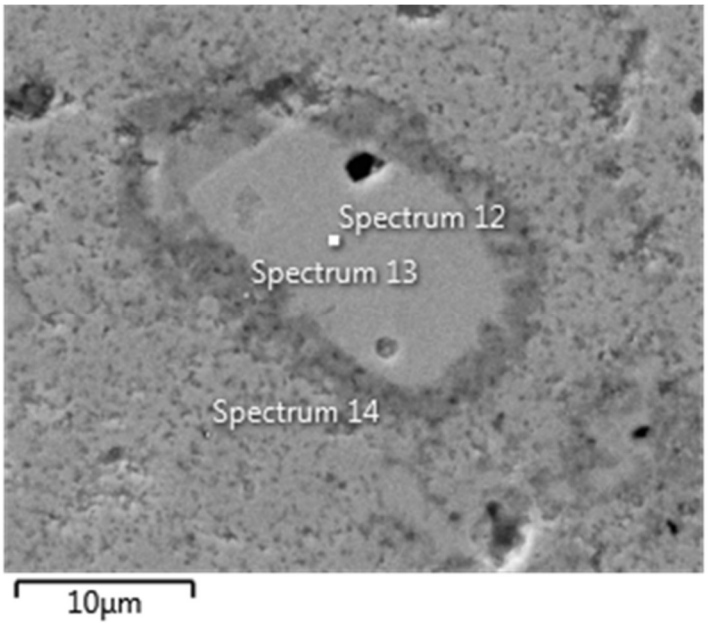

Figure 4.3.3 BCT10/HP (90/10) composite under SEM microscopy and EDS quantification on three different points of the sample.

Multi-phase formations like the one in Figure 4.3.3 often come across when analysing, using SEM microscopy, the polished surface of composite samples such as BCT10/HP (90/10). By EDS analysis is possible to quantify the points indicated, one being in the centre of the formation (spectrum 12), another on the border (spectrum 13) and one outside (spectrum 14). In the EDS spectrum 12, a large presence of phosphor and barium with low amount of calcium as can be seen in annexe I, Figure I.4. As the spectrums advance outside the formation to spectrum 13, calcium presence increases becoming the most abundant, titanium is revealed and phosphor decreases. Outside the formation borders, spectrum 14 indicates the presence of barium, titanium, the lowest calcium presence and phosphor in the same amount as in spectrum 13. Overlapping the composite XRD analysis information in section 4.3.1, Figure 4.3.1, with the EDS spectrums mentioned here, barium phosphate phase is present in the formation interior analysed by spectrum 12. The border by spectrum 13 suggests α-TCP, hydroxyapatite and calcium doped barium titanate are mixed but did not react to big extent. On the outside by spectrum 14, BCT reacted to some extend with HP dissociating phosphor but to small extent compared with the interior by spectrum 12. The last remark is also supported by XRD results,

in the previously mentioned section, since the addition of 10% HP is cause for 2θ shifting to higher angles.

The same SEM and EDS analysis is reported for BT/HP (90/10) composite in annexe I, Figure I.3. The results are in every way similar to BCT10/HP (90/10). However, since all the calcium in BT/HP (90/10) must be from hydroxyapatite and every spectrum reveal calcium presence, under synthesis conditions it is clear BT or BCT always react to some extent with hydroxyapatite even if it is as small as spectrum 11 indicates (see annexe I).

4.4. ICP-AES and SEM/EDS accounting for bioactivity essays

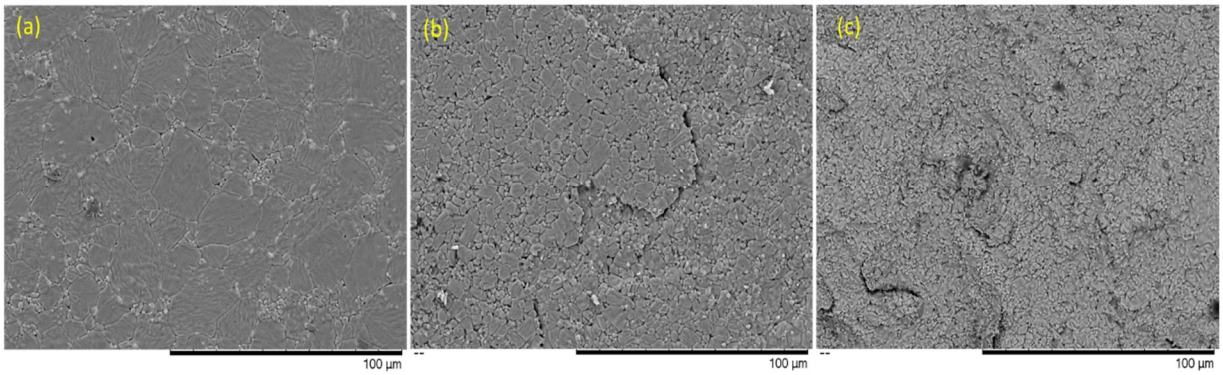

Figure 4.4.1 SEM microscopy showing BCT05 surface: (a) unpolarized after sintering, (b) unpolarized after immersed in SBF for 7 days (c) polarized after 7 day immersion in SBF.

Bioactivity was tested by analysing the surface of materials to detect the deposition of calcium and phosphor ions on its surface. Given the fact that only a small number of samples were polarized and results from corona polling are difficult to reproduce, the same sample was immersed in a large volume of SBF (simulated body fluid). From that volume, small samples were taken out and measured, by ICP-AES, for calcium and phosphor concentration accounting with volume variation. The decrease in concentration of calcium and phosphor in the SBF solution indicates there had been precipitation onto the sample surface. On the other hand, if the concentration of either calcium or phosphor increases, it means there is dissolution of the deposit or the sample itself.

Figure 4.4.2 shows the evolution of calcium and phosphor concentrations in SBF, during 7 days in contact with $Ba_{(1-x)}Ca_xTiO_3$ $0 \leq x \leq 0.15$ polarized samples. Although there is a clear mix of precipitation and dissolution phenomena along the experiment, it is also possible to acknowledge a precipitation tendency. However, it is very hard to quantify the results since there is some error associated with measurements and precipitation/dissolution cycle is not regular along time nor mixture.

In Figure 4.4.1 it is shown BCT05 polarized surface transformation for 7 days immersion under both polarized (c) and unpolarized (b) circumstances. Via SEM/EDS mapping and elemental quantification is possible to notice a strong presence of phosphor, that can only come from SBF solution, and some calcium residue as shown in annexe L, Figure L.1 and Figure L.2. From all mixtures, BCT05 is the one that manifests more surface deposition and it is also the sample with the highest Q_p value as can be confirmed in section 4.2.8, Table 4.3. The remaining BCT samples, have smaller Q_p values than BCT05, but similar between themselves. Through EDS analysis, the presence of calcium and phosphor in the samples mentioned before appears in more scarce quantities, as can be seen in annexe L, Figure L.6 to Figure L.8. This means there seems to be a relation between increasing charge polarization and increasing surface deposition.

The same mixtures unpolarized samples revealed both precipitation and dissolution general tendencies, despite most samples had preferable precipitation. BT and BCT05 phosphor concentration have a dissolution tendency by rising concentration along the 7 days period as can be seen in annexe L, Figure L.3. Composites BCT/HP (90/10) showed less ability to precipitate the apatite layer in either polarized or unpolarized state comparing with BCT mixtures as can be seen in annexe L, Figure L.4 and Figure L.5. The ICP-AES results are somewhat inconclusive specially regarding composites and require further studies with more samples in order to achieve statistical meaning and confirmation. Despite this, information backed by SEM/EDS analysis allows the acknowledgment of an apatite layer formation on BCT polarize samples.

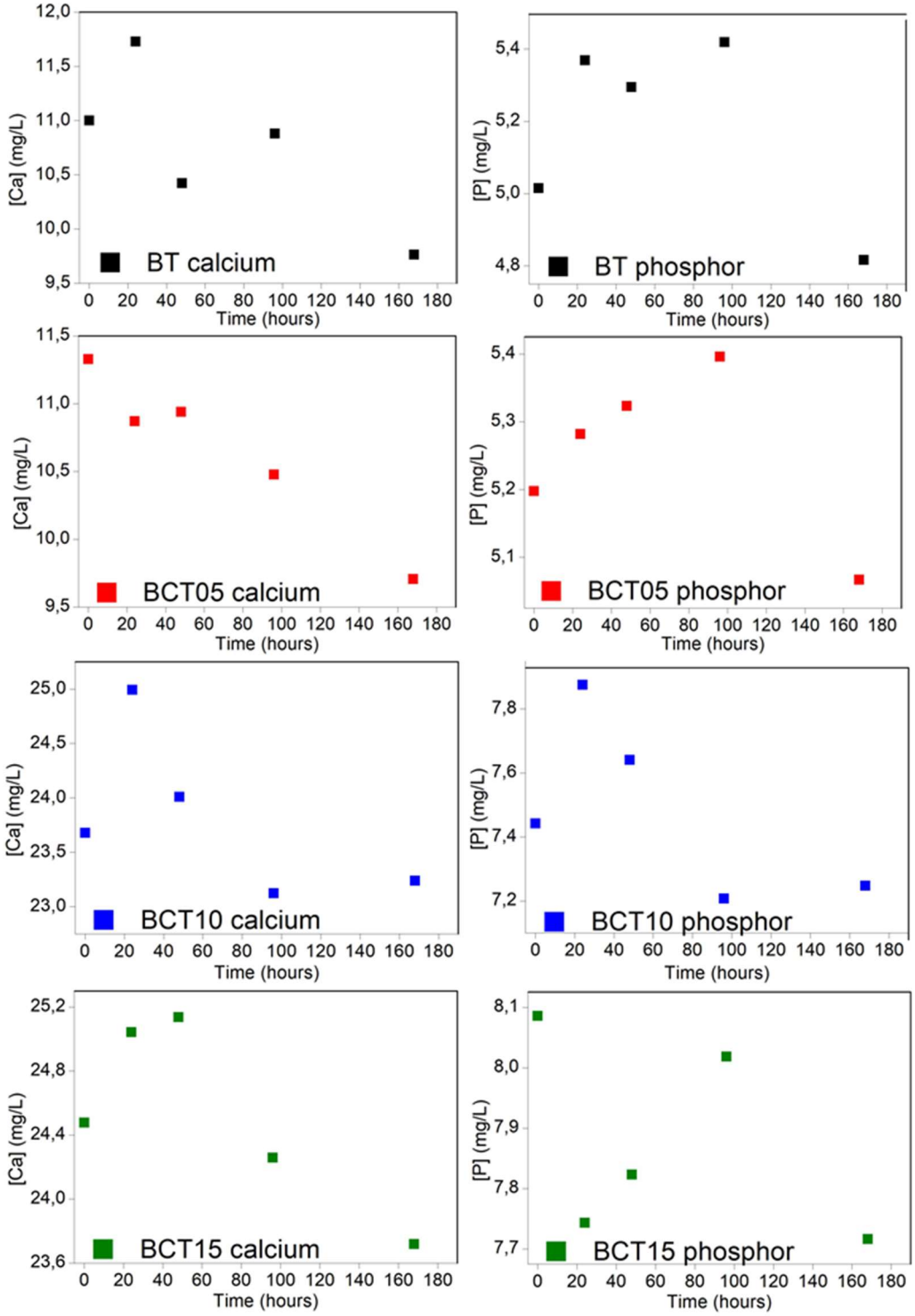

Figure 4.4.2 ICP-AES results for both calcium and phosphor concentration in SBF samples, collected during 7 days, out of a recipient containing one polarized $Ba_{(1-x)}Ca_xTiO_3$ $0 \leq x \leq 0.15$ ceramic sample and 250 mL SBF.

5. Conclusions

Between the three uncontaminated analytical reagents, $CaCO_3$ revealed to have the highest mass loss percentage and the lowest temperature starting point at which thermal decomposition takes place, suggesting that its presence will influence since an early stage the reaction of BCT samples formation. Following the previous, $BaCO_3$ has lower mass loss percentage and higher temperature starting point during thermal decomposition. TiO_2 did not show any mass loss during heating. Both carbonates had higher average particle size than TiO_2.

Tetragonal phase, in $Ba_{(1-x)}Ca_xTiO_3$ $0 \leq x \leq 0.3$ mixtures, was achievable by 1350 °C sintering temperature, despite BCT30 also presenting $CaTiO_3$ cubic phase. Unit cell volume decreases as calcium gives way into BT lattice due to crystal plane approximation since calcium ions Ca^{2+} are smaller than barium ions Ba^{2+}. During sintering, N_2 reductive atmosphere did not improve the formation of tetragonal phase regardless of sintering temperature. Under materials synthesis conditions, the large majority of calcium substitution is done in A-site of ABO_3 perovskite structure, as RAMAN results suggest. Despite this, FTIR results indicate there is always some residual substitution on B-site proven by frequency decrease between BT and BCT05 spectrums, consequence of weaker coulomb interaction with O^{2-} ions. Although tetragonal phase is present in all mixtures, phase distortion happens along calcium substitution. From $Ba_{(1-x)}Ca_xTiO_3$ $x \geq 0.2$, crystal conformation is affected to the extent of accentuated Curie point decrease, thus establishing $x \leq 0.15$ as substitution limit in order to ensure and maintain tetragonal phase properties.

Average particle size of 3.6 – 5.0 μm after milling is enough to obtain tetragonal phase after sintering but an heterogenous mix of small and mainly large grain sizes is formed. Smaller particle size and calcium presence both inhibit grain growth, in some cases, these two overlap like in BCT15 where calcium presence is obfuscated by the larger particle size that dictates larger grain formation. For the remaining mixtures grain growth is controlled by calcium presence.

Hydroxyapatite decomposes in both α-TCP and β-TCP when sintered at 1350 °C. When mixed with BCT and sintered, HP reacts to some extent forming barium phosphor and α-TCP, but also maintains some of BCT and HP structure. By minimizing HP content to 10% weight, a smaller fraction of BPH and α-TCP phases are formed, in comparison with 20% weight HP presence. It is possible to identify on samples surface small oval shaped formations where these reactions take place.

All materials are non-cytotoxic. Early stage bioactivity essays revealed low temperature polarized BCT mixtures have an enhanced ability to deposit Ca^{2+} and PO^{3-}_4 ions on its surface in comparison to unpolarized ones. In particular BCT05, by holding the highest charge polarization (Q_p), also presented the biggest surface transformation while immersed in SBF, giving way to the most well-formed apatite layer between all samples. This result indicates there is a direct relation between well polled BCT samples and apatite layer affinity. Composites made of BCT/HP (90/10) on the other hand, did not show a significant difference, regarding apatite layer deposition, between polarized and unpolarized samples. Since composite samples were not submitted to TSDC, there is no information to the polarization extent of these samples. But it is likely that 110 °C polarization temperature was too low, knowing HP surface charge is commonly generated by high temperature electric field application. For HP polarization, high temperature between 200 °C and 300 °C is necessary to provide the activation energy for the reorientation of protons around O^{2-} causing the ordering of lattice OH^- ions, in other words, the formation of oxygen vacancies [78]. Composites, compared to BCT mixtures, showed to have both dissolution and precipitation behaviour of calcium and phosphor ions by ICP-AES analysis.

This can be related to the presence of α-TCP in composite , since this phase has rapid dissolution and thus releases Ca^{2+} and PO^{3-}_4, increasing their concentration in SBF medium [79].

5.1. Future perspectives

Although many results are reported here, there is still much work to be done regarding the subject discussed. It would be very interesting to increase milling time in order to obtain submicron particle size and to reduce grain size for both BCT and BCT/HP, then analyse via TSDC the piezoelectric response and the evolution of activation energy and relaxation times. Polarization temperature study must be done in order to determine the influence it might have on BCT samples since there is literature supporting that immediately above Curie point the polarizability of BT crystal is very high [80]. Also, regarding the high polarization temperatures required for hydroxyapatite may be favourable to this study. It would also be important to polarize samples while controlling current flow instead of only controlling potential voltage which is believed to be one of the reasons why mixtures present different polarization charges.

Some undesirable phase formation in BCT, could be suppressed by CO_2 atmosphere during sintering [17]. Also, higher sintering temperatures and shorter sintering times might be a good way to prevent grain growth and possible optimization regarding piezoelectric properties. A two-step sintering method, followed by chemical binder addition could have inhibit the fraction of phases, like BPH and α-TCP, by sintering BCT at higher temperature (above 1350 °C) and HP at lower temperature (bellow 1300 °C).

Since some reaction between BCT and HP happens when sintering at 1350 °C, it would be interesting to study carbon vibration modes of the newly formed phases via FTIR analysis. DSC analysis to composites samples is also important to better understand the evolution of Curie point in function of hydroxyapatite presence. It would also be important to compare BCT Raman results with composites sample, in order to understand the lattice distortion and tetragonal phase compromise HP may cause. Thermal etching before SEM/EDS analysis could have been done in order to better quantify grain size and distribution.

Results given by ICP-AES must have more statistical significance in order to quantify the materials ability to deposit calcium and phosphor ions on its surface. It is also recommended to do longer SBF immersion periods in order to quantify a possible apatite layer growth. Since these materials are piezoelectric, it would be very interesting to make SBF immersion tests at the same time as the samples are mechanically stimulated in order to generate an electrical response and analyse the precipitation/dissolution dynamics change in SBF.

References

[1] O. Sumant and S. Shinde, “Orthopedic Implants Market by Product Type (Reconstructive Joint Replacements, Spinal Implants, Dental Implants, Trauma, Orthobiologics, and Others), Biomaterial (Metallic, Ceramic, Polymeric, and Others), and Type (Knee, Hip, Wrist & Shoulder, Dental, Sp,” 2019. [Online]. Available: https://www.alliedmarketresearch.com/orthopedic-implants-market.

[2] M. M. Stevens, “Biomaterials for bone tissue engineering,” *Biomech. Biomater. Orthop. Second Ed.*, vol. 11, no. 5, pp. 18–25, 2008.

[3] R. Attström and U. van der Velden, “Consensus report (epi-demiology),” in *Proceedings ofthe 1st European Workshop on Periodontics*, 1993, pp. 120–126.

[4] M. Esposito, J. Hirsch, U. Lekholm, and P. Thomsen, “Differential Diagnosis and Treatment Strategies for Biologic Complications and Failing Oral Implants: A Review of the Literature,” *Int. J. Oral Maxillofac. Implants*, vol. 14, no. 4, pp. 473–490, 1999.

[5] A. H. Rajabi, M. Jaffe, and T. L. Arinzeh, “Piezoelectric materials for tissue regeneration: A review,” *Acta Biomater.*, vol. 24, pp. 12–23, 2015.

[6] J. Curie and P. Curie, “Développement, par pression, de l’électricité polaire dans les cristaux hémièdres à faces inclinées,” *Comptes Rendues*, vol. 91, pp. 90–93, 1880.

[7] J. P. Ball, B. A. Mound, J. C. Nino, and J. B. Allen, “Biocompatible evaluation of barium titanate foamed ceramic structures for orthopedic applications,” *J. Biomed. Mater. Res. - Part A*, vol. 102, no. 7, pp. 2089–2095, 2014.

[8] F. R. Baxter, C. R. Bowen, I. G. Turner, and A. C. E. Dent, “Electrically active bioceramics: A review of interfacial responses,” *Ann. Biomed. Eng.*, vol. 38, no. 6, pp. 2079–2092, 2010.

[9] B. Jaffe, R. C. William, and H. Jaffe, *Piezoelectri Ceramics*, 1st ed. London, New York: Academic Press INC., 1971.

[10] M. M. Vijatović, J. D. Bobić, and B. D. Stojanović, “History and challenges of barium titanate: Part I,” *Sci. Sinter.*, vol. 40, no. 2, pp. 155–165, 2008.

[11] J. M. Herbert, *Ceramic Dielectrics and Capacitors*. New York: Gordon and Breach Science Publishers, 1985.

[12] W. S. Cho, “Structural evolution and characterization of $BaTiO_3$ nanoparticles synthesized from polymeric precursor,” *J. Phys. Chem. Solids*, vol. 59, no. 5, pp. 659–666, 1998.

[13] W. L. Cherry and R. Adler, “Piezoelectric effect in polycrystalline barium titanate,” *Phys. Rev.*, vol. 72, no. 10, pp. 981–982, 1947.

[14] D. Berlincourt, “Recent Developments in Ferroelectric Transducer Materials,” vol. 1055, no. 00, pp. 53–65, 1956.

[15] S. Roberts, “Dielectric and Piezoelectric Properties of Barium Titanate,” vol. 71, Cambridge, Massachusetts: American Physical Society, 1946, pp. 890–895.

[16] S. Shao, “High piezoelectric properties and domain configuration in $BaTiO_3$ ceramics obtained through the solid-state reaction route,” 2008.

[17] L. K. Templeton and J. A. Pask, “Formation of $BaTiO_3$ from $BaCO_3$ and TiO_2 in Air and in CO_2,” vol. 33, no. 1952, pp. 212–216, 1954.

[18] L. Wang, L. Liu, D. Xue, H. Kang, and C. Liu, “Wet routes of high purity $BaTiO_3$ nanopowders,” *J. Alloys Compd.*, vol. 440, no. 1–2, pp. 78–83, 2007.

[19] E. Fukada and I. Yasuda, “On the piezoelectric effect of bone,” *Journal of the Physical Society of Japan*, vol. 12, no. 10. pp. 1158–1162, 1957.

[20] J. Park and R. Lakes, *Biomaterials: an introduction*, 2nd ed. New York: Plenum Press, 1992.

[21] T. Hassenkam, G. E. Fantner, J. A. Cutroni, J. C. Weaver, D. E. Morse, and P. K. Hansma, “High-resolution AFM imaging of intact and fractured trabecular bone,” *Bone*, vol. 35, no. 1, pp. 4–10, 2004.

[22] K. Ramachandran, G. N. Gopinath, “Structure of Collagen,” *Nature*, vol. 176, pp. 593–595, 1955.

[23] M. Feughelman, D. Lyman, E. Menefee, and B. Willis, “The orientation of the α-helices in α-keratin fibres,” *Int. J. Biol. Macromol.*, vol. 33, no. 1–3, pp. 149–152, 2003.

[24] Y. Zhang, L. Chen, J. Zeng, K. Zhou, and D. Zhang, “Aligned porous barium titanate/hydroxyapatite composites with high piezoelectric coefficients for bone tissue engineering,” *Mater. Sci. Eng. C*, vol. 39, no. 1, pp. 143–149, 2014.

[25] C. Ribeiro *et al.*, “Power management architecture for smart hip prostheses comprising multiple energy harvesting systems,” *Sensors Actuators A. Phys.*, vol. 202, pp. 183–192, 2015.

[26] A. Bagchi, S. R. K. Meka, B. N. Rao, and K. Chatterjee, “Perovskite ceramic nanoparticles in polymer composites for augmenting bone tissue regeneration,” *Nanotechnology*, vol. 25, no. 48, 2014.

[27] Y. H. O. Han, J. B. Appleby, and D. M. Smyth, “Calcium as an Acceptor Impurity in $BaTi0_3$” vol. 100, no. 32, pp. 96–100, 1987.

[28] Z. Q. Zhuang, M. P. Harmer, D. M. Smyth, and R. E. Newnham, “The effect of octahedrally-coordinated calcium on the ferroelectric transition of $BaTiO_3$” *Mater. Res. Bull.*, vol. 22, no. 10, pp. 1329–1335, 1987.

[29] D. F. K. Hennings and H. Schreinemacher, “Ca-acceptors in dielectric ceramics sintered in reducive atmospheres,” *J. Eur. Ceram. Soc.*, vol. 15, no. 8, pp. 795–800, 1995.

[30] X. Wang, H. Yamada, and Chao-Nan Xu, “Large electrostriction near the solubility limit in $BaTiO_3$–$CaTiO_3$ ceramics” vol. 022905, no. January 2005, pp. 12–15, 2005.

[31] X. N. Zhu, W. Zhang, and X. M. Chen, “Enhanced dielectric and ferroelectric characteristics in Ca-modified $BaTiO_3$ ceramics” *AIP Adv.*, vol. 3, no. 8, p. 082125, 2013.

[32] J. M. Vaugghan, *The Physiology of Bone*. Clarendon, Oxford, 1970.

[33] A. Gruverman, D. Wu, B. J. Rodriguez, S. V. Kalinin, and S. Habelitz, “High-resolution imaging of proteins in human teeth by scanning probe microscopy,” *Biochem. Biophys. Res. Commun.*, vol. 352, no. 1, pp. 142–146, 2007.

[34] S. B. Lang *et al.*, “Pyroelectric, piezoelectric and photoeffects in hydroxyapatite thin films on silicon,” *Proc. - Int. Symp. Electrets*, no. March, pp. 87–88, 2011.

[35] S. B. Lang *et al.*, “Ferroelectric polarization in nanocrystalline hydroxyapatite thin films on silicon,” *Sci. Rep.*, vol. 3, pp. 1–6, 2013.

[36] T. Kobayashi, S. Nakamura, and K. Yamashita, “Enhanced osteobonding by negative surface charges of electrically polarized hydroxyapatite,” *J. Biomed. Mater. Res.*, vol. 57, no. 4, pp. 477–484, 2001.

[37] T. P. Hoepfner and E. D. Case, “The porosity dependence of the dielectric constant for sintered hydroxyapatite,” *J. Biomed. Mater. Res.*, vol. 60, no. 4, pp. 643–650, 2002.

[38] J. R. Jones, L. M. Ehrenfried, and L. L. Hench, “Optimising bioactive glass scaffolds for bone tissue engineering,” *Biomaterials*, vol. 27, no. 7, pp. 964–973, 2006.

[39] C. R. Bowen, J. Gittings, I. G. Turner, F. Baxter, and J. B. Chaudhuri, “Dielectric and piezoelectric properties of hydroxyapatite-$BaTiO_3$ composites,” *Appl. Phys. Lett.*, vol. 89, no. 13, pp. 1–4, 2006.

[40] Y. Yang *et al.*, “Structure, electrical and dielectric properties of Ca substituted $BaTiO_3$ ceramics,” *Ceram. Int.*, vol. 44, no. 10, pp. 11109–11115, 2018.

[41] M. R. Panigrahi and S. Panigrahi, “Synthesis and microstructure of Ca-doped $BaTiO_3$ ceramics prepared by high-energy ball-milling,” *Phys. B Condens. Matter*, vol. 404, no. 21, pp. 4267–4272, 2009.

[42] V. S. Puli, D. K. Pradhan, B. C. Riggs, D. B. Chrisey, and R. S. Katiyar, “Investigations on structure, ferroelectric, piezoelectric and energy storage properties of barium calcium titanate (BCT) ceramics,” *J. Alloys Compd.*, vol. 584, pp. 369–373, 2014.

[43] S. Shao *et al.*, “Erratum: High piezoelectric properties and domain configuration in $BaTiO_3$ ceramics obtained through solid-state reaction route (Journal of Physics D: Applied Physics (2008) 41 (125408)),” *J. Phys. D. Appl. Phys.*, vol. 42, no. 18, 2009.

[44] M. A. Tomoaki KARAKI , Kang YAN, “Barium Titanate Piezoelectric Ceramics Manufactured by Two-Step Sintering Barium Titanate Piezoelectric Ceramics Manufactured by Two-Step Sintering,” *Jpn. J. Appl. Phys.*, vol. 7035, 2007.

[45] L. Simon-Seveyrat, A. Hajjaji, Y. Emziane, B. Guiffard, and D. Guyomar, “Re-investigation of synthesis of $BaTiO_3$ by conventional solid-state reaction and oxalate coprecipitation route for piezoelectric applications,” *Ceram. Int.*, vol. 33, no. 1, pp. 35–40, 2007.

[46] W. Huebner and H. U. Anderson, “Tspc/Dc Measurements on Barium Titanate.,” pp. 353–356, 1986.

[47] J. B. Park, S. D. Brown, and J. K. Scott, “Mechanical property changes of barium titanate (ceramic) after in vivo and in vitro aging,” in *Biomaterials, Medical Devices, and Artificial Organs*, vol. 5, no. 3, 1977, pp. 267–276.

[48] C. Ergun, H. Liu, J. W. Halloran, and T. J. Webster, “Increased osteoblast adhesion on nanograined hydroxyapatite and tricalcium phosphate containing calcium titanate,” *J. Biomed. Mater. Res.*, pp. 990–997, 2006.

[49] L. Le Guéhennec, A. Soueidan, P. Layrolle, and Y. Amouriq, “Surface treatments of titanium dental implants for rapid osseointegration,” *Dent. Mater.*, vol. 23, no. 7, pp. 844–854, 2007.

[50] T. Albrektsson, P.-I. Brånemark, H.-A. Hansson, and J. Lindström, “Osseointegrated titanium implants: Requirements for ensuring a long-lasting, direct bone-to-implant anchorage in man,” *Class. Pap. Orthop.*, vol. 52, pp. 155–170, 1981.

[51] I. Arvanitidis, D. Sichen, and S. Seetharaman, “A study of the thermal decomposition of $BaCO_3$,” *Metall. Mater. Trans. B Process Metall. Mater. Process. Sci.*, vol. 27, no. 3, pp. 409–416, 1996.

[52] W. F. Sullivan and S. S. Cole, “Thermal Chemistry of Colloidal Titanium Dioxide,” *Journal of the american Ceram. Soc.*, no. 41, 1959.

[53] E. S. P. B. V, R. M. Mcintosh, J. H. Sharp, and F. W. Wilburn, “The thermal decomposition of

dolomite," *Thermochim. Acta*, vol. 165, pp. 281–296, 1990.

[54] B. Stuart, *Infrared Spectroscopy: Fundamentals and Applications*. John Wiley & Sons, Ltd, 2004.

[55] G. Silvio *et al.*, "Preparation and characterization of core-shell structured TiO_2–$BaCO_3$ particles," *Solid State Sci.*, vol. 3, pp. 291–299, 2001.

[56] R. H. Perry and D. Green, *Perry's Chemical Engineer's Handbook*. Tokyo: McGraw Hill, 1984.

[57] C. Gomez-Yañez, C. Benitez, and H. Balmori-Ramirez, "Mechanical activation of the synthesis reaction of $BaTiO_3$ from a mixture of $BaCO_3$ and TiO_2 powders," *Ceram. Int.*, vol. 26, no. 3, pp. 271–277, 2000.

[58] T. Kimura and N. Koga, "Monohydrocalcite in comparison with hydrated amorphous calcium carbonate: Precipitation condition and thermal behavior," *Cryst. Growth Des.*, vol. 11, no. 9, pp. 3877–3884, 2011.

[59] S. Ye, J. Fuh, and L. Lu, "Effects of Ca substitution on structure, piezoelectric properties, and relaxor behavior of lead-free Ba(Ti 0.9Zr 0.1)O_3 piezoelectric ceramics," *J. Alloys Compd.*, vol. 541, pp. 396–402, 2012.

[60] C. H. Perry, B. N. Khanna, and G. Rupprecht, "Infrared Studies of Perovskite Titanates," *Phys. Rev. Journals*, vol. 135, 1964.

[61] X. Jin, D. Sun, M. Zhang, Y. Zhu, and J. Qian, "Investigation on FTIR spectra of barium calcium titanate ceramics," *J. Electroceramics*, vol. 22, no. 1–3, pp. 285–290, 2009.

[62] U. D. Venkateswaran, V. M. Naik, and R. Naik, "High-pressure Raman studies of polycrystalline BaTiO," *Phys. Rev. B*, vol. 58, no. 21, pp. 14256–14260, 1998.

[63] I. B. Ouni, D. Chapron, H. Aroui, and M. D. Fontana, "Ca doping in $BaTiO_3$ crystal: Effect on the Raman spectra and vibrational modes," *J. Appl. Phys.*, vol. 121, no. 11, pp. 1–7, 2017.

[64] M. C. Chang and S. C. Yu, "Raman study for (Ba1-xCax)TiO3 and Ba($Ti_{1-y}Ca_y$)O_3 crystalline ceramics," *J. Mater. Sci. Lett.*, vol. 19, no. 15, pp. 1323–1325, 2000.

[65] J. Pokorńy, U. M. Pasha, L. Ben, O. P. Thakur, D. C. Sinclair, and I. M. Reaney, "Use of Raman spectroscopy to determine the site occupancy of dopants in BaTiO3," *J. Appl. Phys.*, vol. 109, no. 11, 2011.

[66] M. Acosta *et al.*, "BaTiO3 - based piezoelectrics: Fundamentals, current status, and perspectives," *Appl. Phys. Rev.*, vol. 4, no. 4, 2017.

[67] S. H. Yoon, S. H. Kang, S. H. Kwon, and K. H. Hur, "Resistance degradation behavior of Ca-doped $BaTiO_3$," *J. Mater. Res.*, vol. 25, no. 11, pp. 2135–2145, 2010.

[68] Q. Zhao, H. Gong, X. Wang, I. W. Chen, and L. Li, "Superior Reliability Via Two-Step Sintering: Barium Titanate Ceramics," *J. Am. Ceram. Soc.*, vol. 99, no. 1, pp. 191–197, 2016.

[69] N. Ahmadi, M. Kharaziha, and S. Labbaf, "(Ba–Ca)TiO_3 nanopowder: Synthesis and their electrical and biological characteristics," *Mater. Chem. Phys.*, vol. 226, no. January 2018, pp. 263–271, 2019.

[70] D. Waller, T. Iqbal, and A. Safari, "Poling of Lead Zirconate Titanate Ceramics and Flexible Piezoelectric Composites by the Corona Discharge Technique," *J. Am. Ceram. Soc.*, vol. 72, no. 2, pp. 322–324, 1989.

[71] S. H. Yoon, C. A. Randall, and K. H. Hur, "Effect of Acceptor (Mg) concentration on the resistance degradation behavior in acceptor (Mg)-doped $BaTiO_3$ bulk ceramics: II. Thermally stimulated

depolarization current analysis," *J. Am. Ceram. Soc.*, vol. 92, no. 8, pp. 1766–1772, 2009.

[72] W. Wu, Z. Liu, Y. Gu, Z. Yue, and Y. Li, "Thermally stimulated depolarization current study on barium titanate single crystals," *AIP Adv.*, vol. 8, no. 4, pp. 0–6, 2018.

[73] H. S. Liu *et al.*, "Hydroxyapatite synthesized by a simplified hydrothermal method," *Ceram. Int.*, vol. 23, no. 1, pp. 19–25, 1997.

[74] G. Muralithran and S. Ramesh, "The Effects of sintering temperature on the properties of hydroxyapatite," *Ceram. Int.*, vol. 26, no. 2, pp. 221–230, 2000.

[75] A. Aba and C. Ergun, "Phase stability in hydroxyapatite/barium titanate piezo bioceramics," *Defect Diffus. Forum*, vol. 273–276, pp. 1–7, 2008.

[76] F. R. Baxter, I. G. Turner, C. R. Bowen, J. P. Gittings, and J. B. Chaudhuri, "An in vitro study of electrically active hydroxyapatite-barium titanate ceramics using Saos-2 cells," *J. Mater. Sci. Mater. Med.*, vol. 20, no. 8, pp. 1697–1708, 2009.

[77] B. Zhu *et al.*, "Synthesis of nanostructured barium phosphate and its application in micro-computed tomography of mouse brain vessels in ex vivo," *J. Nanoparticle Res.*, vol. 16, no. 2, 2014.

[78] K. Yamashita and N. Oikawa, "Acceleration and Deceleration of Bone-Like Crystal Growth on Ceramic Hydroxyapatite by Electric Poling," vol. 4756, no. 12, pp. 2697–2700, 1996.

[79] H. Yuan *et al.*, "Bone formation induced by calcium phosphate ceramics in soft tissue of dogs: A comparative study between porous α-TCP and β-TCP," *J. Mater. Sci. Mater. Med.*, vol. 12, no. 1, pp. 7–13, 2001.

[80] A. G. Chynoweth, "Surface Space-Charge Layers in Barium Titanate," *Phys. Rev.*, vol. 102, pp. 705–714, 1955.

Annexes

A. Introduction

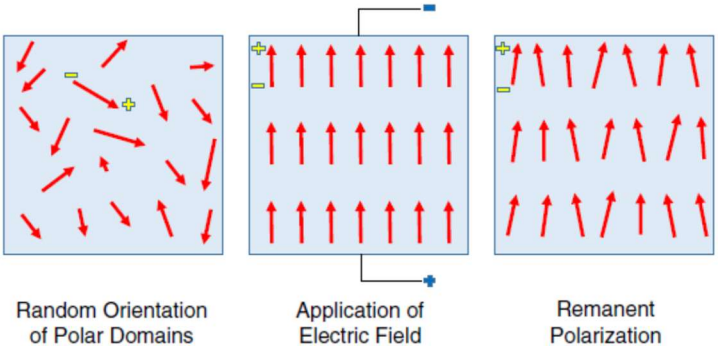

Figure A.1 Electric field application effect on the spontaneous oriented domains formed from cooling in piezoelectric materials [77].

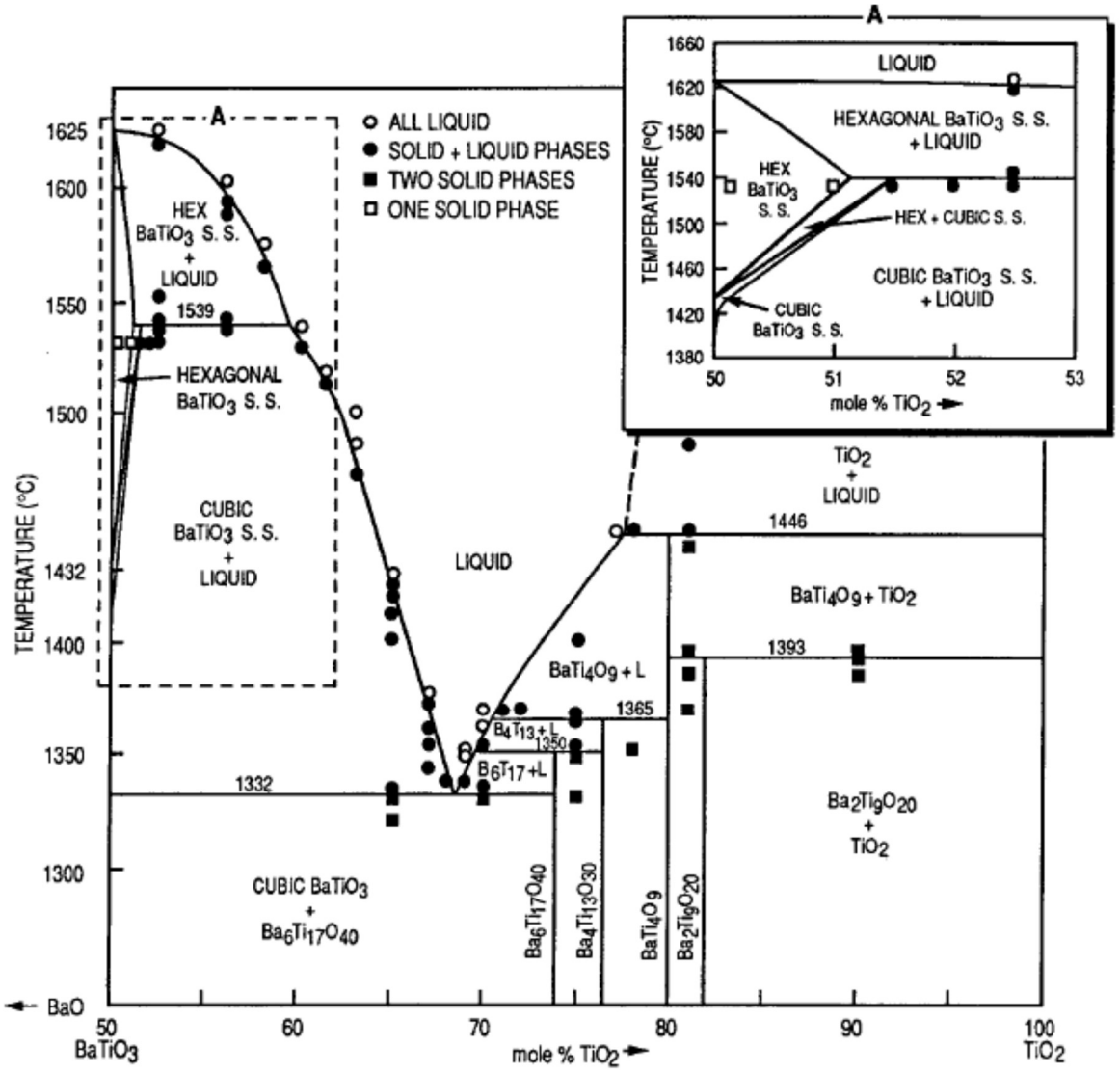

Figure A.2 $BaTiO_3$-TiO_2 equilibrium phase diagram [45]

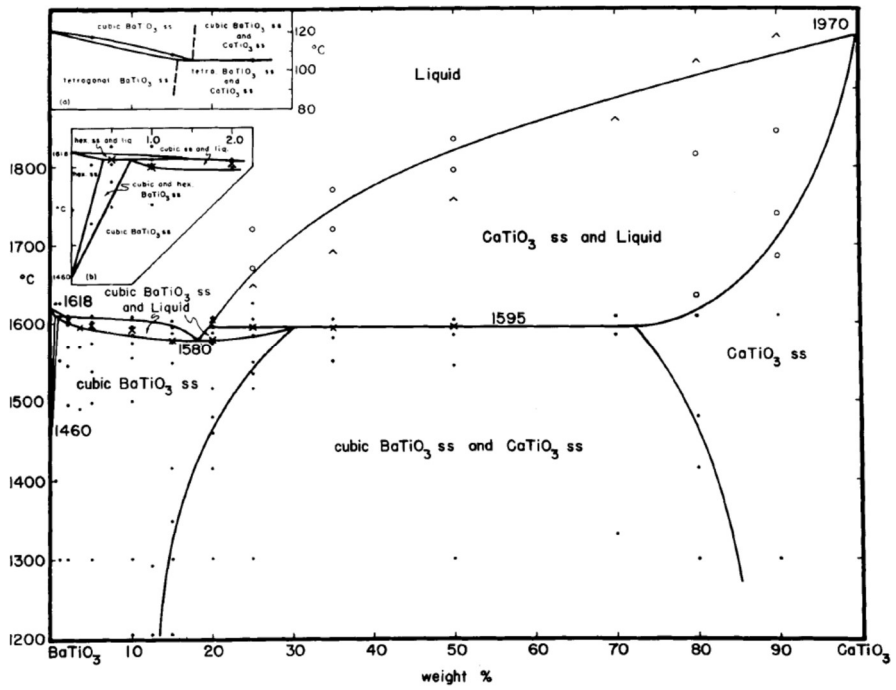

Figure A.3 Phase diagram of $BaTiO_3$ and CaTiO3 [46]

B. Sample production method

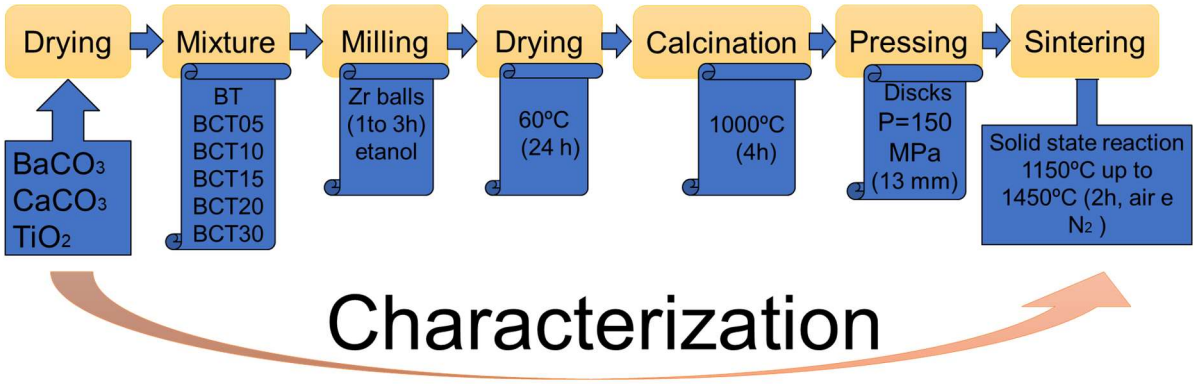

Figure B.1 Schematic of BT and BCT sample production

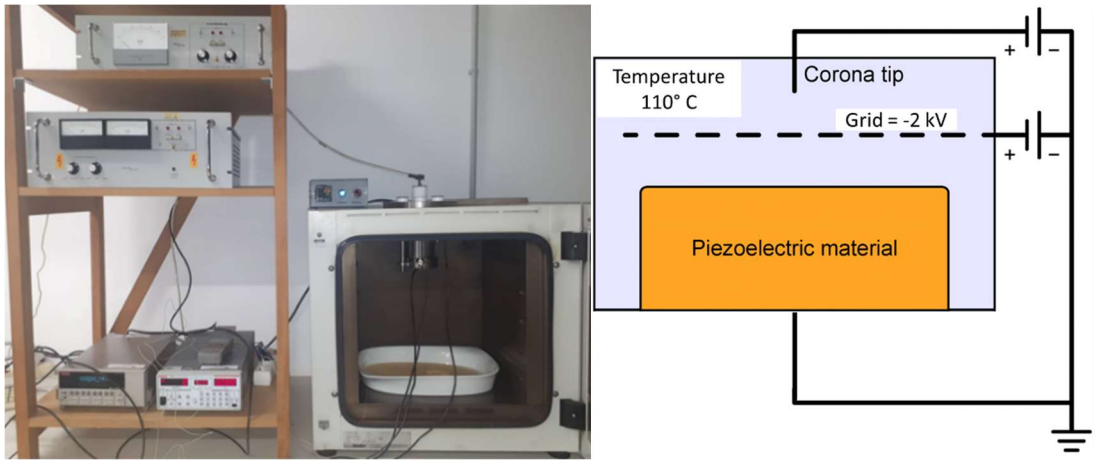

Figure B.2 Apparatus of the corona system used to polarize samples close to the Curie point (left) and corona tip and grid schematic (right).

C. DTA-TG mixtures analysis

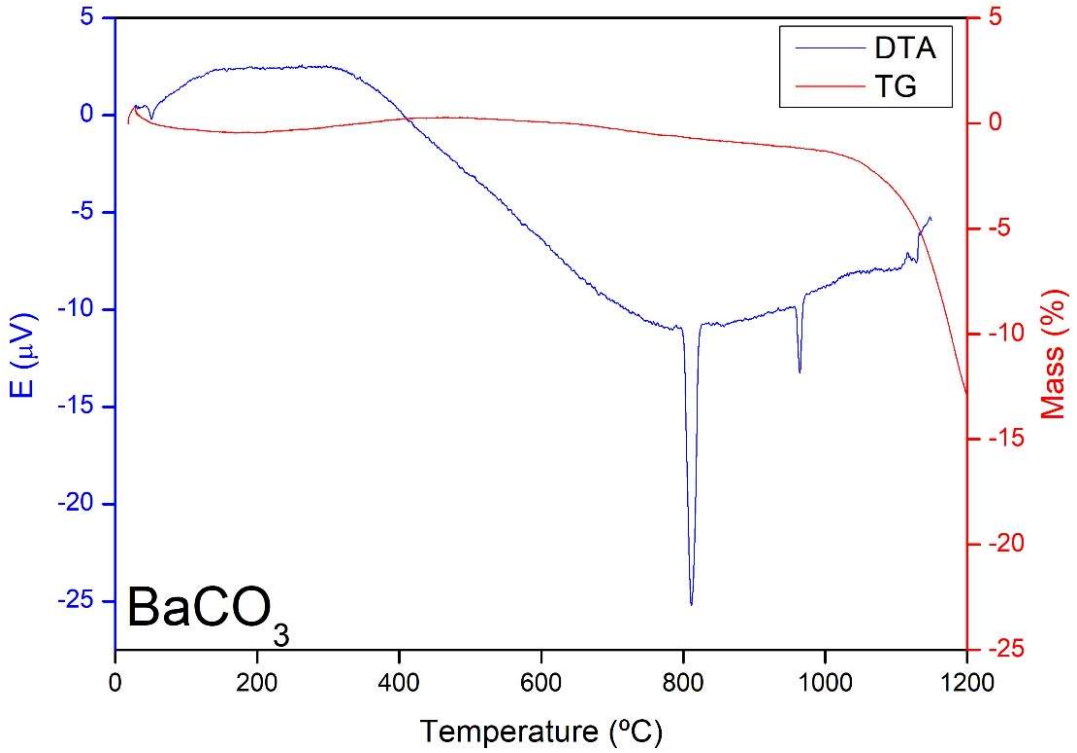

Figure C.1 $BaCO_3$ analytical reagent DTA-TG analysis.

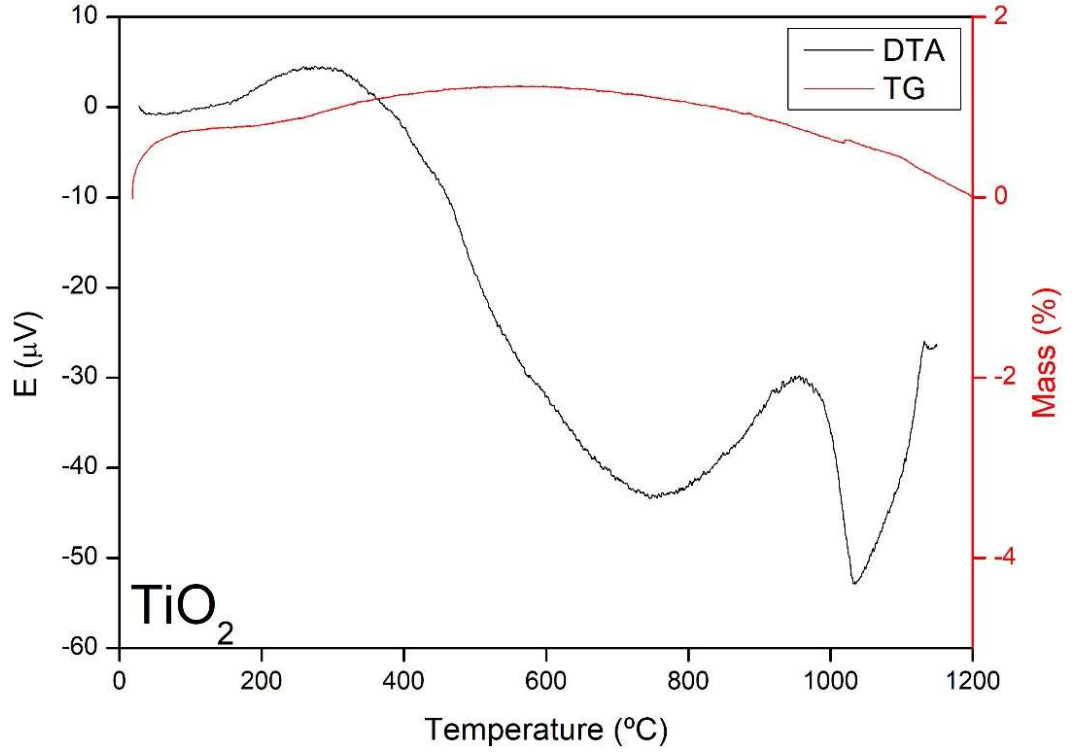

Figure C.2 TiO_2 analytical reagent DTA-TG analysis.

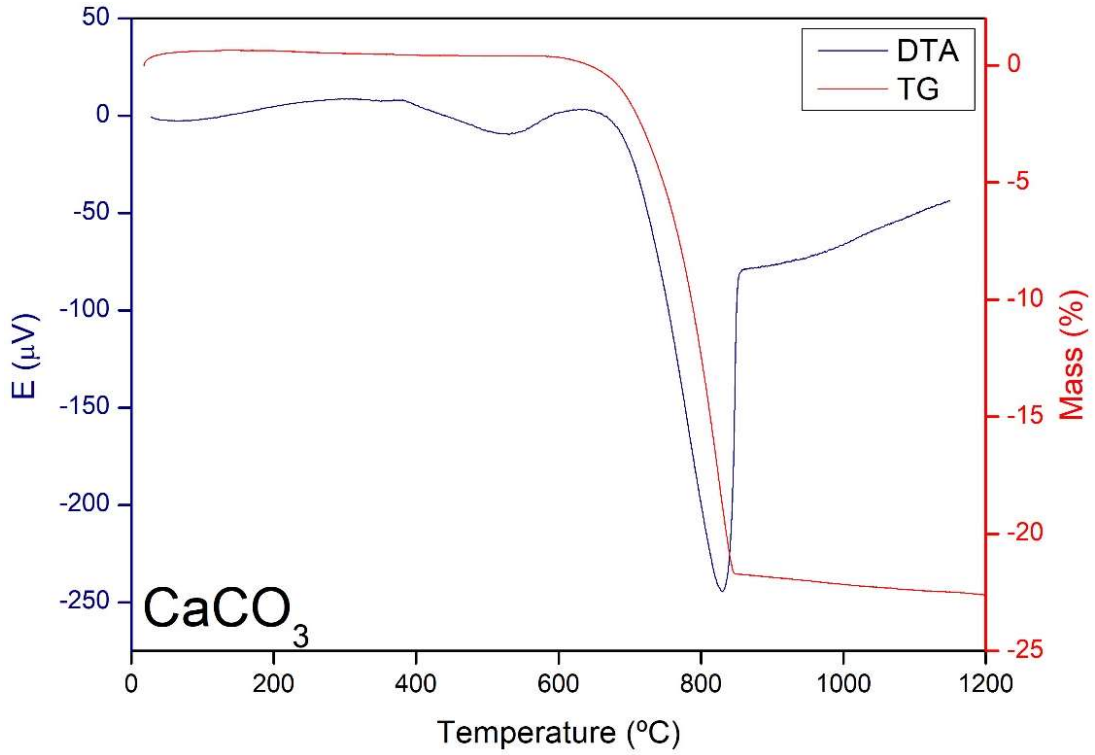

Figure C.3 $CaCO_3$ analytical reagent DTA-TG analysis.

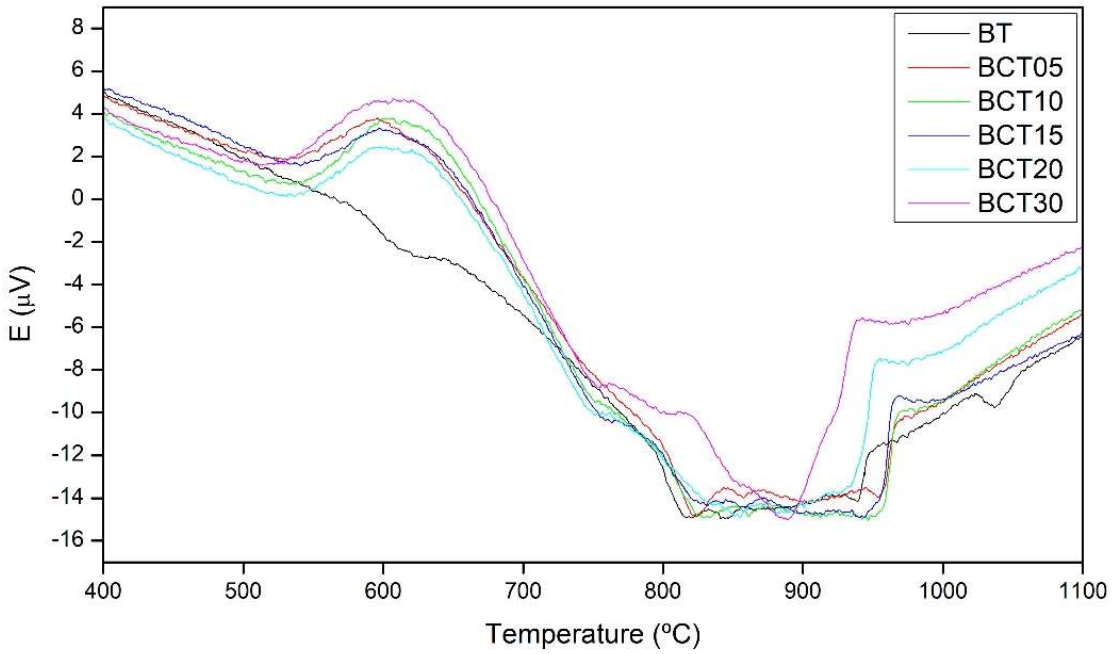

Figure C.4 Differential thermic analysis of all $Ba_{(1-x)}Ca_xTiO_3$ mixtures on the range 400 °C to 1100 °C.

D. Granulometry

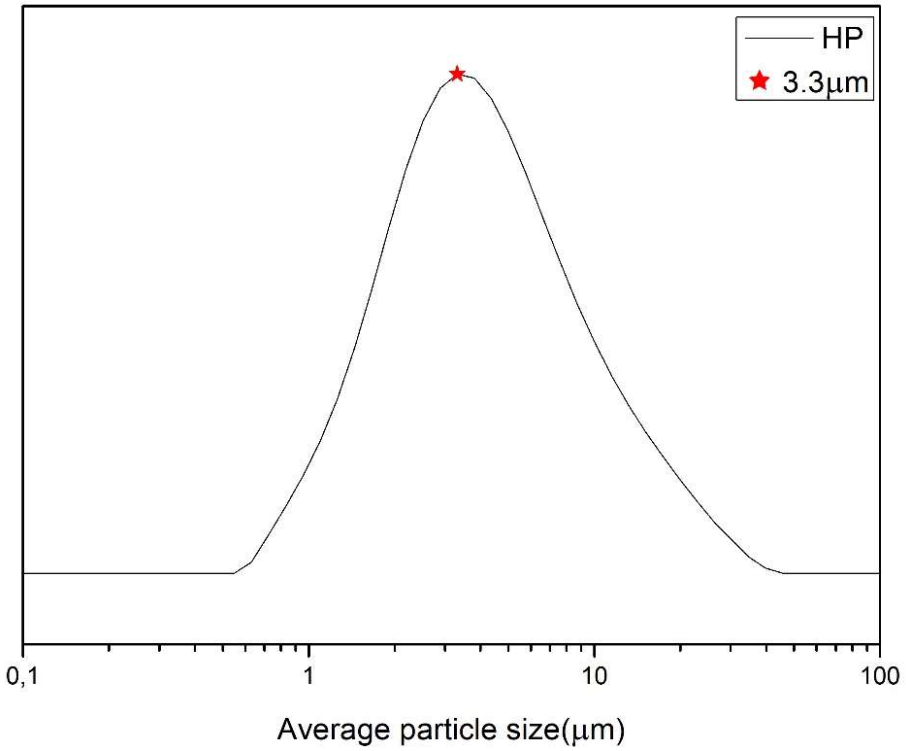

Figure D.1 Granulometry analysis for commercial hydroxyapatite used in composite making.

E. XRD

E.1. Calcium doped barium titanate

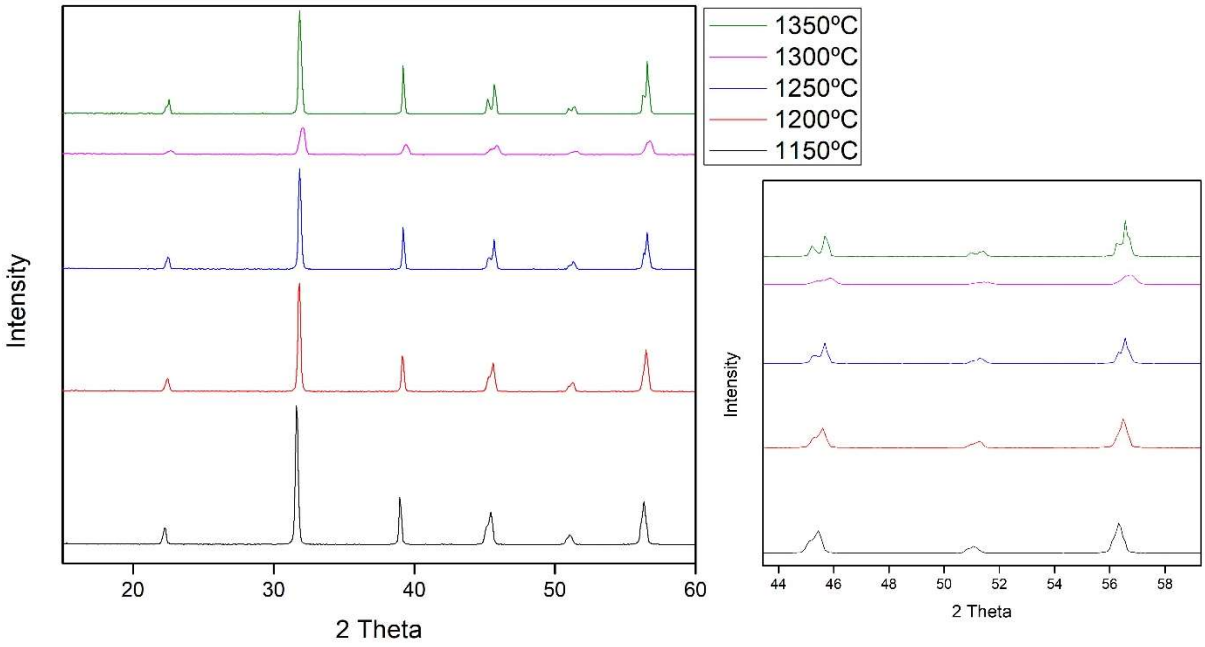

Figure E.1 XRD analysis for BT samples sintered at different temperatures from 1150 °C to 1350 °C.

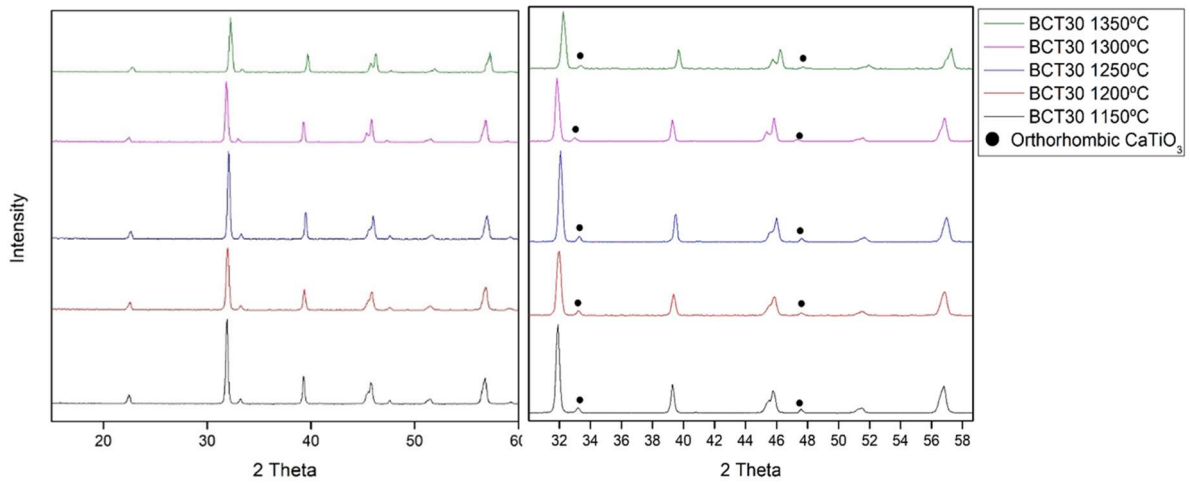

Figure E.2 XRD analysis for BCT30 samples sintered at different temperatures from 1150 °C to 1350 °C (on top) and zoom on diffractograms in areas with peaks of $CaTiO_3$ (bellow).

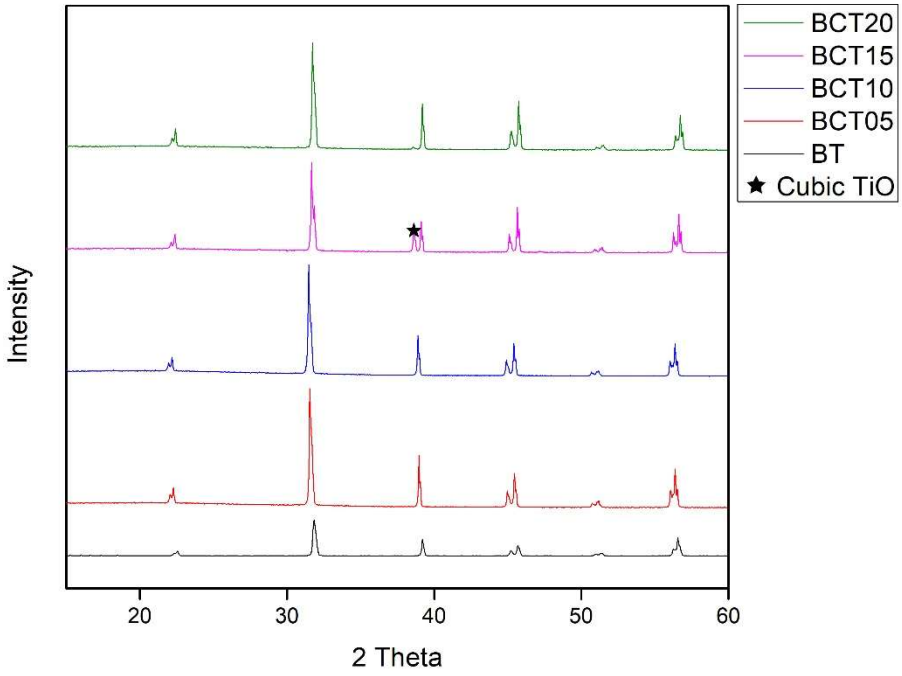

Figure E.3 XRD for $Ba_{(1-x)}Ca_xTiO_3$ $0 \leq x \leq 0.15$ mixture sintered at 1350 °C. Sample BCT15 is the only sample to present a double peak below $2\vartheta = 40°$ and it might be due to a different conformation of titanium during sintering.

E.2. Hydroxyapatite composites

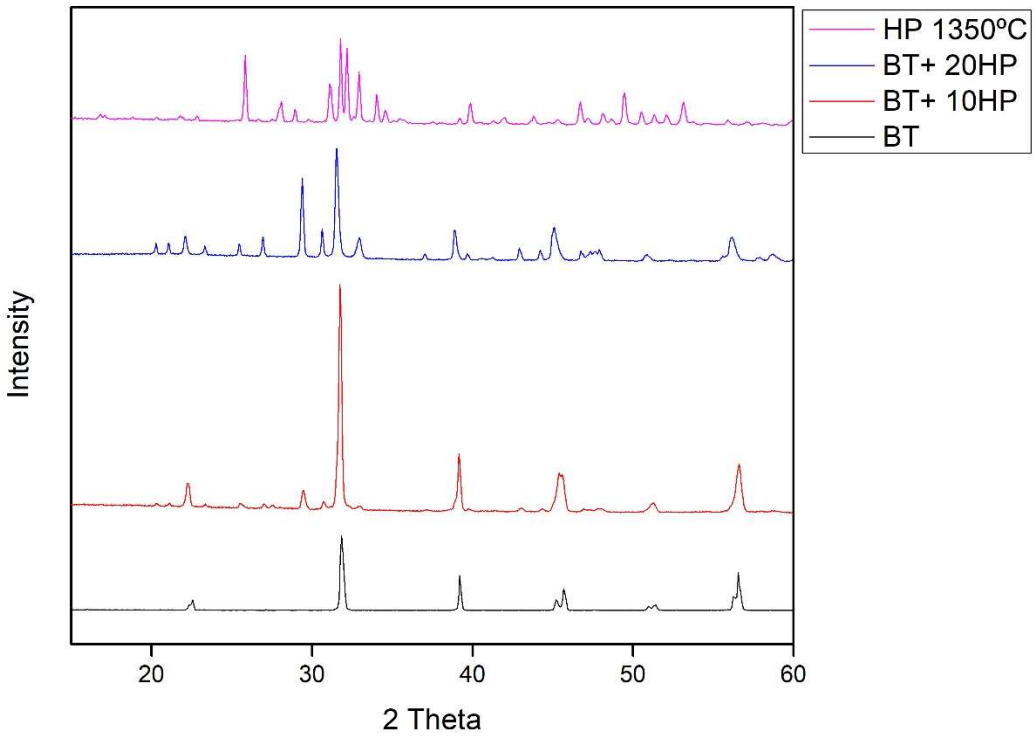

Figure E.4 X-ray diffraction of all BT and hydroxyapatite sintered at 1350 °C.

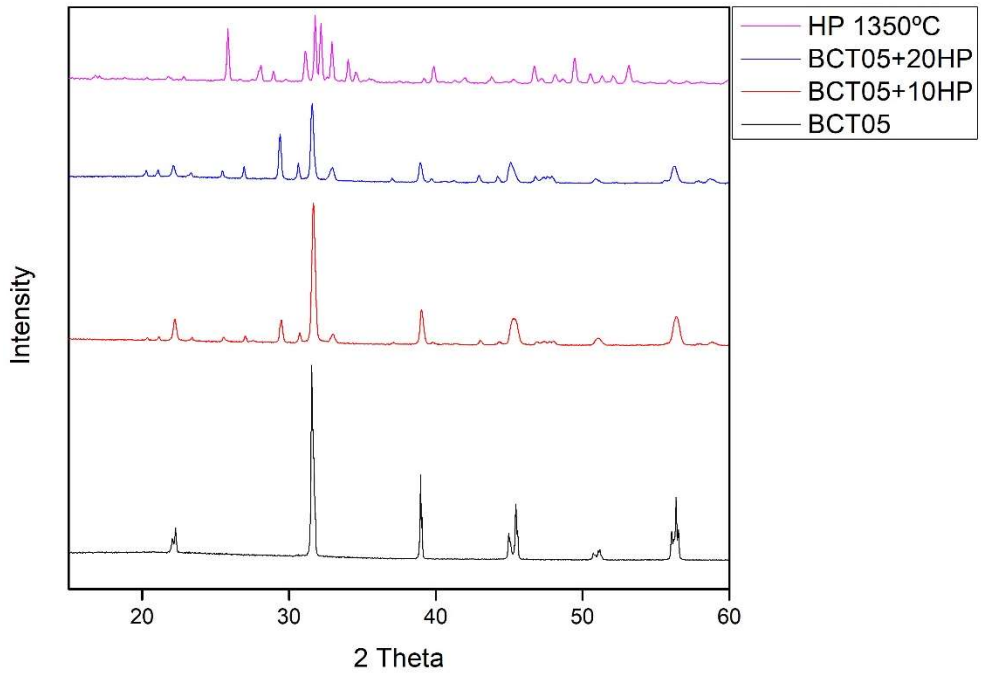

Figure E.5 X-ray diffraction in order to compare BCT05 composites with HP and solo BCT05, all 1350 °C sintered.

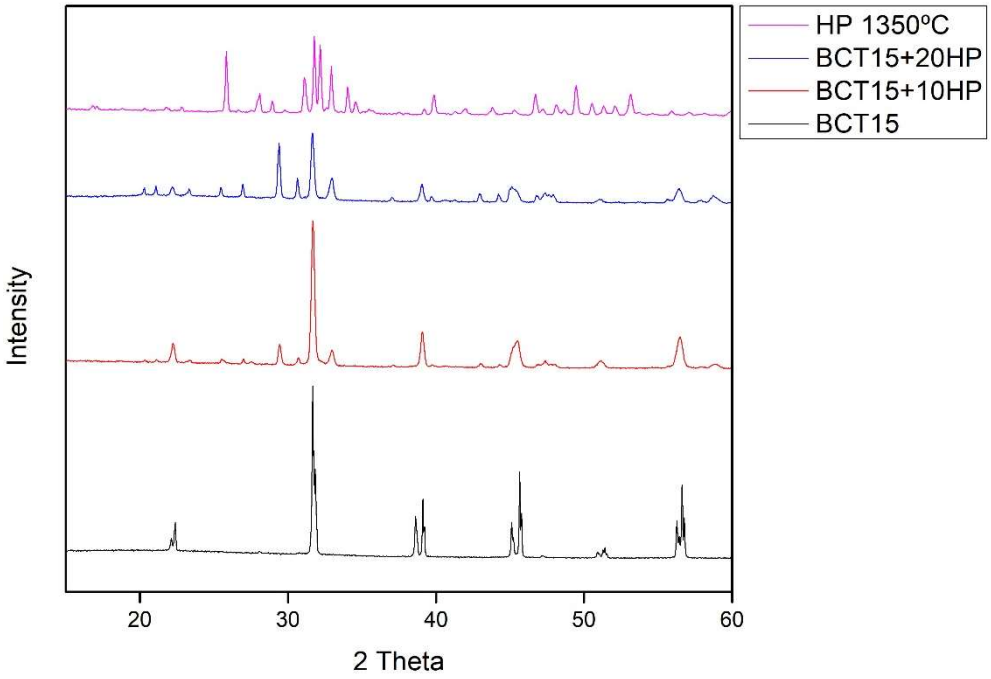

Figure E.6 X-ray diffraction for all BCT15 composites to be compared with BCT15 solo and HP, all 1350 °C sintered.

F. FTIR

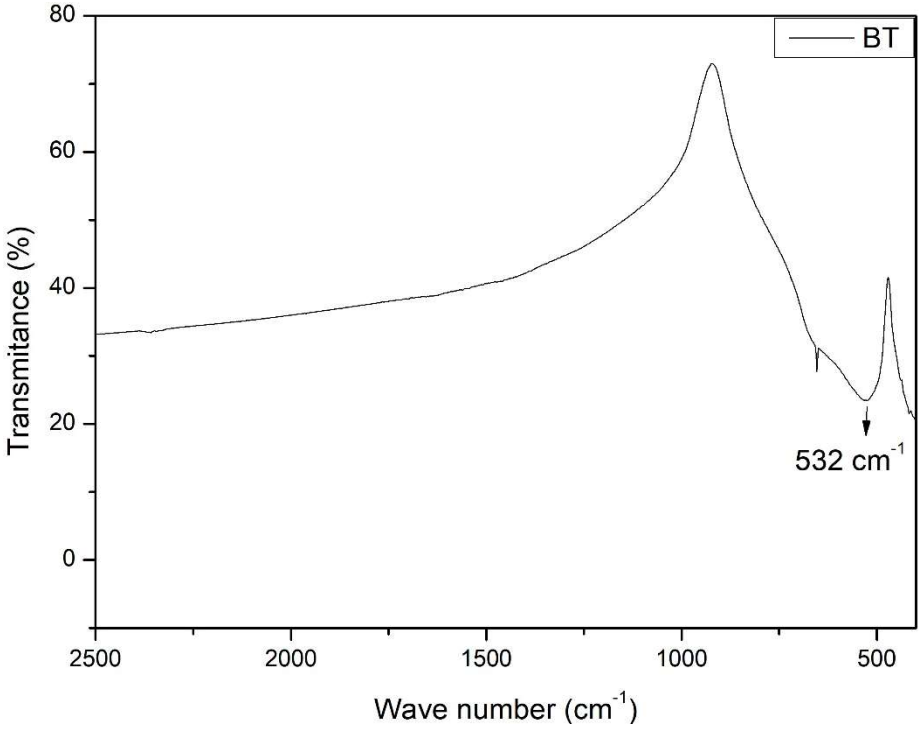

Figure F.1 Barium titanate sintered at 1350 °C FTIR spectrum

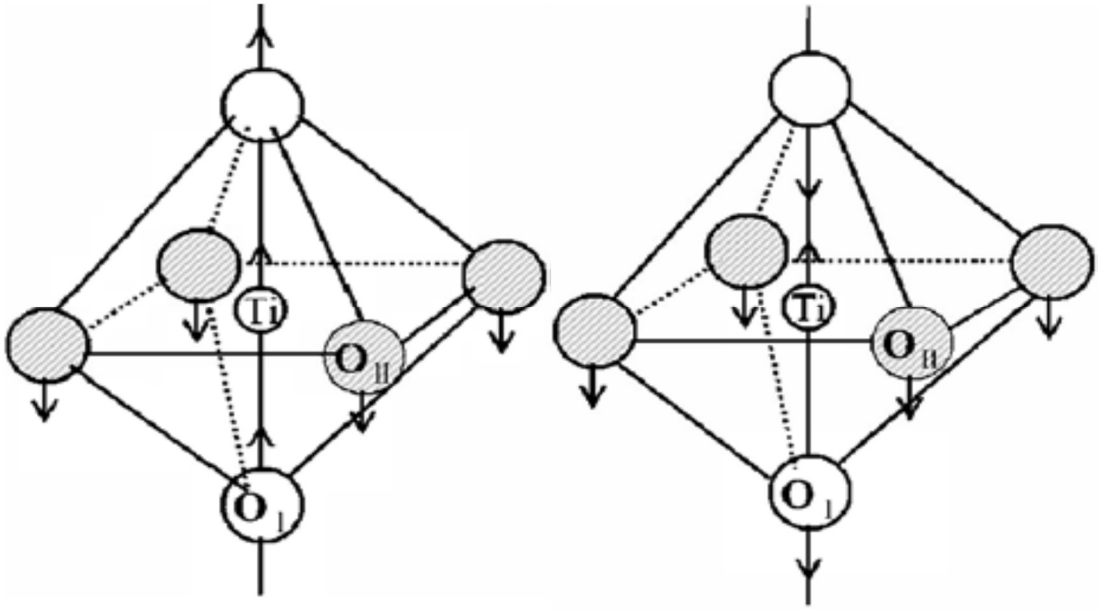

Figure F.2 Ti-O vibration modes: Bending vibration (left), stretching vibration (right) [61].

G. Raman analysis of every mixture

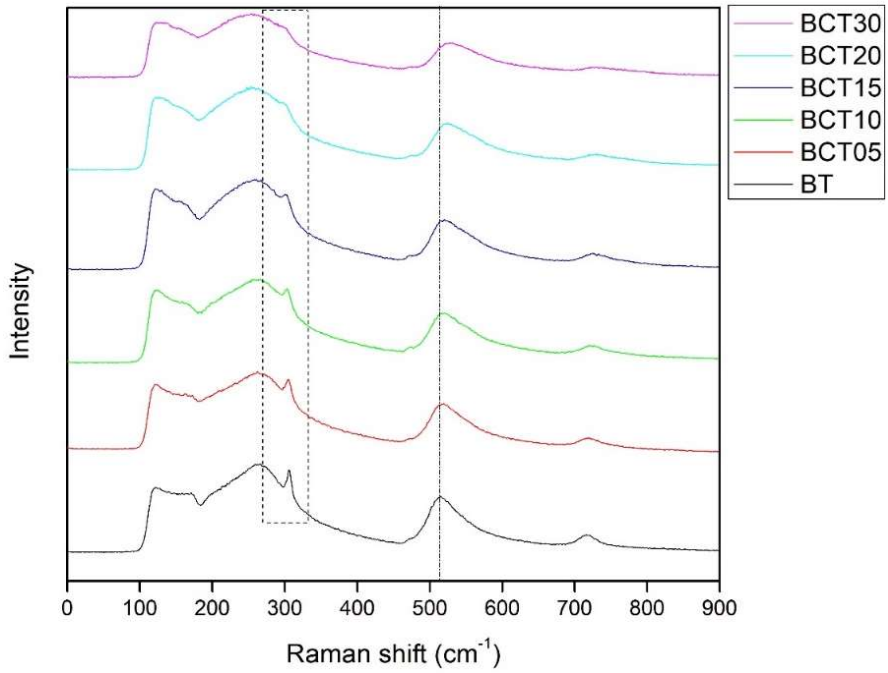

Figure G.1 Raman analysis of all the mixtures $Ba_{1-x}Ca_xTiO_3$ sintered at 1350 °C. Note along the increase of calcium presence the disappearance of the 309 cm^{-1} peak visible in BT inside the dashed rectangular. It is also noticeable the progression of a second peak signed with the dot-dash line to higher Raman shift values in function of calcium presence.

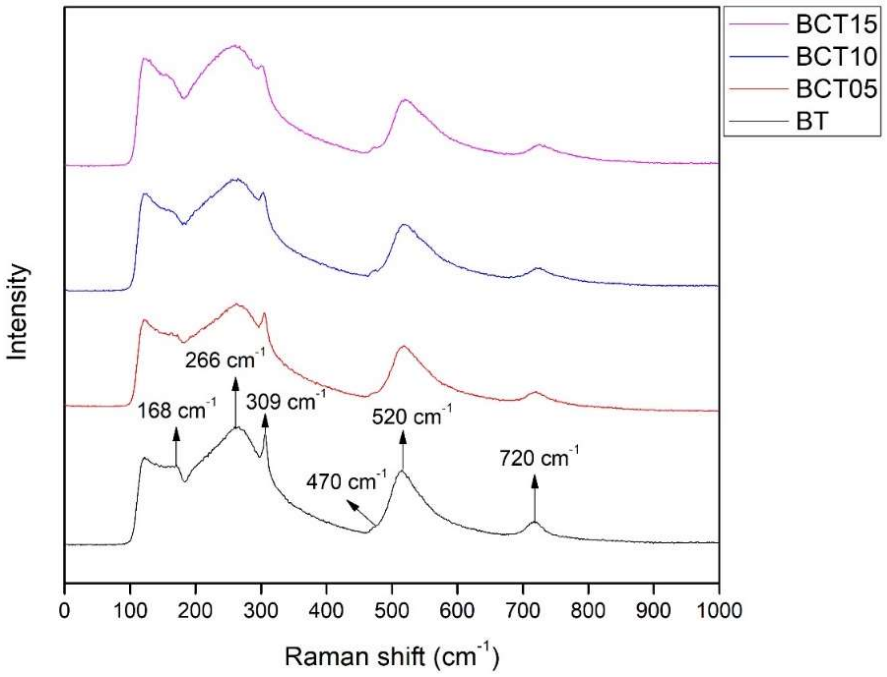

Figure G.2 Raman analysis of the 1350 °C sintered mixtures that qualify to composite making. Up to BCT15 is possible to spot the 309 cm^{-1} peak that assures tetragonality of the material. The perturbation spotted in 470 cm^{-1} is also related with tetragonality.

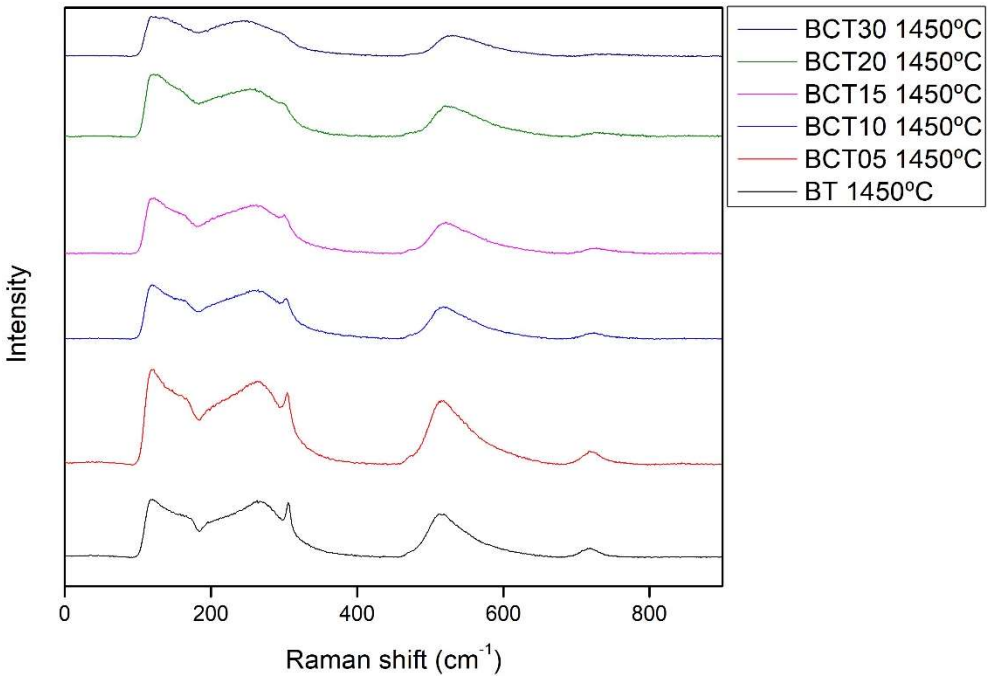

Figure G.3 Raman analysis of $Ba_{(1-x)}Ca_xTiO_3$ $0 \leq x$ 0.3 mixtures sintered at 1450 °C.

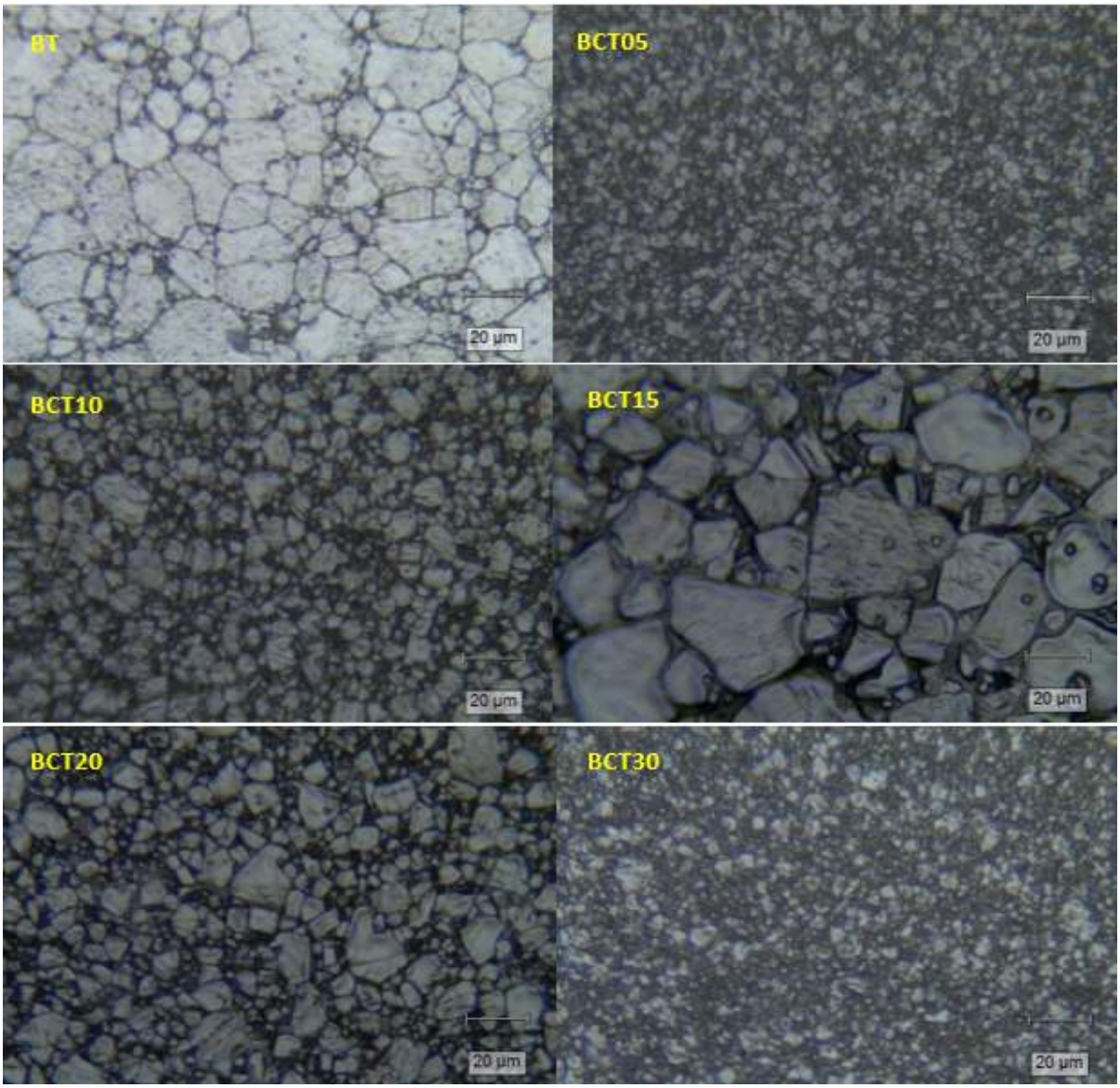

Figure G.4 Raman microscopy for all $Ba_{(1-x)}Ca_xTiO_3$ mixtures.

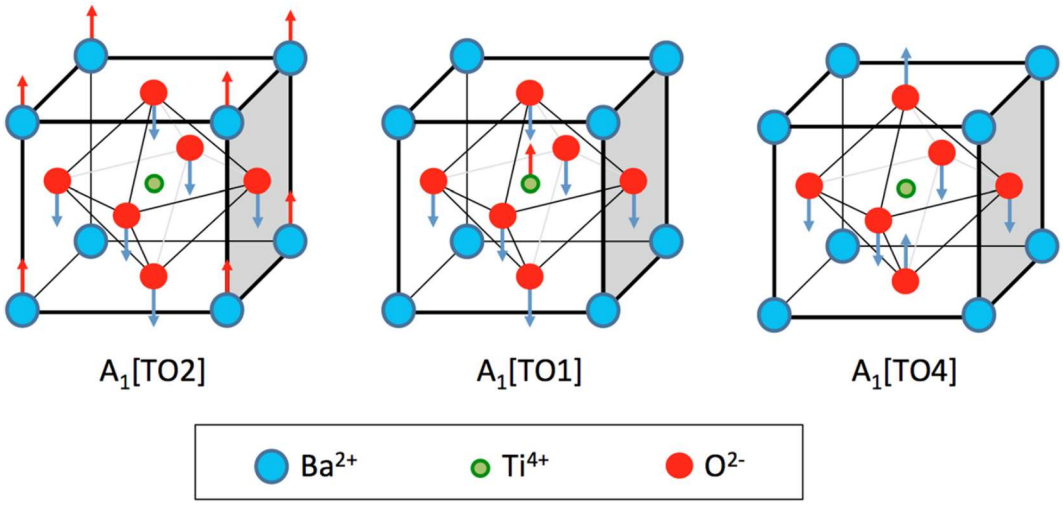

Figure G.5 Raman vibration modes [61]

H. DSC

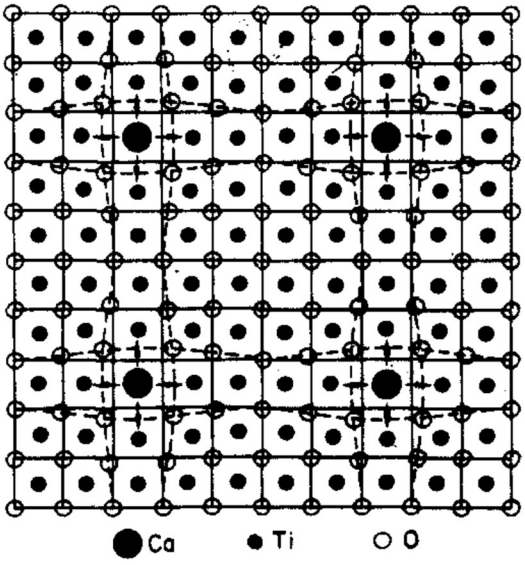

Figure H.1 Lattice distortion caused by Ca^{2+} substitution on B-site of ABO_3 perovskite structure [28].

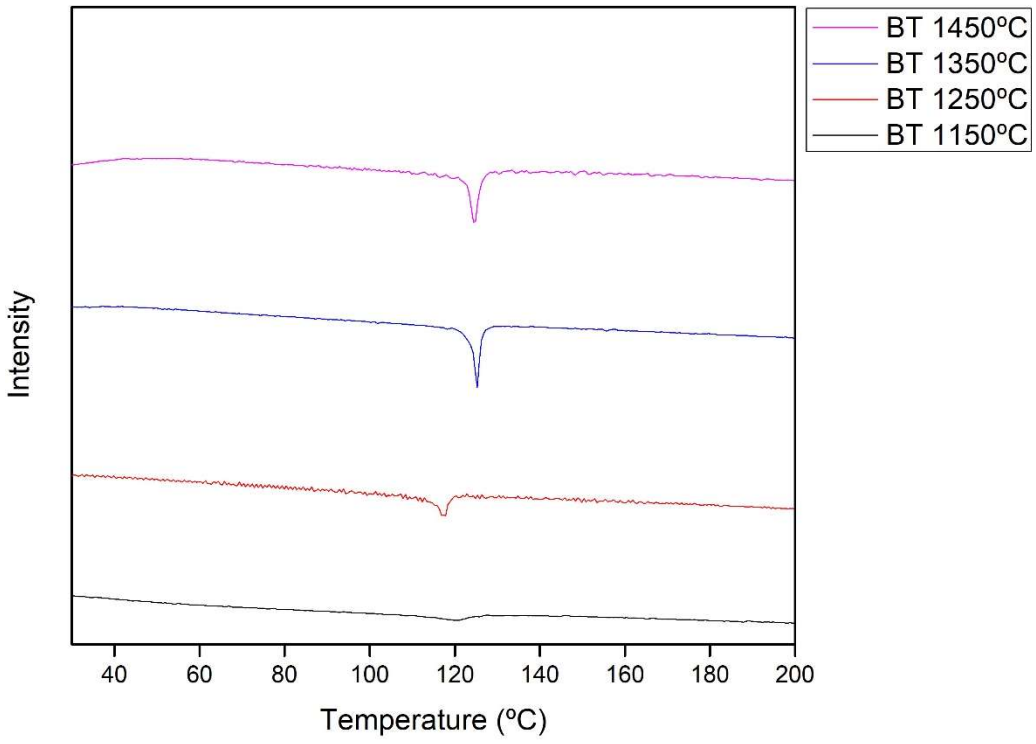

Figure H.2 DSC analysis of BT samples sintered at different temperatures 1150 °C, 1250 °C, 1350 °C and 1450 °C.

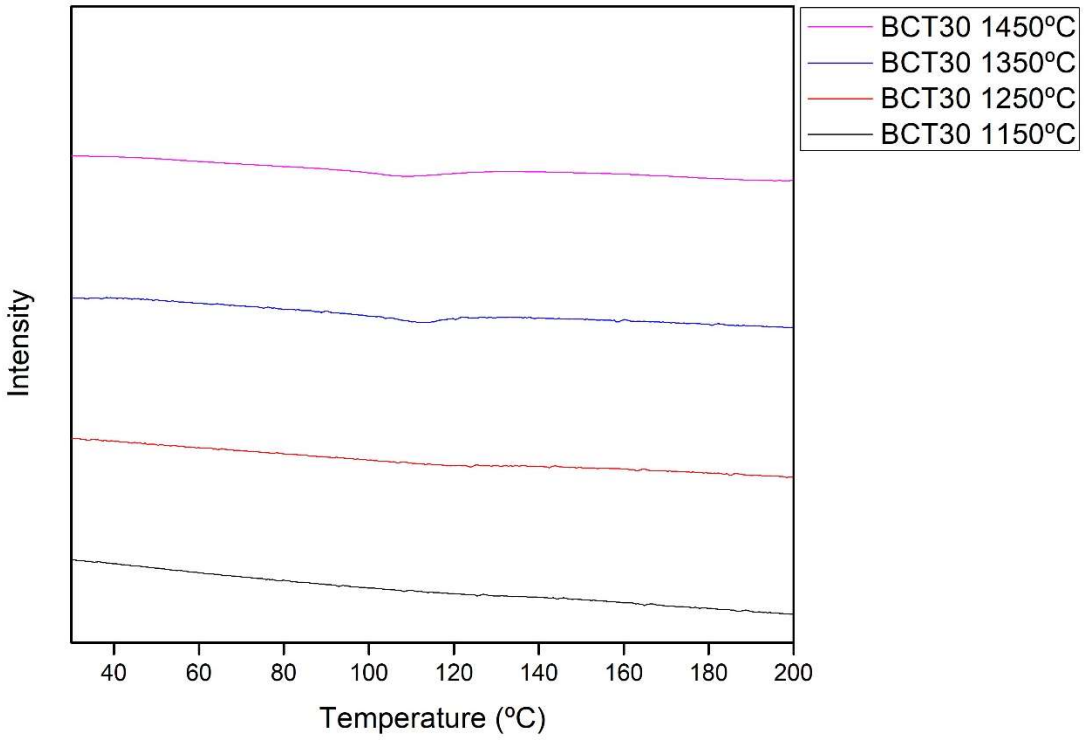

Figure H.3 DSC analysis of BCT30 samples sintered at 1150 °C, 1250 °C , 1350 °C and 1450 °C.

I. SEM and EDS

I.1. Calcium doped barium titanate

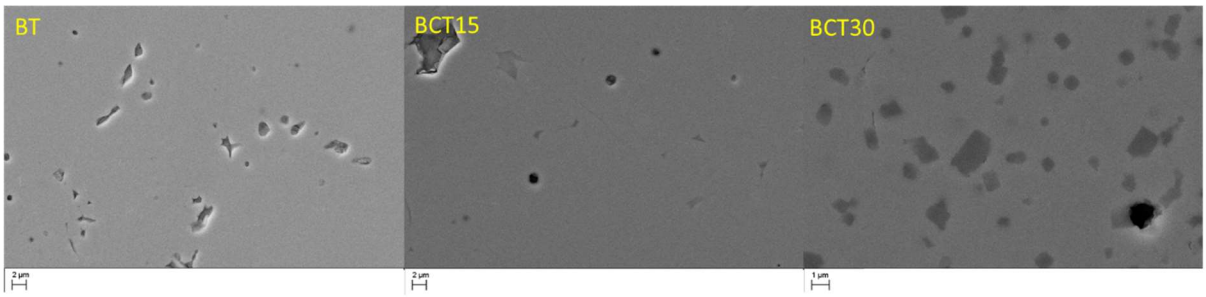

Figure I.1 SEM analysis for diamond paste polished samples of BT, BCT15 and BCT30.

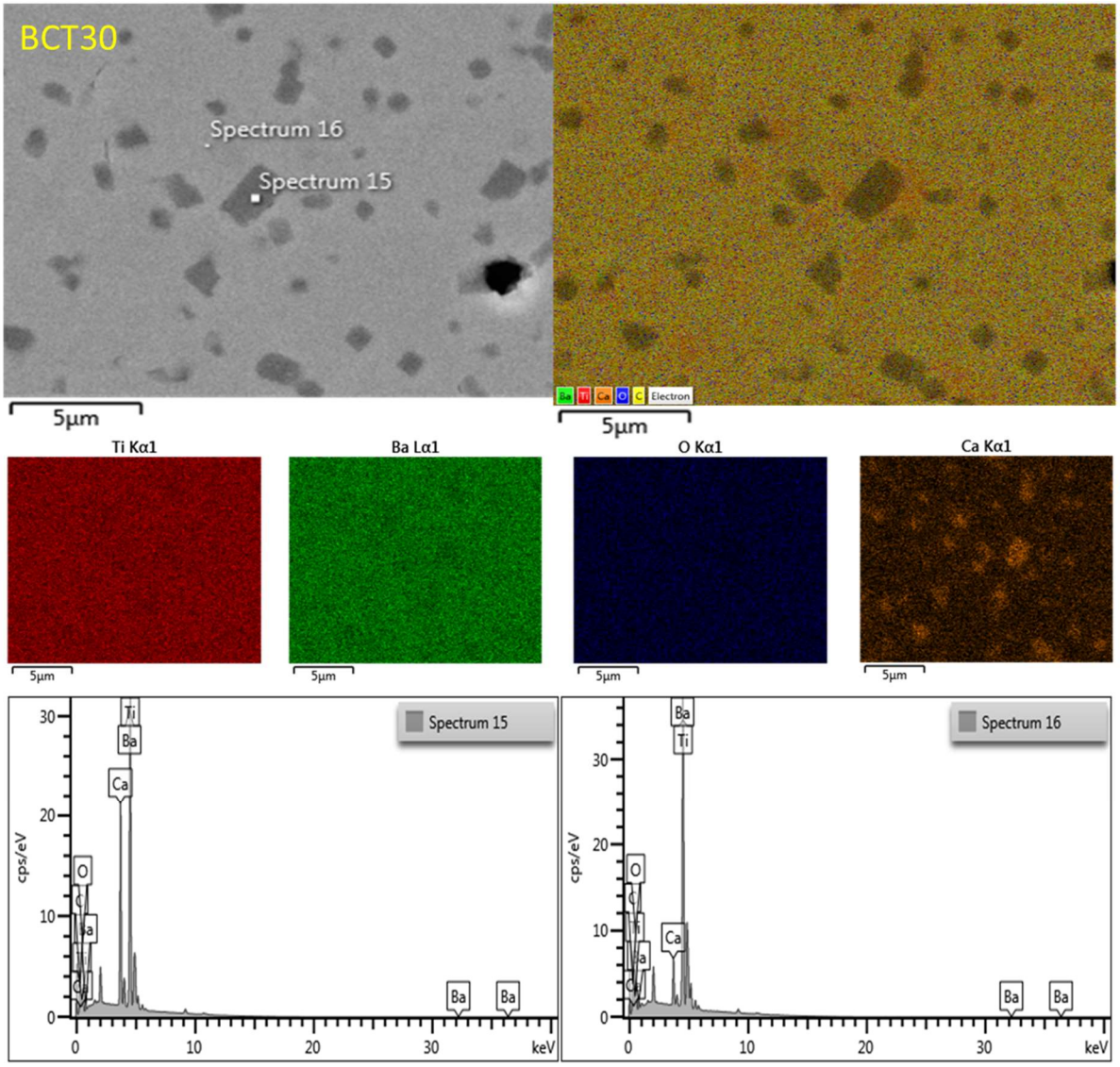

Figure I.2 SEM and EDS analysis for BCT30 polished sample.

I.2. Hydroxyapatite composites

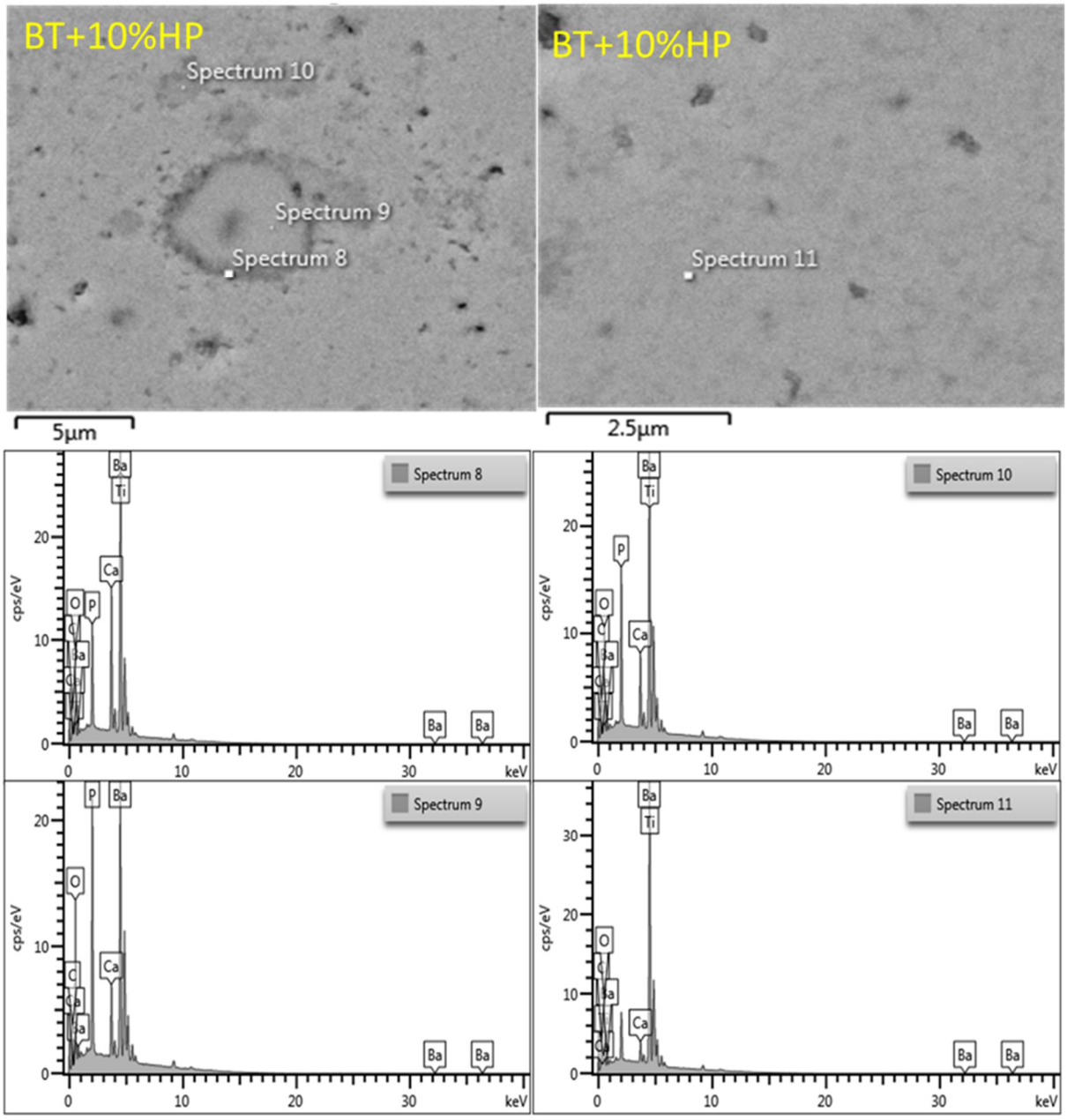

Figure I.3 BT/HP (90/10) composite under SEM microscopy with EDS quantification on four different points of the sample.

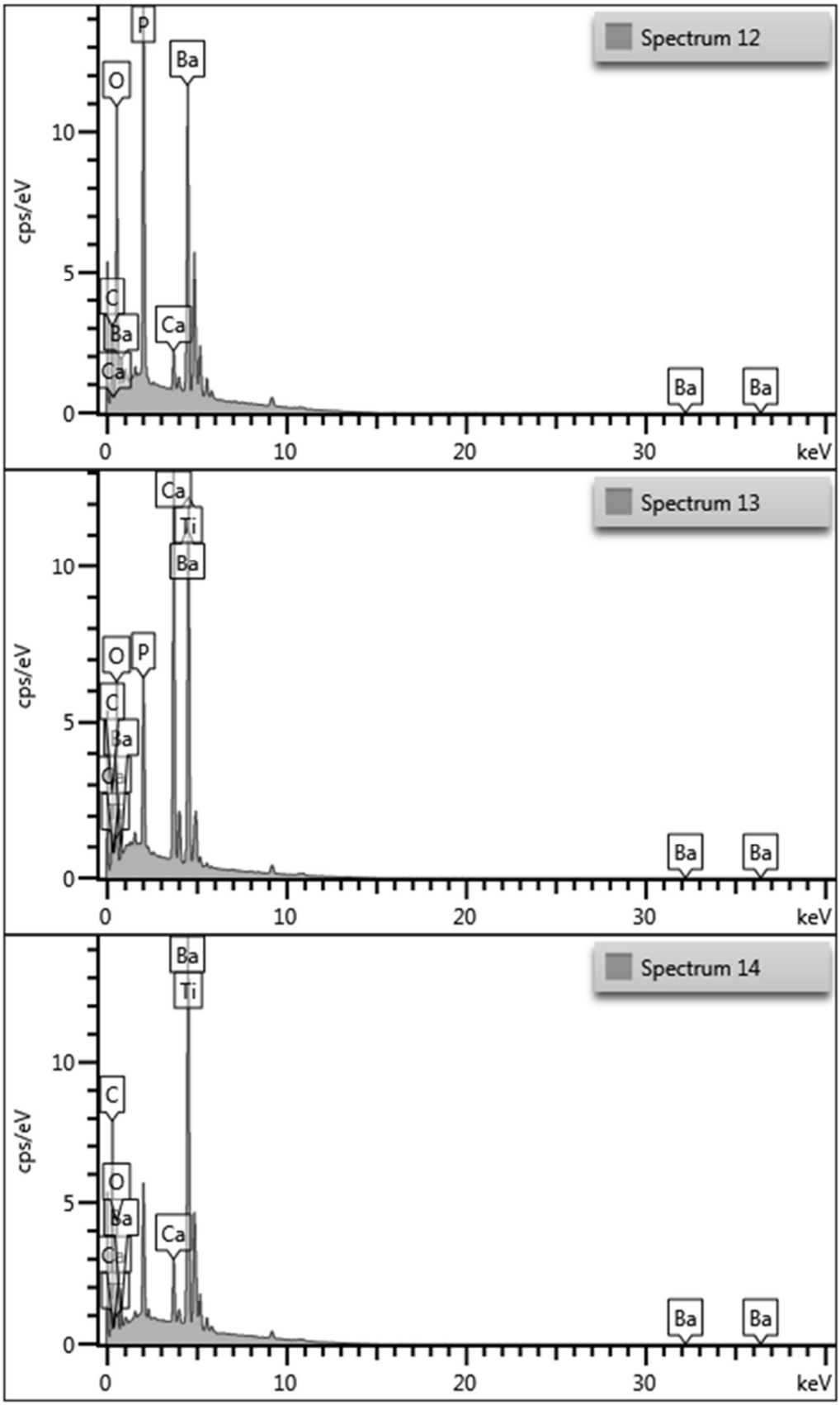

Figure I.4 EDS quantification of BCT10/HP (90/10) composite. SEM imaging of this same sample is present in section 4.3.2, figure 4.21.

J. Cytotoxicity

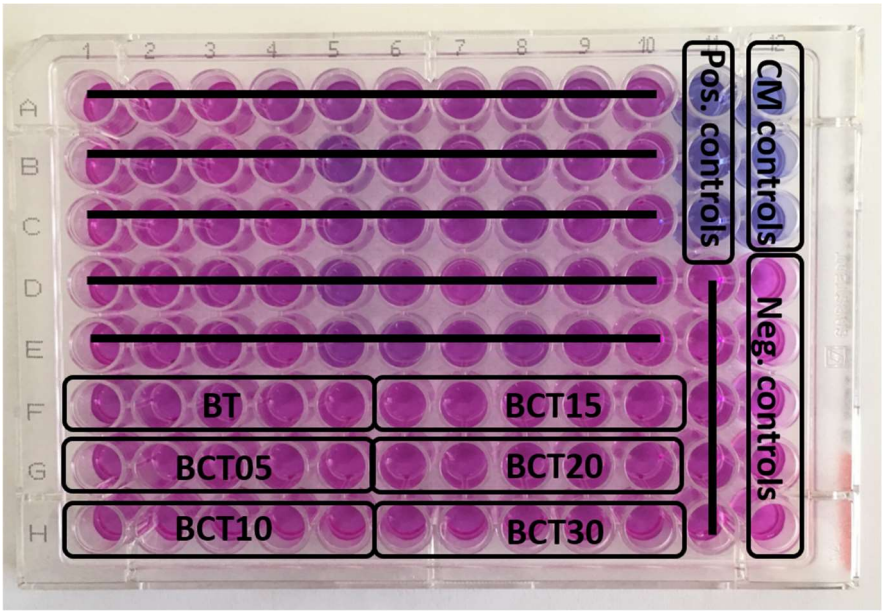

Figure J.1 Labelled plate used in cytotoxicity assays with the positions of each intervenient in order to account for every mixture cell viability.

The cytotoxicity study was performed using the extract method which consists of placing the cells in contact with the medium where the mixtures were previously incubated. To determine the number of viable cells, a colorimetric method based on the resazurin reagent was used, which is reduced by the living cells. For the extract production, different samples of 40 mg were pre-sterilized with UV irradiation for 1 hour. Subsequently, each mixture was placed in 2.5 mL of medium, at 37 °C, for 48 hours. Cells were seed into 96-well plates, like in Figure J.1, and 5 wells were used for each $Ba_{(1-x)}Ca_xTiO_3$ (BCT) $0 \leq x \leq 0.3$ mixture (30 wells total: 5 replicas for the same concentration). In addition, negative (column 12, 5 replicas from line D to H), positive (column 11, 3 replicas) and cell-mediated controls (column 12, 3 replicas from line A to C) were performed, serving as reference for calculating cell viability.

The plate was again placed in the incubator for 48 h. Resazurin was used for cell viability analysis. After 48 hours in the incubator, the plate was removed and as well as the medium contained in each well. A solution of 90% of medium and 10% resazurin was then placed in each well. The viability analysis consists of a change in the colour of the solution (a pink colour means live cells and a blue colour means the presence of dead cells. The plate was placed in the incubator for 4 hours. After this time, the absorbances of each well (at 570 nm and 600 nm) were measured in a Biotek ELX800 microplate reader. To determine the cell viability (%), medium control and uncertainties, the means of each 5 replicates were calculated for each sample and the following expressions were used:

Medium Control = $\text{"Average } i\text{"} - \text{"Average } CM\text{"}$

Cell Viability = $\frac{\text{"}Average\ control\text{"}}{\text{"Average C-"} - \text{"}Average\ CM\text{"}}$

Uncertainty = $\sqrt{\sigma^2 + \sigma_{CM}^2}$

Where σ represents the standard deviation for each of the concentrations used and σ_{CM} is the standard deviation of the control medium. In order to analyse cell viability, it is necessary to take into

account four denominations according to the percentage of viability obtained and they are: viability greater than 90 % the material is non-cytotoxic; with cell viability between 80% and 89 % considered to be slightly cytotoxic; between 50 % and 79 % is moderately cytotoxic; if it is less than 50 % is severely cytotoxic.

K. Thermal stimulated depolarization currents

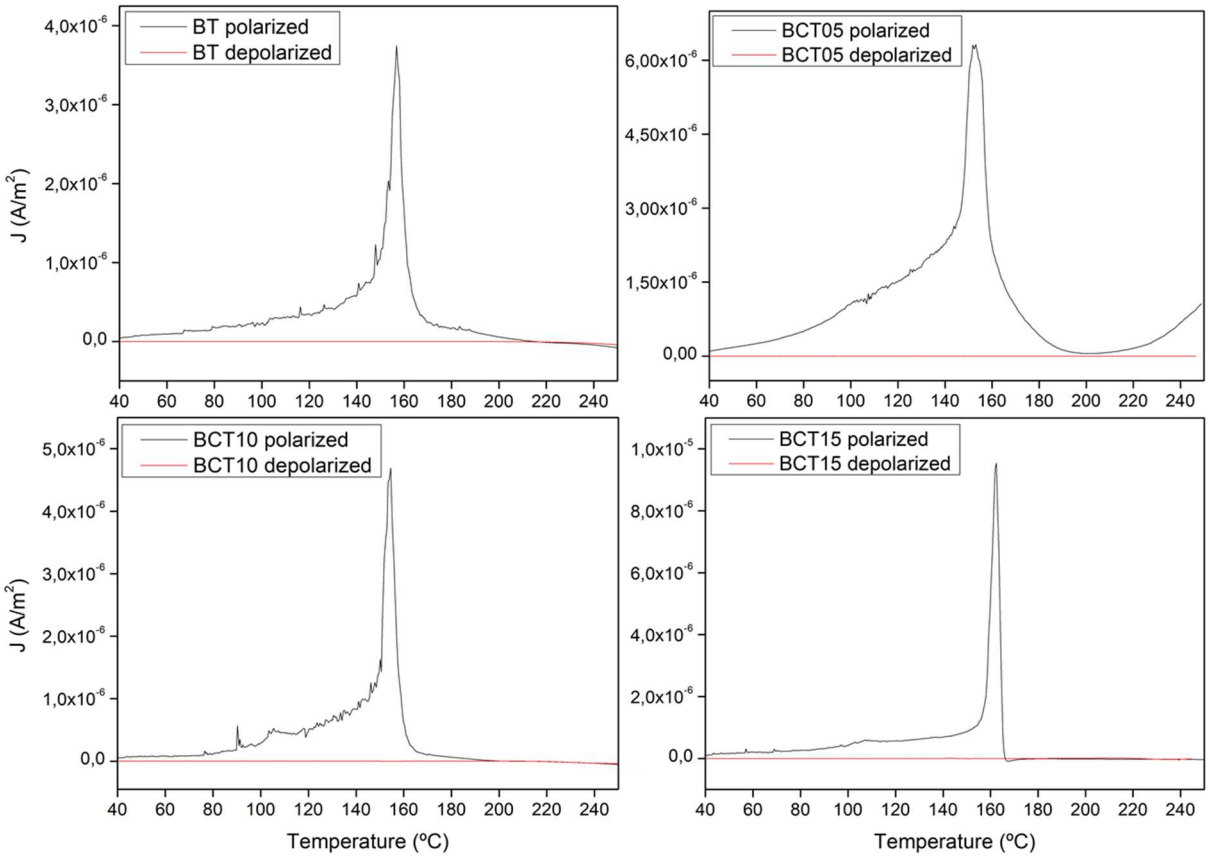

Figure K.1 Results for polarized and depolarized $Ba_{(1-x)}Ca_xTiO_3$ $0 \leq x \leq 0.15$ samples submitted to thermally stimulated depolarization currents.

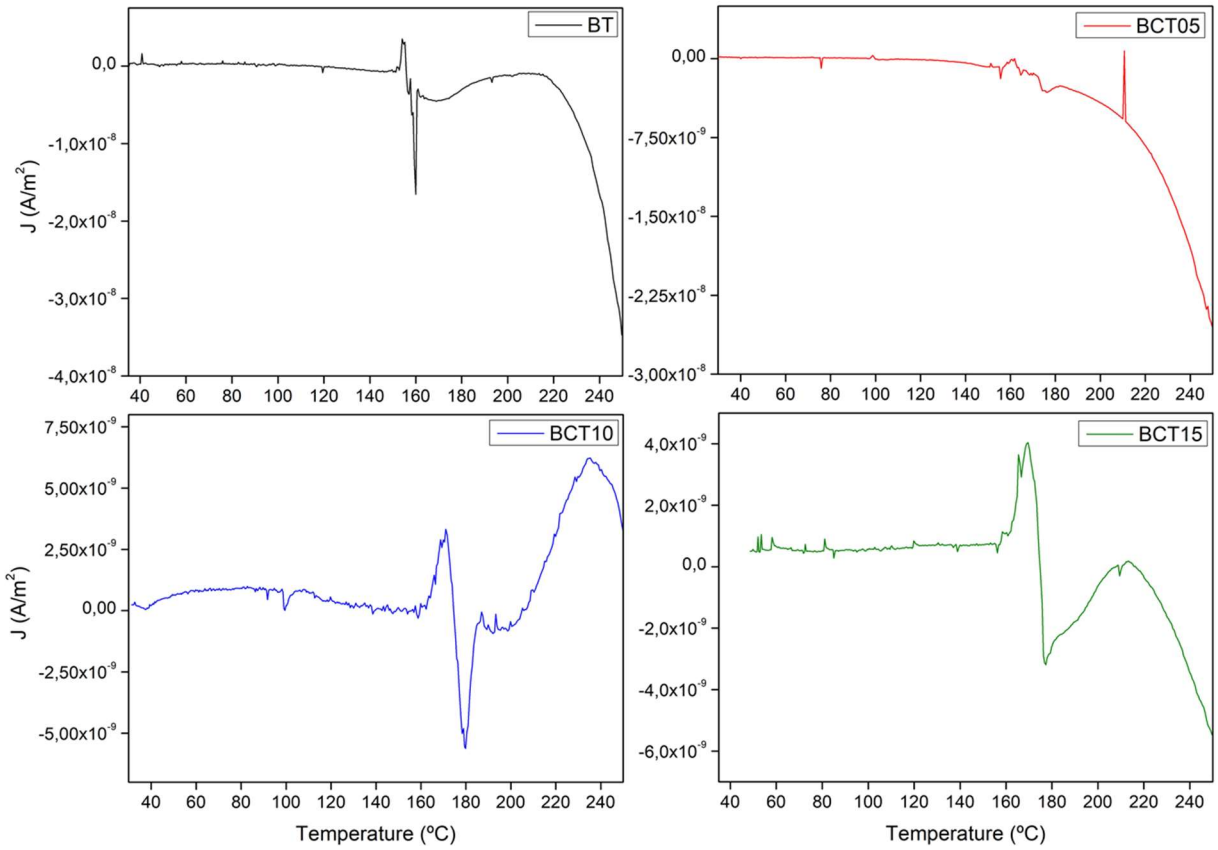

Figure K.2 Never polarized samples TSDC analysis.

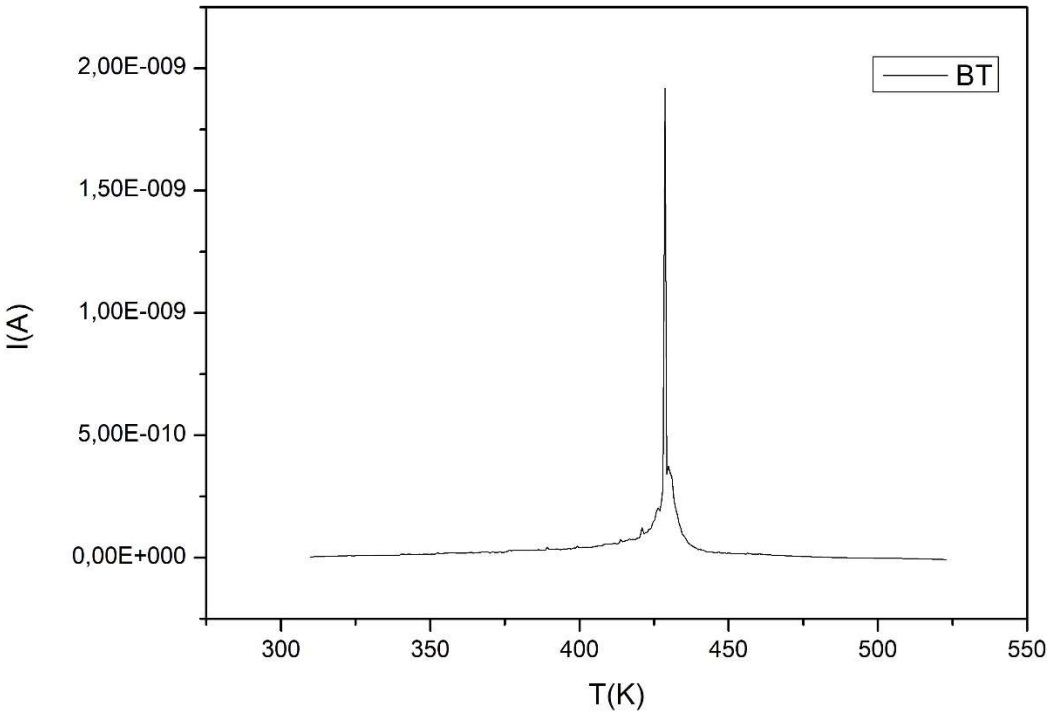

Figure K.3 TSDC spectrum showing a pyroelectric anomalous current on BT sample.

L. Bioactivity essays

Simulated body fluid (1L) was done by preparing a recipient containing 750 ml of deionized water with a magnetic mixer and heated up to 37 °C. The chemical compounds were added to the recipient by the following order and quantities: 7.996 g NaCl, 0.350 g $NaHCO_3$, 0.224 KCl, 0.228 g $K_2HPO_4 \cdot 3H_2O$, 0.305 g $MgCl_2 \cdot 6H_2O$, 40 ml 1M HCl, 0.278 g $CaCl_2$, 0.071 g Na_2SO_4, 6.057 g $(CH_2OH)_3CNH_2$. After the last addition, the mixture keeps being agitated for 10 minutes before pH is measured. Add 1M HCl drops until pH is between 7.2 and 7.4. Add deionized water until the recipient contains 1L total. The solution is kept inside a cooler.

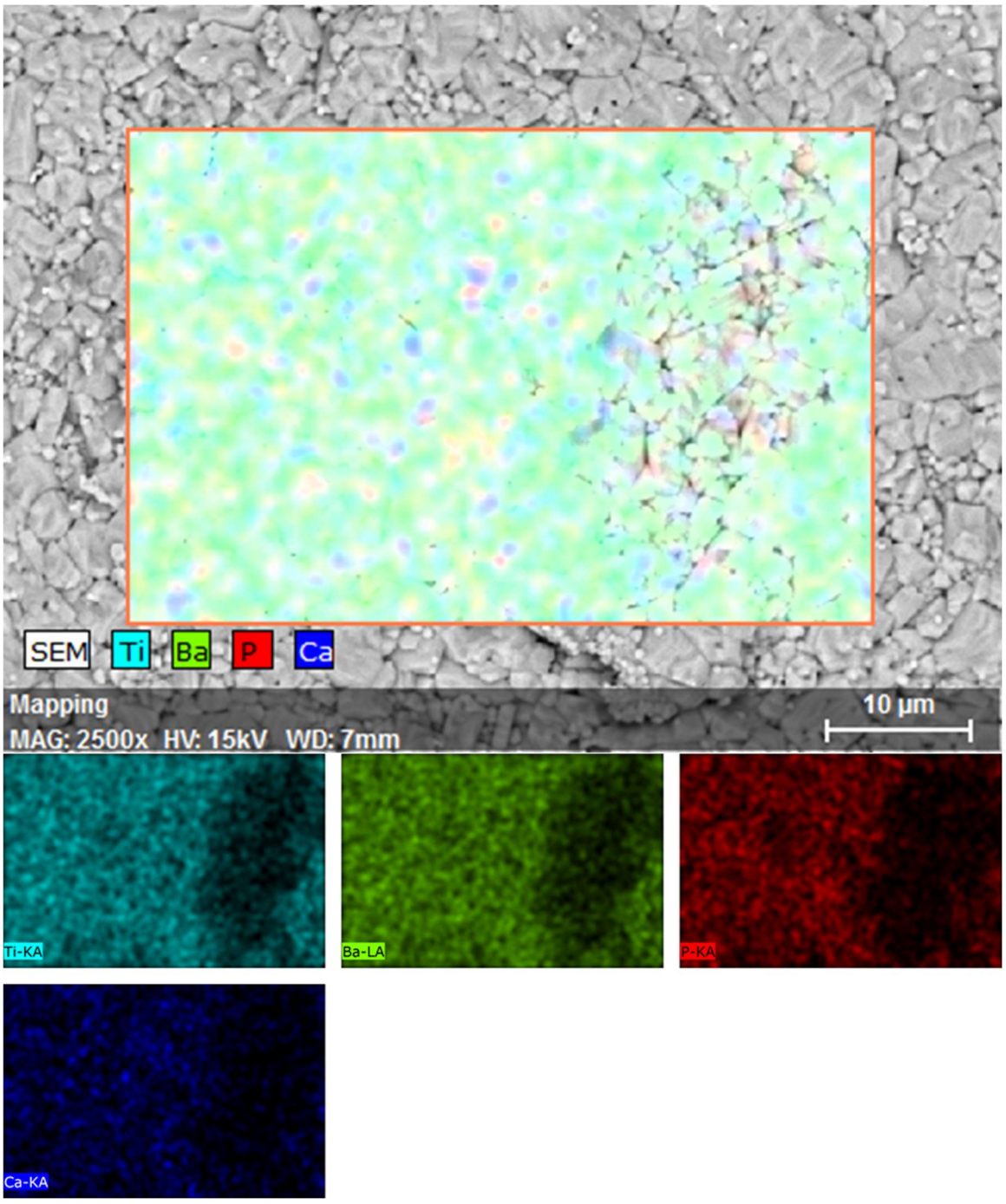

Figure L.1 SEM/EDS results for polarized BCT05 sample after 7 days SBF immersion.

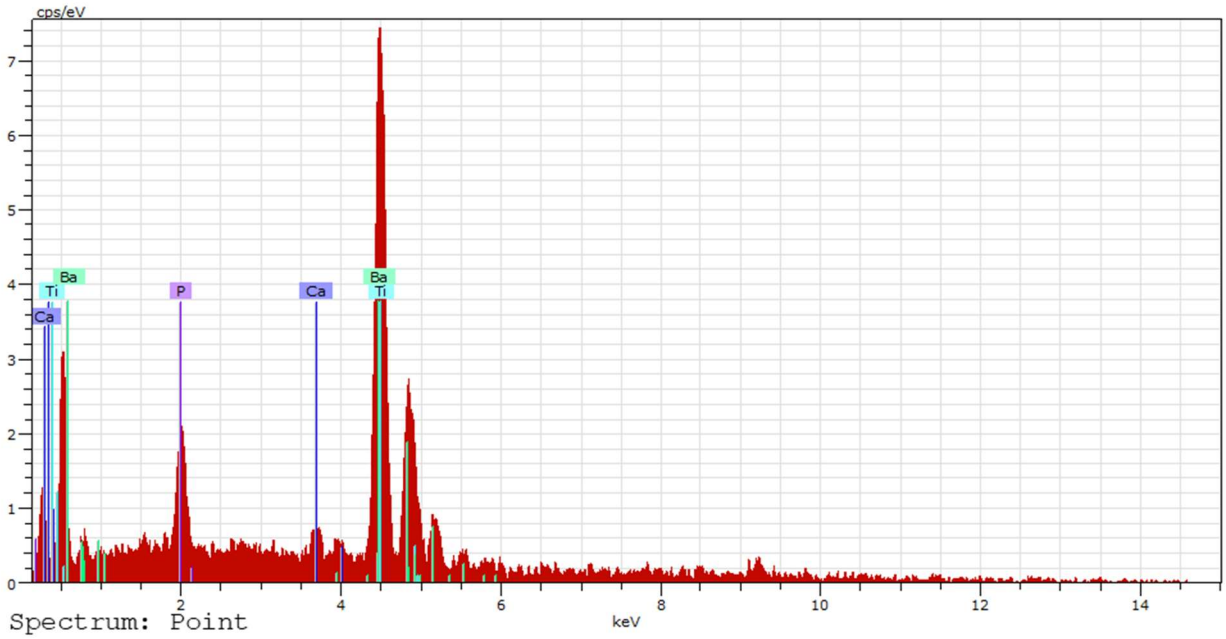

Spectrum: Point

Element	AN	Series	Net	unn. C [wt.%]	norm. C [wt.%]	Atom. C [at.%]
Titanium	22	K-series	2175	23.71	34.49	52.46
Barium	56	L-series	2700	39.85	57.97	30.74
Phosphorus	15	K-series	574	3.99	5.81	13.65
Calcium	20	K-series	160	1.19	1.73	3.15
			Total:	68.75	100.00	100.00

Figure L.2 EDS quantification for polarized BCT05 samples immersed in SBF for 7 days.

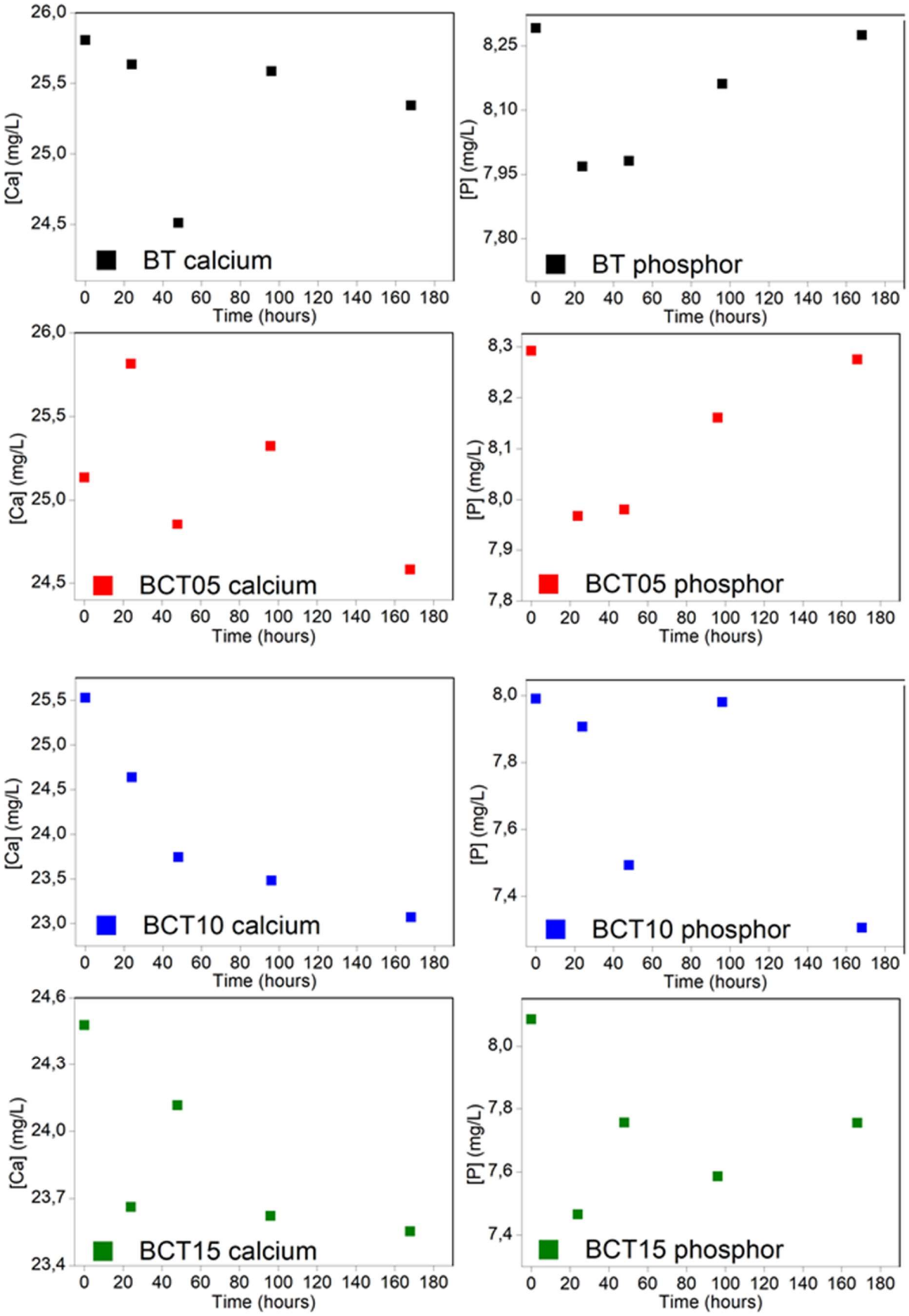

Figure L.3 ICP-AES results for $Ba_{(1-x)}Ca_xTiO_3$ $0 \leq x \leq 0.15$ unpolarized samples 7 days immersion in SBF. Samples were put inside a recipient containing 250 mL when the test starts. Each graph shows the SBF calcium and phosphor concentration varying during the 7 days period.

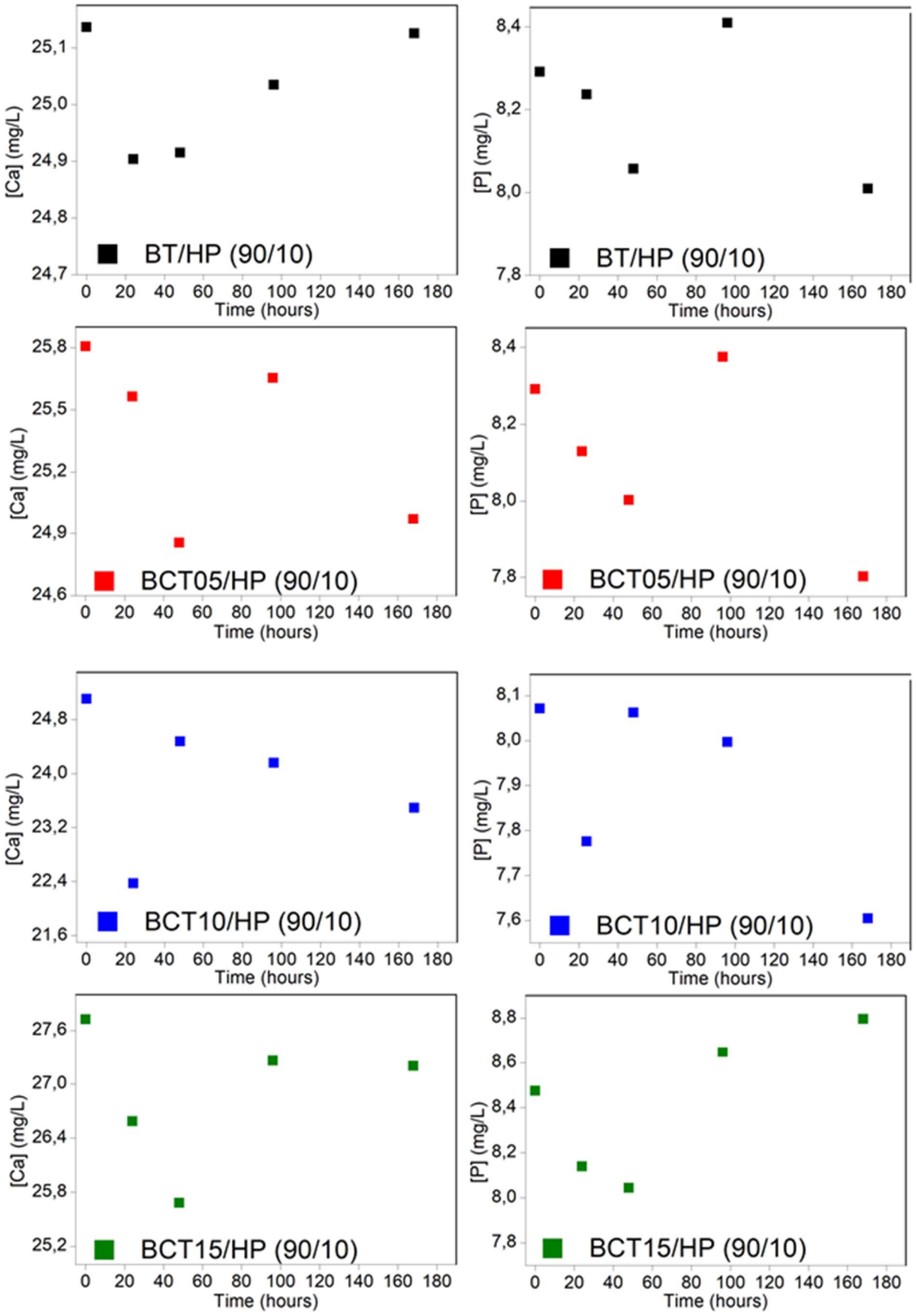

Figure L.4 ICP-AES results for polarized composites.

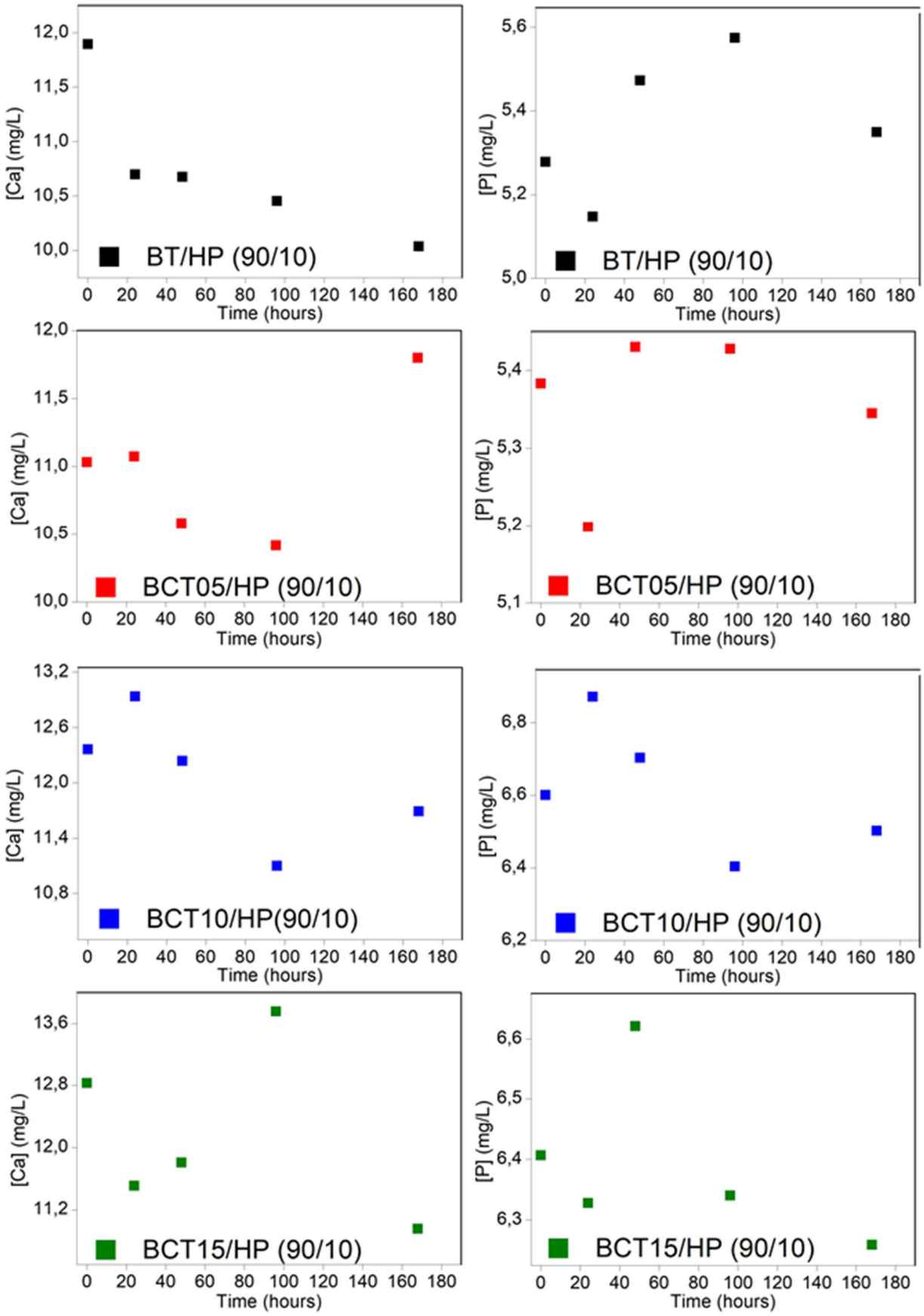

Figure L.5 ICP-AES results for unpolarized composites.

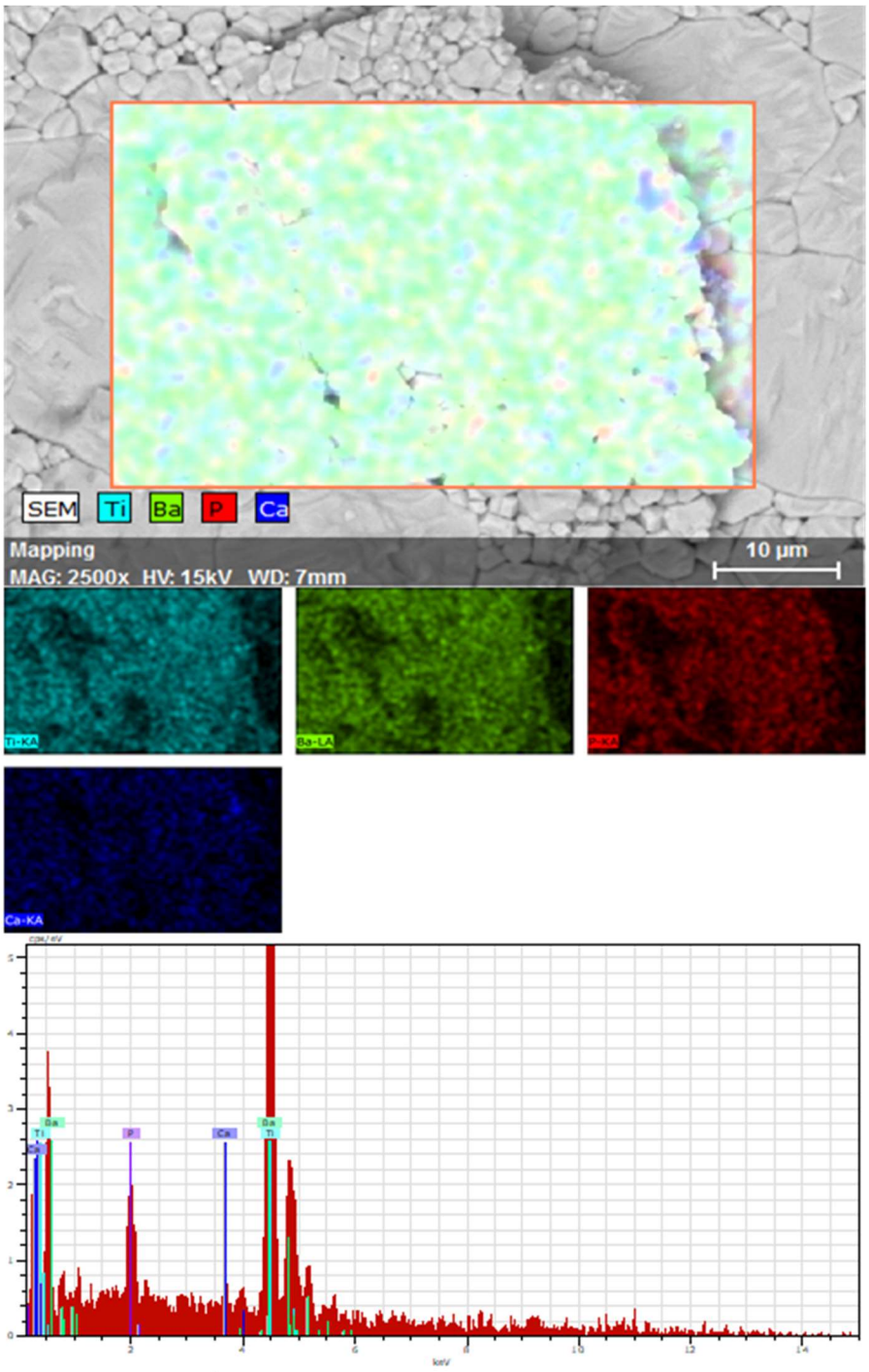

Spectrum: Point

Element	AN	Series	Net	unn. C [wt.%]	norm. C [wt.%]	Atom. C [at.%]
Titanium	22	K-series	1002	24.99	35.41	53.32
Barium	56	L-series	1190	40.25	57.02	29.94
Phosphorus	15	K-series	259	4.17	5.91	13.75
Calcium	20	K-series	67	1.18	1.67	3.00
		Total:		70.58	100.00	100.00

Figure L.6 SEM/EDS mapping and quantification of polarized BT sample after 7 days immersion in SBF.

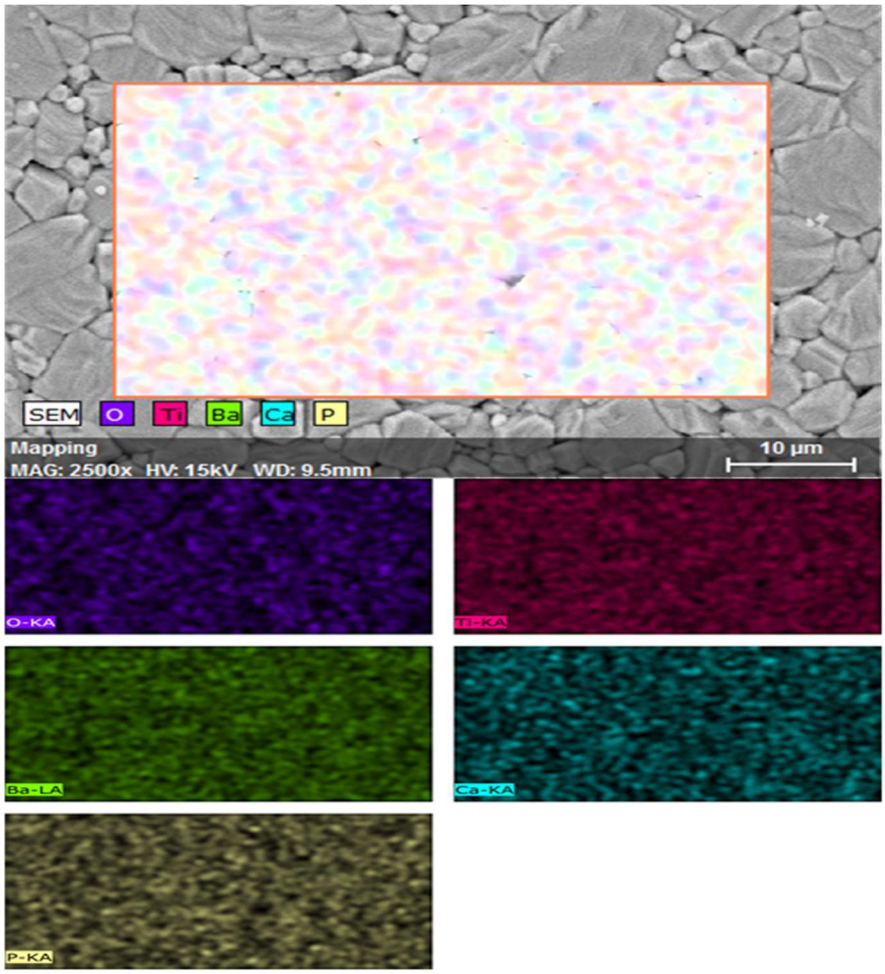

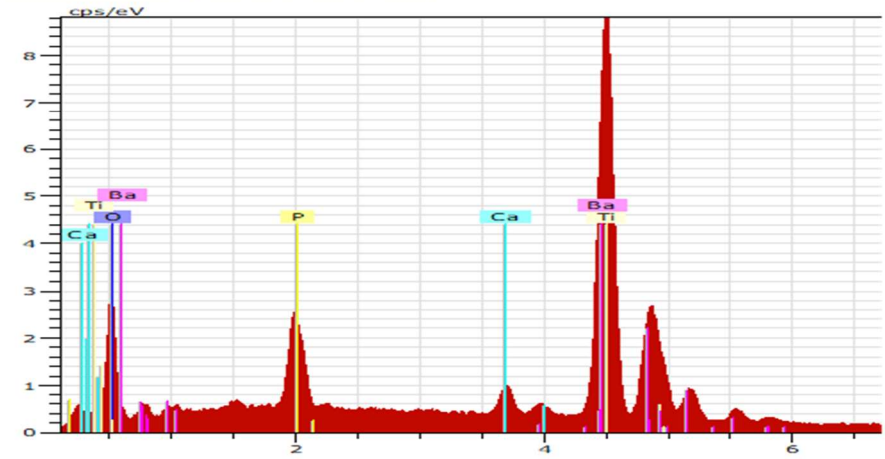

Spectrum: Point

Element	AN	Series	Net	unn. C [wt.%]	norm. C [wt.%]	Atom. C [at.%]
Oxygen	8	K-series	7740	17.67	22.32	54.51
Titanium	22	K-series	34336	25.86	32.67	26.66
Barium	56	L-series	29873	30.28	38.26	10.88
Phosphorus	15	K-series	8843	3.78	4.78	6.03
Calcium	20	K-series	3149	1.56	1.97	1.92
		Total:		79.14	100.00	100.00

Figure L.7 SEM/EDS mapping and quantification for polarized BCT10 sample after 7 days immersion in SBF.

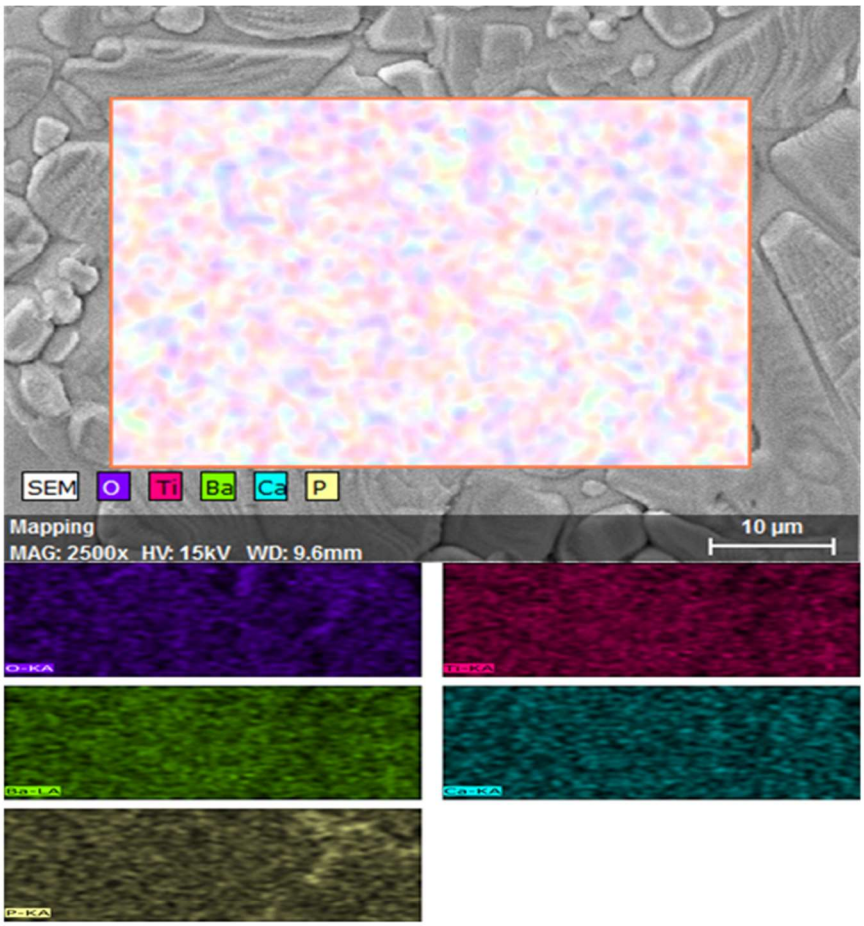

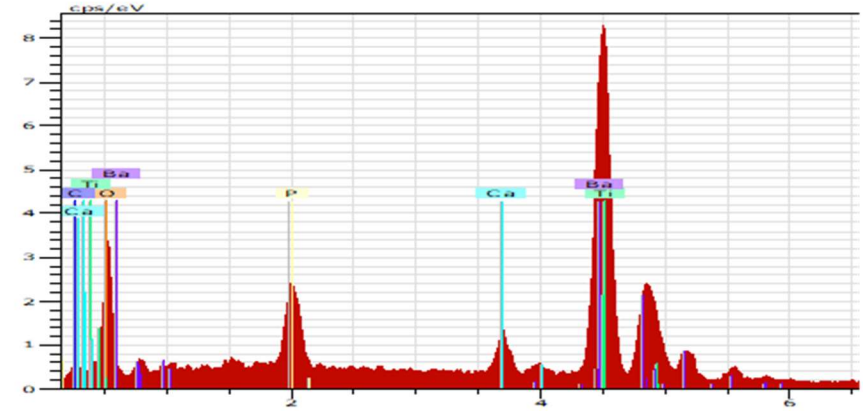

Spectrum: Point

Element	AN	Series	Net	unn. C [wt.%]	norm. C [wt.%]	Atom. C [at.%]
Oxygen	8	K-series	3775	19.08	22.76	52.68
Titanium	22	K-series	13441	23.81	28.40	21.97
Barium	56	L-series	13834	33.06	39.44	10.64
Carbon	6	K-series	412	1.90	2.27	7.01
Phosphorus	15	K-series	3705	3.49	4.17	4.98
Calcium	20	K-series	2079	2.47	2.95	2.73
			Total:	83.82	100.00	100.00

Figure L.8 SEM/EDS mapping and quantification for polarized BCT15 sample after 7 day immersion in SBF.